

Phase field modeling of ternary fluid-structure interaction problems

Von der Fakultät für Mathematik und Informatik
der Technischen Universität Bergakademie Freiberg

genehmigte

Dissertation

zur Erlangung des akademischen Grades

Doktor rerum naturalium

(Dr. rer. nat.)

vorgelegt

von **M.Sc. Dominic Mokbel Ala Al Dawla**

geboren am 04. Juli 1988 in Dresden

Gutachter: Prof. Dr. Sebastian Aland

Dr. Dirk Peschka

Tag der Verleihung: 19.12.2023

Kurzfassung

Interaktionen zwischen drei nicht mischbaren Phasen, einschließlich inkompressibler viskoelastischer Strukturen und Fluide, sind Gegenstand von zahlreichen naturwissenschaftlichen Untersuchungen. Die Komplexität vieler Szenarien dieser Art hat verschiedene Forschungsanstrengungen im Bereich des wissenschaftlichen Rechnens motiviert. Diese Arbeit präsentiert neuartige numerische Ansätze für zwei spezifische Konstellationen im Rahmen von ternären Fluid-Struktur-Interaktionen. Eine Reihe konkreter Anwendungen demonstriert das Potenzial dieser Ansätze. Zunächst wird ein Phasenfeldmodell entwickelt, das die Interaktion zwischen einem Fluid und einem viskoelastischen Festkörper beschreibt. Diesem Zweck dient ein Navier-Stokes-Cahn-Hilliard System in Kombination mit einem hyperelastischen Neo-Hooke-Modell. Darauf folgt die Implementierung einer ALE Methode (*arbitrary Lagrangian-Eulerian*) zur Simulation der Eindrückung des Festkörpers im Kontext einer Rasterkraftmikroskopie, wodurch schließlich physikalische Parameter vorhergesagt werden können. Im zweiten Ansatz geht es um die Wechselwirkung zwischen einem zweiphasigen Fluid und einem viskoelastischen Festkörper, wobei Fluid und Festkörper in getrennten Gebieten definiert sind. Beide Teilgebiete sind an einer gemeinsamen Grenzfläche ausgerichtet. Das zuvor eingeführte Phasenfeldmodell wird zur Darstellung des Fluids verwendet. Eine ALE Methode dient zur Bewegung des Gitters, wobei sich die Grenzfläche zwischen Fluid und Festkörper mit der Strömungsgeschwindigkeit bewegt. In allen Teilgebieten wird ein einheitliches System gelöst, das sowohl die Massen- und Impulsbilanz als auch das Kräftegleichgewicht an der Fluid-Festkörper-Grenzfläche umfasst. Der Fokus liegt in der Folge auf Simulationen von statischer und dynamischer Benetzung weicher Oberflächen. Von besonderem Interesse ist dabei eine Kontaktlinie, die sich über ein Substrat mit oszillierendem Stick-Slip-Verhalten bewegt. Diese Arbeit kombiniert die Vorteile von Phasenfeld- und ALE Methoden für aussagekräftige Simulationen und betont die Validität und numerische Stabilität aller Ansätze.

Abstract

Interactions between three immiscible phases, including incompressible viscoelastic structures and fluids, form standard constellations for countless scenarios in natural science. The complexity of many such scenarios has motivated various research efforts in scientific computing. This work presents novel numerical approaches for two specific of these ternary fluid-structure interaction constellations. The potential of these approaches is demonstrated by diverse applications. First, a phase field model is developed describing the interaction between a fluid and a viscoelastic solid. For this purpose, a Navier-Stokes-Cahn-Hilliard system is considered together with a hyperelastic neo-Hookean model. Based on this, an arbitrary Lagrangian-Eulerian (ALE) method is implemented to simulate the indentation of the solid material in the context of atomic force microscopy, capable of predicting physical parameters. Next, the second approach is developed to describe the interaction between a two-phase fluid and a viscoelastic solid, where fluid and solid are defined on separate domains but aligned at the interface between them. The previously introduced phase field model is used to represent the fluid and an ALE method is used for the motion of the grid, where the fluid-solid interface moves with flow velocity. A unified system is solved in all subdomains, which includes both the balance of mass and momentum and the balance of forces at the fluid-solid interface. Simulations of static and dynamic soft wetting are subsequently presented, in particular a contact line moving over a substrate with oscillating stick-slip behavior. This work combines the advantages of phase field and ALE methods for meaningful simulations and emphasizes validity and numerical stability in all approaches.

Contents

1	Introduction	1
1.1	Motivation	1
1.2	Overview of this thesis	2
2	Basic aspects	5
2.1	Sharp interface model for two-phase flow	5
2.2	Derivation of a phase field model for two-phase flow	7
2.2.1	Background and motivation	7
2.2.2	Total energy	8
2.2.3	Energy minimizer and phase field profile	9
2.2.4	Approximation to the sharp interface energy	13
2.2.5	Thermodynamic consistency	14
2.2.6	Navier-Stokes-Cahn-Hilliard model	19
2.3	Soft wetting	20
2.3.1	Background	20
2.3.2	Deformable boundary and contact angle condition	22
2.3.3	Wall energy specification	25
2.4	Numerical representation of free boundaries	26
3	Development of a phase field model for fluid-structure interaction (FSI)	29
3.1	Introduction	30
3.2	Sharp interface model for FSI	31
3.3	Phase field modeling	33
3.4	Energy dissipation	35
3.4.1	Energy time derivative	35
3.4.2	Force and flux	38
3.4.3	Governing equations	39
3.5	Axisymmetric setup and time-discrete equations	40

3.6	Numerical tests	43
3.6.1	Test setup	43
3.6.2	Benchmark quantity	45
3.6.3	Simulation results	46
3.7	Illustration of the method's potential	48
3.8	Conclusion	51
4	Phase field coupled to a rigid body: A ternary FSI approach for atomic force microscopy (AFM)	55
4.1	Introduction	55
4.2	Extension of the phase field model for FSI	57
4.2.1	Simulated scenario	57
4.2.2	Mathematical model	59
4.3	Numerical results	61
4.3.1	Model validation using Hertzian theory	61
4.3.2	Explicit relation of force and indentation	64
4.4	Probing mechanical properties of various materials	68
4.4.1	Viscoelastic properties of hydrogels	68
4.4.2	Viscoelastic properties of HeLa cells in interphase and mitosis	69
4.5	Discussion	75
5	Phase field coupled to a deformable solid: Modeling and simulation of soft wetting scenarios	79
5.1	Introduction	79
5.2	Mathematical model	81
5.2.1	Configuration	81
5.2.2	Governing equations	81
5.2.3	Unified model	85
5.3	Discretization	86
5.3.1	ALE discretization	86
5.3.2	Time discretization	86
5.3.3	Space discretization	88
5.4	Numerical tests	90
5.4.1	Validation study	90
5.4.2	Time step stability	92
5.4.3	Fluid substrates	93
5.4.4	Interaction between liquid droplets on viscoelastic substrates	95
5.4.5	Surfing on a viscoelastic substrate	96

5.5	Stick-slip contact line motion on Kelvin-Voigt model substrates	98
5.5.1	State of the art	99
5.5.2	Setup and contact line motion	100
5.5.3	Validation by an analytical model	104
5.5.4	Results	105
5.5.5	Discussion	109
5.6	Conclusions	110
6	Conclusions and outlook	113

Chapter 1

Introduction

1.1 Motivation

The interaction between fluid flows and structures is the subject of versatile studies, as it is widespread both in nature and in man-made technical constructions. *Fluid-structure interaction* (short: **FSI**) is a term used whenever a solid structure interacts with an internal or surrounding fluid. In this context, the term “structure” is quite general and can be physically distinguished from a continually deforming fluid by stronger bonds between the atoms of the material. Of particular interest are deformations of the structure caused by the flowing fluid, which in turn provide feedback in the flow. Such interactions are observed, for example, between airplane flights and the air flowing around them, between a pump and the air inside it, or between deformable blood vessels and the blood flowing through them. To study such scenarios, many modeling approaches have been developed in the past that involve two phases: exactly one fluid and exactly one structure. Most of the time, however, nature is more complex. If only a third phase is allowed in a model, a much wider range of applications opens up. For example, one could now study the interaction between platelets, blood plasma and blood vessels. Moreover, one could model scenarios with three states of matter (liquid, solid, gaseous), which is always the case when, for example, a drop of liquid sits on a deformable solid surface surrounded by air (soft wetting).

Of course, ternary FSI is a broad field and encompasses a rich variety of different problems. A more specific model assumption motivated by natural scenarios, which is also made in this thesis, is a solid structure with bulk viscoelasticity. To stay with the examples above: Blood cells and biological cells in general are commonly assumed to be viscoelastic bodies, and in the field of soft wetting one is often interested in (visco-)elastic substrates that are easily deformable by capillary forces, see e.g. [1]. When talking about mathematical and numerical methods to simulate such ternary FSI scenarios, one should first address the interaction of a single fluid phase with a single viscoelastic structure phase. This alone may be a significant challenge due to material-specific differences of the phases involved. Then, given a ternary FSI problem, one faces the challenge of finding an appropriate extended method

for modeling and discretization. This thesis addresses these challenges by providing different methods, each of which is flexibly extensible and capable of handling a variety of ternary FSI scenarios.

In ternary FSI problems, up to three types of free boundaries can appear between each two phases. In general, for the classification of numerical representation strategies, the literature often distinguishes between so-called interface capturing and interface tracking methods. Interface capturing methods (particularly phase field approaches [2]) use an implicit description of the free boundary and are often well suited for describing its evolution in complex dynamics. Phase field approaches generally provide a physically sound description of multi-phase flows and allow arbitrary topological changes of the (diffuse) free boundaries (see e.g. [3]). Since these are decisive advantages for the applications considered here, a phase field approach is used throughout this thesis. On the other hand, interface tracking methods explicitly describe the free boundary and offer different advantages. An important representative is the *arbitrary Lagrangian-Eulerian* (short: **ALE**) method [4], which is used in this thesis. In contrast to the phase field method, the ALE method gives not a diffuse but a sharp (grid) representation of the free boundary, which itself is usually moved with the flow velocity. An arbitrary grid motion can be defined in the bulk domains, mostly aimed at achieving numerical stability. The ALE method is fast and efficient, although limited to simple geometries. To exploit the advantages of both approaches and solve ternary FSI problems, combinations of phase field and ALE methods are used in this thesis.

1.2 Overview of this thesis

Chapter 2 explains basic aspects of the main components in this work. The starting point is a sharp interface model for incompressible, isothermal two-phase flows with immiscible fluids, as presented in Sec. 2.1. This is followed by the formulation of a phase field model for two-phase flows in Sec. 2.2. The phase field model considered here has already been discussed in [5, 6] and is a basis of all further approaches in this thesis. For a deeper understanding of this model, Sec. 2.2 provides a step-by-step derivation that couples an evolution equation for the diffuse interface with momentum and mass conservation of the flow. There, energetic arguments, thermodynamic consistency, and the approximation to the sharp interface limit are discussed. This section concludes with the summarized system of equations in Sec. 2.2.6. As soft wetting plays a significant role in this thesis, Sec. 2.3 provides some basics on this, including in particular a discussion of the contact angle condition used later. Furthermore, to address the numerical representation of free boundaries, the introductory chapter closes in Sec. 2.4 with a brief outline of the advanced strategies needed later to simulate ternary FSI problems.

Next, Chapter 3 turns to a phase field model for binary FSI based on the author's paper [7]. This extension of the basic model from Sec. 2.2 allows one of the phases to be modeled as a viscoelastic structure, with a choice of Kelvin-Voigt or Maxwell viscoelasticity. The evolution of the elastic strain is

described by an Oldroyd-B-like equation and neo-Hookean hyperelasticity is assumed, which is known to give accurate results even for strains up to the order of 100% [8]. The model is thermodynamically consistent and convergent towards the sharp interface limit. The chapter concludes with several simulation results to illustrate the method's potential. Even though only FSI scenarios were simulated, the model can be easily adapted to simulate any combination between purely viscous, viscoelastic and purely elastic materials. A specific model extension is presented in Chapter 4 and was published by the author in [9]. The idea is that by solving two evolution equations for elastic strain, a composite viscoelastic material is modeled, consisting of both a Maxwell and a Kelvin-Voigt component. Another special feature is the numerical representation of a specific ternary FSI problem: the indentation of a rigid spherical indenter in air into the viscoelastic material, simulating atomic force microscopy (AFM) experiments. The numerical strategy includes a combination of ALE and phase field methods. This chapter finally provides extensive applications that illustrate how the simulations help to probe viscoelastic parameters of biological cells and certain synthetic materials.

Lastly, Chapter 5 presents a comprehensive study published by the author in [10] and [11], offering simulations motivated by soft wetting phenomena. This time, the solid is modeled as a viscoelastic Kelvin-Voigt material with linear elastic contribution. In addition, a two-phase fluid represented by a phase field is defined in a separate domain. Capillary forces originating from surface tensions between all phases involved are included in the model. Together with suitable coupling conditions at the fluid-solid interface, Sec. 5.2.3 yields a unified model that is discretized and solved in a monolithic manner. Again, the numerical strategy consists of an individual combination of ALE and phase field methods. Validity and time step stability are discussed in Sec. 5.4. The subsequent numerical tests encompass scenarios such as the stationary state of droplets interacting with viscoelastic substrates and liquid interfaces surfing over viscoelastic substrates. The chapter concludes with a detailed investigation of stick-slip contact line motion in Sec. 5.5, with the simulations providing new physical insights into this hitherto poorly understood phenomenon.

Chapter 2

Basic aspects

As mentioned before, this thesis aims to model various types of three-phase problems. All of these models will use a classical phase field approach for two-phase flow [5, 6], which will be developed in Sections 2.1 and 2.2. Note that, in particular, no ternary phase field model is considered here, as was done e.g. in [12]. In order to represent the third phase, additional approaches will be introduced later. In the following argumentation, the underlying phase field approach is developed step by step, starting with the sharp interface model. Moreover, Sections 2.3 and 2.4 summarize aspects of soft wetting and domain representation methods that are essential for this thesis.

2.1 Sharp interface model for two-phase flow

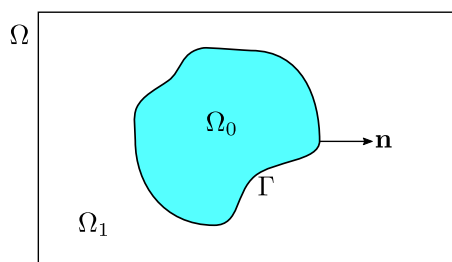


Figure 2.1: Illustration of the 2D setup.

This thesis basically considers incompressible, isothermal flows of immiscible fluids. With this in mind, a fundamental model for two-phase flow is introduced in this section. Let the considered domain $\Omega \subseteq \mathbb{R}^d$ be divided into two fluid domains Ω_0 and Ω_1 , as illustrated in Fig. 2.1 for two dimensions. The interface between the subdomains is denoted by Γ , such that $\Gamma = \overline{\Omega_0} \cap \overline{\Omega_1}$ and $\Omega = \Omega_0 \cup \Omega_1 \cup \Gamma$. A common velocity field $\mathbf{v} : \Omega \rightarrow \mathbb{R}^d$, continuous over Γ , indicates movements in both domains.

Let d_t denote the time derivative. Conservation of momentum and mass yield the governing equations

for two-phase flow:

$$\rho_i (d_t \mathbf{v} + \mathbf{v} \cdot \nabla \mathbf{v}) - \nabla \cdot (\eta_i (\nabla \mathbf{v} + \nabla \mathbf{v}^T)) + \nabla p = \mathbf{F} \quad \text{in } \Omega_i, i=0,1, \quad (2.1)$$

$$\nabla \cdot \mathbf{v} = 0 \quad \text{in } \Omega_i, i=0,1, \quad (2.2)$$

where ρ_i and η_i denote density and (dynamic) viscosity in Ω_i , respectively. Furthermore, p and \mathbf{F} denote pressure and body force defined in Ω , respectively. Density and viscosity are assumed to be constant in the respective subdomains. As a representative, the density can therefore be defined in the form $\rho : \Omega \rightarrow \mathbb{R}$, $\rho = \rho_0 \chi_0 + \rho_1 (1 - \chi_0)$ with constant ρ_0 , ρ_1 and a characteristic function $\chi_0 : \Omega \rightarrow \{0, 1\}$ being 1 in Ω_0 and 0 else.

In this section, neither initial conditions nor specific boundary conditions for \mathbf{v} and p on $\partial\Omega$ will be defined. Instead, it should only be specified that the outer boundary points stay at their initial positions for all times, which is essentially the case for later applications in this thesis. In contrast, the subdomains Ω_0 and Ω_1 are time-dependent and the movement is implicitly determined by the interface Γ . The latter is assumed to move with the flow velocity according to $d_t \Gamma = \mathbf{v}|_\Gamma$. An interface considered in this way is often referred to in the literature as a free boundary. Accordingly, ρ , η and χ also depend on time. It should be noted that all model applications in this thesis consider free boundaries that are advected with the hydrodynamic flow.

Furthermore, the following jump conditions across Γ hold:

$$[[\mathbf{v}]]_\Gamma = 0 \quad (2.3)$$

$$[[-p\mathbb{I} + \eta (\nabla \mathbf{v} + \nabla \mathbf{v}^T)]]_\Gamma \cdot \mathbf{n} = -\sigma \kappa \mathbf{n} + \nabla_\Gamma \sigma \quad (2.4)$$

with \mathbb{I} , σ , κ , \mathbf{n} and ∇_Γ denoting the identity matrix, the surface tension, the total curvature, the normal vector to Γ pointing into Ω_1 and the surface gradient, respectively. Moreover, $[[f]]_\Gamma = f_0 - f_1$ denotes the jump of a function f across Γ . Thus Eq. (2.3) describes the continuity of the velocity field in Ω . Eq. (2.4) is the interfacial force balance including a possible surface tension force. The term $\sigma \kappa \mathbf{n}$ is responsible for a force that smoothes out regions of strong curvature and minimizes the surface area. Note that the total curvature is positive for a sphere of Ω_0 . The term $\nabla_\Gamma \sigma$, also known as Marangoni force, describes the contribution of a surface tension gradient and consequently vanishes for constant σ . Given that σ is a quantity defined in the whole domain Ω , the Marangoni term can be calculated by $\nabla_\Gamma \sigma = \mathbf{P} \nabla \sigma$ with projection matrix $\mathbf{P} = \mathbb{I} - \mathbf{n} \otimes \mathbf{n}$, where \otimes denotes the dyadic product.

It should be noted that thermodynamic consistency of this system has already been proven, see

e.g. [13]. This means in particular that the total energy of the system,

$$E_{\text{total}} = \underbrace{\int_{\Omega} \frac{\rho}{2} |\mathbf{v}|^2 \, d\mathbf{x}}_{\text{kinetic energy}} + \underbrace{\int_{\Gamma} \sigma \, d\mathbf{x}}_{\text{surface tension energy}}, \quad (2.5)$$

is non-increasing in time.

Remark. *The free boundary does not necessarily have to be a single closed curve, as exemplified in Fig. 2.1. Instead, depending on the considered problem, it can take a variety of further shapes. In particular, the free boundary can have a non-empty intersection $\Gamma \cap \partial\Omega \neq \emptyset$ with the outer boundary of the domain. The latter case is of special interest in the context of (soft) wetting, see Sec. 2.3.*

In the following section, a diffuse phase field interface is considered instead of a sharp interface Γ . In this approach the total energy will need to be adjusted, which necessitates a re-examination of thermodynamic consistency.

2.2 Derivation of a phase field model for two-phase flow

As introduced in the last section, this thesis considers problems with free boundaries. Various strategies are available to represent the bulk regions and the free boundaries mathematically. Of course, each of these strategies has its advantages and disadvantages, and the demands of the specific problem decide which variant should be chosen. Since problems with three bulk regions will be considered in this thesis, there will ultimately also be up to three different types of free boundaries, each separating two bulk regions from each other. As discussed later in Sec. 2.4, a combination of two different representation methods will be useful.

At this point, the phase field approach is first introduced as one of these two methods and the simplified assumption of two bulk regions is retained. In the following, the basic idea and motivation of the approach are outlined as a first step. Afterwards, the total energy E_{total}^{ϕ} of the system will be developed, which will be shown to converge to the sharp interface energy E_{total} (Eq.(2.5)) for decreasing interface thickness. A mathematical formulation of the phase field function will be presented within this step. Finally, thermodynamic consistency of the system will be investigated, resulting in a phase field model for two-phase flow.

2.2.1 Background and motivation

In general, a phase field is a function that can be used to distinguish between several fluid phases. A two-phase setting similar to that in Sec. 2.1 is considered again here, but without dividing Ω into two subdomains. The phase field is typically defined as a function $\phi : \Omega \rightarrow \mathbb{R}$ that takes distinct values in

each of the phases, with a smooth transition across the interface. In this chapter, ϕ is chosen to take 0 in one phase and 1 in the other. As indicated in Fig. 2.2, one desirably obtains narrow interface regions with rapid phase transitions. The diffuse interface has a finite thickness, and a level set may be considered as its discrete location, e.g. $\{\mathbf{x} \in \Omega \mid \phi(\mathbf{x}) = 0.5\}$.

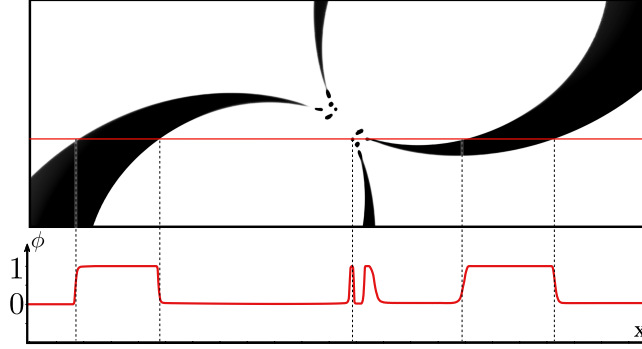


Figure 2.2: Principle of a phase field. Top: The color code indicates the phase field function with $\phi = 1$ in the black region and $\phi = 0$ in the white region. Bottom: Plot of ϕ over the horizontal line in the top image, illustrating the smooth but rapid transition across the diffuse phase field interface.

The use of such an auxiliary function has many benefits, that enable a multitude of applications in physics, biology or materials science. As will be shown in this thesis, the phase field model provides a physically sound method that can be used to describe systems whose dynamics are governed by both small-scale interfacial forces and macro-scale bulk forces. Furthermore, a phase field interface represented in a computational grid is not linked to individual grid points or edges. Consequently, it can undergo grid-independent topological changes. Moreover, in mathematical models, stress terms can be easily restricted to single phases or to the interface region, e.g. by multiplication with the phase field or a norm of its gradient. As a beneficial side effect, a phase field function supports clear visualization of simulation results using phase dependent color scales. In fact, the use of phase field models in various branches of natural science continues to grow to this day (see e.g. [3, 14]).

2.2.2 Total energy

In the following sections, a typical procedure for deriving a common phase field model for two-phase flow will be summarized. For more in-depth details on the arguments used here, see [15].

The change from a sharp to a diffuse interface is accompanied by a change in the interfacial contribution to the total energy of the system. Thus Eq. (2.5) has to be reformulated as

$$E_{\text{total}}^{\phi} = E^{\phi} + \underbrace{\int_{\Omega} \frac{\rho}{2} |\mathbf{v}|^2 \, d\mathbf{x}}_{\text{kinetic energy}} \quad (2.6)$$

with E^{ϕ} denoting the contribution of the diffuse interface which is yet to be determined. Note that

since the phase field approach allows mixing of the two phases in the narrow interface region, the velocity field \mathbf{v} is now defined as the volume-averaged velocity of this mixture. More on this will be explained in Sec. 2.2.5 (see also [5]).

According to the requirements for the phase field function described in Sec. 2.2.1, the definition of E^ϕ should take into account that the diffuse interface region should be thin as compared to the domain size. More generally, it is intended to penalize mixing of the phases. Another physically meaningful requirement is the penalization of phase transitions, which tends to reduce the interface level set. This fits with the assumption that enlarging the interface without external forces is energetically unfavorable.

A common choice that conforms to these conditions is the Ginzburg-Landau energy, defined by

$$E_{\text{GL}}^\phi := \int_{\Omega} \frac{\epsilon}{2} |\nabla \phi|^2 + \frac{1}{\epsilon} W(\phi) \, d\mathbf{x} \quad (2.7)$$

with a constant $\epsilon > 0$ referred to as interface thickness. Obviously, the first term of the integrand penalizes phase transitions. The second term gives a free energy density with a function $W(\phi)$, which should be chosen to penalize mixing of the phases. A typical choice is a polynomial of degree four with local minima at $\phi = 0$ and $\phi = 1$. Such a polynomial is also referred to as double well potential and provides the information that phase separation is energetically favorable. Note that Eq. (2.7) is not yet a definition for E^ϕ . Ultimately, one wants to define E^ϕ such that it converges to the sharp interface energy (second part in Eq. (2.5)) for $\epsilon \rightarrow 0$. It remains to be clarified to what extent E_{GL}^ϕ is convergent in this sense. In Sec. 2.2.4 it will finally turn out that E_{GL}^ϕ achieves the desired convergence behavior by multiplying with a certain constant scaling factor.

2.2.3 Energy minimizer and phase field profile

In order to be able to derive a concrete phase field model for two-phase flow, the total energy Eq. (2.6) must first be specified. For this purpose, a minimizer for the Ginzburg-Landau energy Eq. (2.7) is determined in the following. This procedure subsequently yields both a formulation of the phase field function in a one-dimensional case and a total energy that converges to the sharp interface energy Eq. (2.5) for $\epsilon \rightarrow 0$. As a first step, a stationary profile of the phase field is determined in the present subsection. The obtained mathematical description of the phase field can later be used to construct initial conditions for concrete time-dependent problems. As a second step, the convergence of the energy is covered in Sec. 2.2.4. The arguments used in these two steps can also be found in [16].

Finding a minimizer for E_{GL}^ϕ means finding an expression for ϕ with $\delta E_{\text{GL}}^\phi(\phi) / \delta \phi = 0$ in the sense of

a variational derivative. The first variation can be calculated by

$$\begin{aligned}
\delta E_{\text{GL}}^\phi(\phi) &= \frac{d}{d\lambda} E_{\text{GL}}^\phi(\phi + \lambda f) \Big|_{\lambda=0} \\
&= \frac{d}{d\lambda} \int_{\Omega} \frac{1}{\epsilon} W(\phi + \lambda f) + \frac{\epsilon}{2} |\nabla(\phi + \lambda f)|^2 \, d\mathbf{x} \Big|_{\lambda=0} \\
&= \int_{\Omega} \frac{1}{\epsilon} W'(\phi + \lambda f) f + \epsilon \nabla(\phi + \lambda f) \cdot \nabla f \, d\mathbf{x} \Big|_{\lambda=0} \\
&\stackrel{\text{ibp}}{=} \int_{\Omega} \left(\frac{1}{\epsilon} W'(\phi + \lambda f) - \epsilon \Delta(\phi + \lambda f) \right) f \, d\mathbf{x} \Big|_{\lambda=0} \\
&= \int_{\Omega} \left(\frac{1}{\epsilon} W'(\phi) - \epsilon \Delta\phi \right) f \, d\mathbf{x} \tag{2.8}
\end{aligned}$$

with an arbitrary function f such that E_{GL}^ϕ is uniquely defined on $\phi + \lambda f$ for sufficiently small λ . Note that integration by parts (ibp) was used in this calculation, where the occurring boundary integral contains the term $\mathbf{n}_\Omega \cdot \nabla\phi$ with \mathbf{n}_Ω denoting the outer normal to the domain boundary $\partial\Omega$. This term is set to zero here, which means that in case of contact, the diffuse interface always takes a contact angle of 90° at the outer boundary of the domain. Different contact angles can occur due to a wall free energy, see [17] and Sec. 2.3.

As a consequence of the calculation above, the variational derivative reads

$$\frac{\delta E_{\text{GL}}^\phi[\phi]}{\delta\phi} = \frac{1}{\epsilon} W'(\phi) - \epsilon \Delta\phi . \tag{2.9}$$

For simplification, a special case with dimension $d = 1$ and domain $\Omega = \mathbb{R}$ is considered in the following. Setting the variational derivative (2.9) to zero, together with appropriate boundary conditions, eventually leads to a specific energy minimizing profile for ϕ . The boundary conditions are chosen as

$$\text{(a) } \lim_{x \rightarrow -\infty} \phi(x) = 0, \quad \text{(b) } \phi(0) = 0.5, \quad \text{(c) } \lim_{x \rightarrow \infty} \phi(x) = 1, \quad \text{(d) } \lim_{x \rightarrow \pm\infty} \phi'(x) = 0. \tag{2.10}$$

Moreover, the double well potential is set to

$$W(\phi) = k\phi^2(1 - \phi)^2 \tag{2.11}$$

with a constant $k > 0$. In order to calculate the minimizer, the variational derivative is multiplied by

$\phi'(x)$ and integrated from $-\infty$ to x :

$$\begin{aligned}
& \int_{-\infty}^x \left[\frac{1}{\epsilon} W'(\phi(x^*)) \right] \phi'(x^*) - [\epsilon \phi''(x^*)] \phi'(x^*) \, dx^* = 0 \\
\implies & \int_{-\infty}^x \frac{1}{\epsilon} \frac{d}{dx^*} [W(\phi(x^*))] - \frac{\epsilon}{2} \frac{d}{dx^*} [\phi'(x^*)^2] \, dx^* = 0 \\
\implies & \frac{1}{\epsilon} W(\phi(x^*)) \Big|_{-\infty}^x - \frac{\epsilon}{2} \phi'(x^*)^2 \Big|_{-\infty}^x = 0 \\
\implies & \frac{1}{\epsilon} W(\phi(x)) - \frac{\epsilon}{2} \phi'(x)^2 = 0, \tag{2.12}
\end{aligned}$$

where the definition of $W(\phi)$ and Eqs. 2.10 (a) and (d) were used in the last implication step. Eq. (2.12) is referred to as **equipartition of energy** and states that both energy components in Eq. (2.7) contribute equally to the total energy of the system. Note that it can also be shown for higher dimensions that energy minimizers for Eq. (2.7) yield equipartition of energy, i.e.

$$\frac{1}{\epsilon} W(\phi) - \frac{\epsilon}{2} |\nabla \phi|^2 = 0. \tag{2.13}$$

Eq. (2.12) implies the ordinary differential equation

$$\phi'(x) = \frac{\sqrt{2k}}{\epsilon} \phi(1 - \phi) \tag{2.14}$$

whose analytical solution is

$$\phi_*(x) = \frac{\exp(\sqrt{2k} x/\epsilon)}{\exp(\sqrt{2k} x/\epsilon) + C} \tag{2.15}$$

with a constant C . This constant can be calculated by Eq. (2.10) (b) as $C = 1$. Hence, Eq. (2.15) can be reformulated as

$$\phi_*(x) = \frac{1}{2} + \frac{1}{2} \tanh\left(\frac{\sqrt{k}}{\epsilon\sqrt{2}} x\right) \tag{2.16}$$

using the definition of the hyperbolic tangent function. Such a function perfectly describes the smooth transition between the two phases at the interface, as shown in the left part of Fig. 2.3. The parameters k and ϵ control the order of magnitude of the transition region. Note that since there is no unique definition of the interface thickness, it cannot generally be equated with ϵ . However, one may e.g. define the interface region as $\{x \in \mathbb{R} \mid 0.1 < \phi_*(x) < 0.9\}$. Consequently, for a typical choice of $k = 1$ the interface region has the width

$$\phi_*^{-1}(0.9) - \phi_*^{-1}(0.1) = \epsilon\sqrt{2} \ln 9 \approx 3.1\epsilon. \tag{2.17}$$

An interface thickness defined in this way is therefore proportional to ϵ . Moreover, Eq. (2.17) suggests that ϵ approximately describes the order of magnitude of the transition region. In this thesis, ϵ is therefore referred to as interface thickness.

The result of this simple example is representative for more complex settings in higher dimensions. If the phase field is viewed along a line perpendicular to the interface, it will locally take a shape comparable to the hyperbolic tangent profile obtained here. However, prescribing boundary conditions for $\phi(\mathbf{x})$, $\phi'(\mathbf{x})$ with $\mathbf{x} \in \mathbb{R}^d$, $d > 1$ and complex interface shapes might lead to complicated mathematical derivations. A typical simple approach is the formulation of a signed distance function $D_{\pm} : \Omega \subset \mathbb{R}^d \rightarrow \mathbb{R}$ that describes the desired initial phase field interface [18]. This allows the boundary conditions Eq. (2.10) to be used again, replacing x by D_{\pm} . The derivation then analogously leads to the (scaled) hyperbolic tangent function Eq. (2.16). Consequently, Eq. (2.16) can be used as a universal description of the phase field profile for higher dimensions and a multitude of interface shapes.

Note that other value ranges of the phase field function can also be considered. A typical choice is $\phi \approx 1$ and $\phi \approx -1$ in the bulk regions, together with the double well potential $W(\phi) = k(1 - \phi^2)^2$. This yields

$$\phi_*(x) = \frac{\exp(2\sqrt{2k}x/\epsilon) - 1}{\exp(2\sqrt{2k}x/\epsilon) + 1} = \tanh\left(\frac{\sqrt{2k}}{\epsilon}x\right). \quad (2.18)$$

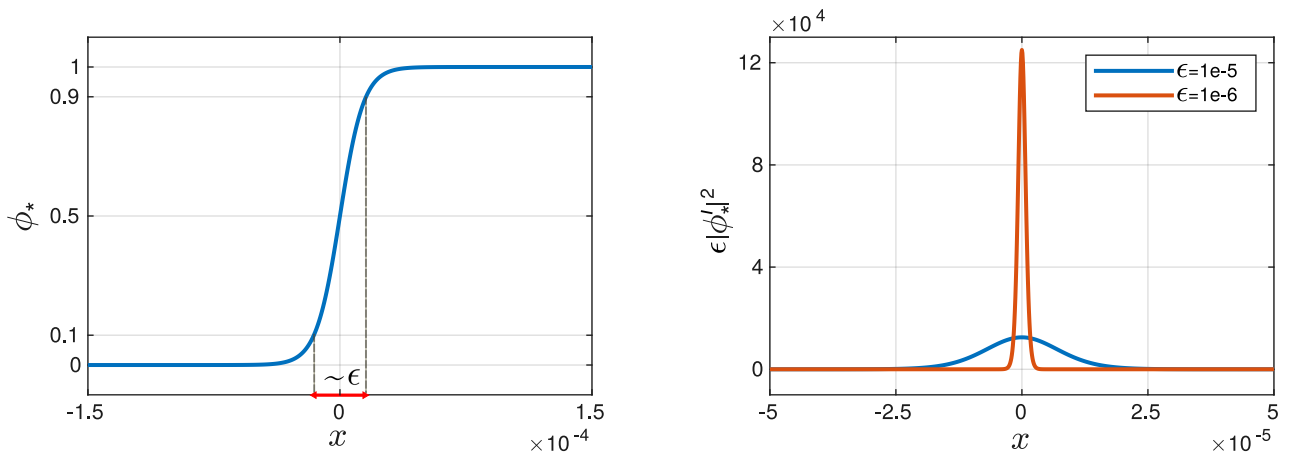


Figure 2.3: Graphs with double well potential Eq. (2.11) and parameter $k = 1$. **Left:** Tangent hyperbolic profile Eq. (2.16) with $\epsilon = 1e-5$. The highlighted part of the x -axis indicates the interface thickness, which is proportional to ϵ . It corresponds to the chosen phase field range $0.1 < \phi_* < 0.9$. **Right:** Energy density in Eq. (2.20).

2.2.4 Approximation to the sharp interface energy

The arguments in this subsection are consistent with those in [16]. Both the minimizer determined above and the equipartition of energy can now be entered in Eq. (2.7) to calculate the energy in the 1D example:

$$E_* := E_{\text{GL}}^\phi[\phi_*] = \int_{-\infty}^{\infty} \frac{\epsilon}{2} |\phi'(x)|^2 + \frac{1}{\epsilon} W(\phi(x)) \, dx \quad (2.19)$$

$$\stackrel{(2.12)}{=} \epsilon \int_{-\infty}^{\infty} |\phi'(x)|^2 \, dx \quad (2.20)$$

$$= \epsilon \int_0^1 |\phi'| \, d\phi \quad (2.21)$$

$$\stackrel{(2.14)}{=} \frac{\epsilon\sqrt{2k}}{\epsilon} \int_0^1 \phi(1-\phi) \, d\phi \quad (2.22)$$

$$= \frac{\sqrt{k}}{3\sqrt{2}}. \quad (2.23)$$

An advantageous property is the independence of E_* from epsilon. The energy only depends on the choice of the double well potential, for which Eq. (2.11) was used in the above calculation. For the case $W(\phi) = k(1-\phi^2)^2$ it follows $E_* = \frac{4}{3}\sqrt{2k}$.

The energy density is close to zero except in a vicinity of the interface. Moreover, in the passage to the limit $\epsilon \rightarrow 0$ this vicinity becomes narrower and the value at the interface increases. For the double well potential Eq. 2.11 this is illustrated in the right part of Fig. 2.3. The interface thickness ϵ was chosen there according to an order of magnitude that is typical for later applications in this thesis (in m).

With appropriate scaling of the energy density, the convergence of the following terms to the Dirac delta function δ_Γ can now be concluded:

$$\frac{1}{E_*} \left(\frac{1}{\epsilon} W(\phi) + \frac{\epsilon}{2} |\nabla\phi|^2 \right) \xrightarrow{\epsilon \rightarrow 0} \delta_\Gamma \quad (2.24)$$

$$\frac{\epsilon}{E_*} |\nabla\phi|^2 \xrightarrow{\epsilon \rightarrow 0} \delta_\Gamma \quad (2.25)$$

$$\frac{2}{\epsilon E_*} W(\phi) \xrightarrow{\epsilon \rightarrow 0} \delta_\Gamma \quad (2.26)$$

$$|\nabla\phi| \xrightarrow{\epsilon \rightarrow 0} \delta_\Gamma. \quad (2.27)$$

The left-hand side of (2.27) is a commonly used prefactor for terms to be restricted to the interface region, even in 2D and 3D (see [19]).

Furthermore, as a generalization of (2.24) it was shown in [20] for higher dimensions that minimization of the diffuse interface energy (2.7) corresponds to a minimization of the sharp interface area in the

limit $\epsilon \rightarrow 0$, i.e.

$$\frac{1}{E_*} E_{\text{GL}}^\phi \xrightarrow{\epsilon \rightarrow 0} \int_{\Gamma} 1 \, d\Gamma, \quad (2.28)$$

where the interface is defined by $\Gamma = \overline{\{\mathbf{x} \in \mathbb{R}^d | \phi(\mathbf{x}) = 0\}} \cap \overline{\{\mathbf{x} \in \mathbb{R}^d | \phi(\mathbf{x}) = 1\}}$ for $\phi \in \{0, 1\}$ almost everywhere. Note here that the phase field in the limit $\epsilon \rightarrow 0$ no longer has a smooth transition region, but a jump at the interface. This can be easily seen from the 1D profile Eq. (2.16):

$$\lim_{\epsilon \rightarrow 0} \phi_*(x) = \begin{cases} 1 & x > 0 \\ 0.5 & x = 0 \\ 0 & x < 0. \end{cases}$$

Finally, the previously unknown energy contribution E^ϕ given in Eq. (2.6) can now be formulated as

$$E^\phi = \frac{\sigma}{E_*} E_{\text{GL}}^\phi = \int_{\Omega} \frac{\sigma}{E_*} \left(\frac{1}{\epsilon} W(\phi) + \frac{\epsilon}{2} |\nabla \phi|^2 \right) \, d\mathbf{x} \quad (2.29)$$

with constant surface tension σ . Accordingly, the total energy of the system reads

$$E_{\text{total}}^\phi = \int_{\Omega} \underbrace{\frac{\rho}{2} |\mathbf{v}|^2}_{\text{kinetic energy}} + \underbrace{\frac{\sigma}{E_*} \left(\frac{1}{\epsilon} W(\phi) + \frac{\epsilon}{2} |\nabla \phi|^2 \right)}_{\text{diffuse interface energy}} \, d\mathbf{x}. \quad (2.30)$$

Inserting the surface tension σ at this point ensures the convergence of the total energy against the sharp interface energy (2.5),

$$E_{\text{total}}^\phi \xrightarrow{\epsilon \rightarrow 0} E_{\text{total}}, \quad (2.31)$$

which follows with (2.28).

Note that in many places in the remainder of this thesis, a **scaled** version of **surface tension** will be referred to as follows:

$$\tilde{\sigma} = \frac{\sigma}{E_*}. \quad (2.32)$$

2.2.5 Thermodynamic consistency

This subsection is the final step in the derivation of the phase field model for two-phase flow. To be consistent with thermodynamics, the total energy E_{total}^ϕ given in the previous subsection should not increase in time. For an investigation to this end, the time derivative of the energy is calculated in the following. This calculation uses an evolution equation for the phase field, which is formulated in a

first preparatory step. For an in-depth discussion on the argumentation in this subsection, see [5, 6].

Evolution of the phase field

A condition is now introduced that describes the desired time-dependent behavior of the phase field. This condition is intended to ensure phase separation in the manner described earlier. It is also intended to prevent, for example, a bubble with $\phi \approx 1$ from shrinking and eventually disappearing, which would result in $\phi \approx 0$ everywhere in the domain. More generally, the phase field should be described as a conserved quantity.

For these reasons, let $\phi = \phi(\mathbf{x}, t)$ with $\mathbf{x} \in \Omega$ now be a space- and time-dependent function whose evolution obeys

$$d_t \phi + \mathbf{v} \cdot \nabla \phi + \nabla \cdot \mathbf{j} = 0 \quad \text{in } \Omega \quad (2.33)$$

with a yet unspecified flux \mathbf{j} . Note that the material time derivative $d_t + \mathbf{v} \cdot \nabla$ was chosen here, which couples the phase field to the hydrodynamic flow velocity. Eq. (2.33) states that ϕ is a conserved quantity in Ω , where the flux describes the way that this quantity flows. The flux ultimately determines how the phase field is distributed over the domain. The choice for common diffusion would be $\mathbf{j} = D \nabla \phi$, which yields the diffusion equation $d_t \phi + \mathbf{v} \cdot \nabla \phi = -D \Delta \phi$ for a constant diffusion parameter $D > 0$ (also referred to as Fick's law). However, this would contradict the requirement to avoid mixing the two phases. An expression for the flux must therefore be found that provides the desired phase separation. The calculation in this subsection will eventually lead to a thermodynamically consistent choice of the flux.

System of equations to be specified

The facts discussed so far can be organized in the following way. The system of equations

$$\partial^\bullet (\rho(\phi) \mathbf{v}) - \nabla \cdot (\eta(\phi) (\nabla \mathbf{v} + \nabla \mathbf{v}^T)) + \nabla p = \mathbf{F} \quad (\text{conservation of momentum}) \quad (2.34)$$

$$\nabla \cdot \mathbf{v} = 0 \quad (\text{incompressibility}) \quad (2.35)$$

$$\partial^\bullet \phi + \nabla \cdot \mathbf{j} = 0 \quad (\text{conservation of } \phi) \quad (2.36)$$

holds in Ω , where the material derivative $d_t + \mathbf{v} \cdot \nabla$ is replaced with ∂^\bullet . The force \mathbf{F} and the flux \mathbf{j} are yet unknown quantities. Equations (2.34) - (2.36) are used below in the calculation of the energy time derivative. Thus \mathbf{F} and \mathbf{j} will appear in the resulting formulation of $d_t E_{\text{total}}^\phi$. Finally, an appropriate choice for \mathbf{F} and \mathbf{j} can be found given the condition

$$d_t E_{\text{total}}^\phi = d_t \left(\int_{\Omega} \frac{\rho(\phi)}{2} |\mathbf{v}|^2 + \frac{\sigma}{E_*} \left(\frac{1}{\epsilon} W(\phi) + \frac{\epsilon}{2} |\nabla \phi|^2 \right) d\mathbf{x} \right) \leq 0, \quad (2.37)$$

that ensures a non-increasing energy.

Density and viscosity are now phase-dependent quantities that may be interpolated e.g. by

$$\begin{aligned}\eta(\phi) &= \phi\eta_1 + (1 - \phi)\eta_0, \\ \rho(\phi) &= \underbrace{\phi\rho_1}_{=: \tilde{\rho}_1(\phi)} + \underbrace{(1 - \phi)\rho_0}_{=: \tilde{\rho}_0(\phi)},\end{aligned}$$

where ρ_1 , ρ_0 , η_1 and η_0 denote the (non-negative) constant values in the respective phases. $\tilde{\rho}_i(\phi)$ denotes the portion of the density field associated with phase i . The interpolations will later be adjusted in the extended models presented in this thesis.

Note that Eqs. (2.34) and (2.35) differ from those in the sharp interface approach in Sec. 2.1. In particular, Ω is not divided into two subdomains, and Ω_i is approximated by the domain where $\phi \approx i$. Partial mixing of the macroscopically immiscible fluids occurs in the thin interfacial region. As indicated by the density interpolation above, there is no constant density field in either phase, in contrast to the sharp interface model. For the latter, the incompressibility condition applies in each of the two phases, i.e. $\nabla \cdot \mathbf{v} = 0$ in Ω_i for $i = 0, 1$. In the present case of partial mixing, however, the mass conservation equation $d_t \tilde{\rho}_i + \nabla \cdot (\tilde{\rho}_i \mathbf{v}_i) = 0$ is assumed for the material represented by phase i . Here, the term $\tilde{\rho}_i \mathbf{v}_i$ describes the mass flux of this material with a corresponding flow velocity \mathbf{v}_i , see [5, 6, 21] for more details on the theory of mixture flows. According to [5], \mathbf{v} is assumed to be a **volume-averaged velocity** for this two-phase mixture, which implies the incompressibility condition Eq. (2.35) in the whole domain Ω . It can be defined as $\mathbf{v} = c_0 \mathbf{v}_0 + c_1 \mathbf{v}_1$, where the factors c_0 , c_1 denote volume fractions with $c_0 + c_1 = 1$. Here, the volume fractions are set to $c_0 = \tilde{\rho}_0(\phi)/\rho_0 = 1 - \phi$ and $c_1 = \tilde{\rho}_1(\phi)/\rho_1 = \phi$. Note that ρ_i represents the constant density of phase i in the unmixed state, i.e. in the sharp interface limit. The incompressibility condition can now be inferred by

$$\nabla \cdot \mathbf{v} = \sum_{i=0}^1 \frac{1}{\rho_i} \nabla \cdot (\tilde{\rho}_i \mathbf{v}_i) = \sum_{i=0}^1 \frac{1}{\rho_i} (-d_t \tilde{\rho}_i) = -d_t \sum_{i=0}^1 \frac{\tilde{\rho}_i}{\rho_i} = -d_t 1 = 0.$$

Remark. *Conservation of mass of this non-constant density system is given by Eqs. (2.35) and (2.36), where the validity of both equations implies the reformulated versions*

$$\begin{aligned}\partial^\bullet \rho(\phi) + \nabla \cdot (\rho'(\phi) \mathbf{j}) &= 0, \\ d_t \rho(\phi) + \nabla \cdot (\rho(\phi) \mathbf{v} + \rho'(\phi) \mathbf{j}) &= 0,\end{aligned}$$

see [5] for details. Note that because of the above interpolation of the density, $\rho'(\phi) = \rho_1 - \rho_0$ applies here. In the case of constant density, mass conservation is already given by $\nabla \cdot \mathbf{v} = 0$.

Computation of force and flux

The computation of force and flux is based on [7]. In this calculation, conditions (2.34) - (2.36) are inserted. Finally, a choice of \mathbf{F} and \mathbf{j} that satisfies condition (2.37) is made. The following identities will be useful:

$$\nabla \mathbf{v} : (\nabla \mathbf{v} + \nabla \mathbf{v}^T) = \frac{1}{2} |\nabla \mathbf{v} + \nabla \mathbf{v}^T|^2 \quad (2.38)$$

$$\partial^\bullet \rho(\phi) = \rho'(\phi) \partial^\bullet \phi \quad (2.39)$$

$$\begin{aligned} \partial^\bullet \left(\frac{\rho(\phi)}{2} |\mathbf{v}|^2 \right) &= \frac{1}{2} \partial^\bullet (\rho(\phi)) |\mathbf{v}|^2 + \partial^\bullet (\mathbf{v}) \cdot \rho(\phi) \mathbf{v} \\ &= \partial^\bullet (\rho(\phi) \mathbf{v}) \cdot \mathbf{v} - \frac{|\mathbf{v}|^2}{2} \partial^\bullet \rho(\phi) \end{aligned} \quad (2.40)$$

$$\partial^\bullet (|\nabla \phi|) = \frac{1}{|\nabla \phi|} (\nabla \phi \cdot \nabla (d_t \phi) + (\mathbf{v} \otimes \nabla \phi) : \nabla \nabla \phi), \quad (2.41)$$

where $|\cdot|$ in (2.38) denotes the Frobenius norm and $:$ in (2.41) the Frobenius inner product. In the following computation of the energy time derivative $d_t E_{\text{total}}^\phi$, occurring boundary integrals will be neglected that arise from integration by parts, as appropriate boundary conditions are assumed. Furthermore, a closed system is assumed, i.e. the domain Ω moves with the flow field, which holds in particular if $\mathbf{v} \cdot \mathbf{n}_\Omega = 0$ at the outer boundary $\partial\Omega$ (\mathbf{n}_Ω denoting the outer normal). This assumption simplifies the calculations since material derivatives will appear under the integral. As a first step, the **time derivative of the kinetic energy** is determined:

$$\begin{aligned} d_t \int_\Omega \frac{\rho(\phi)}{2} |\mathbf{v}|^2 \, d\mathbf{x} &\stackrel{(2.40)}{=} \int_\Omega \partial^\bullet (\rho(\phi) \mathbf{v}) \cdot \mathbf{v} - \frac{|\mathbf{v}|^2}{2} \partial^\bullet \rho(\phi) \, d\mathbf{x} \\ &\stackrel{(2.34)}{=} \int_\Omega (\mathbf{F} + \nabla \cdot (\eta(\phi) (\nabla \mathbf{v} + \nabla \mathbf{v}^T)) - \nabla p) \cdot \mathbf{v} - \frac{|\mathbf{v}|^2}{2} \partial^\bullet \rho(\phi) \, d\mathbf{x} \\ &= \int_\Omega \mathbf{F} \cdot \mathbf{v} - \eta(\phi) (\nabla \mathbf{v} + \nabla \mathbf{v}^T) : \nabla \mathbf{v} + p \nabla \cdot \mathbf{v} - \frac{|\mathbf{v}|^2}{2} \partial^\bullet \rho(\phi) \, d\mathbf{x} \\ &= \int_\Omega -\frac{\eta(\phi)}{2} |\nabla \mathbf{v} + \nabla \mathbf{v}^T|^2 + \mathbf{F} \cdot \mathbf{v} + \frac{|\mathbf{v}|^2}{2} \rho'(\phi) \nabla \cdot \mathbf{j} \, d\mathbf{x}, \end{aligned} \quad (2.42)$$

where Eqs. (2.35), (2.36), (2.38) and (2.39) were used in the last step. Regarding the occurring boundary integrals, either no flow across the boundaries, $\mathbf{v}|_{\partial\Omega} = 0$, or no force, i.e.

$$(\eta(\phi) (\nabla \mathbf{v} + \nabla \mathbf{v}^T) - p\mathbb{I}) \cdot \mathbf{n}_\Omega = 0$$

was assumed here. The next step is the **time derivative of the diffuse interface energy**:

$$\begin{aligned}
d_t E^\phi &= \frac{\sigma}{E_*} \int_{\Omega} \partial^\bullet \left(\frac{\epsilon}{2} |\nabla \phi|^2 + \frac{1}{\epsilon} W(\phi) \right) \, d\mathbf{x} \\
&\stackrel{(2.41)}{=} \frac{\sigma}{E_*} \int_{\Omega} \epsilon \nabla \phi \cdot \nabla (d_t \phi) - \epsilon (\mathbf{v} \cdot \nabla \phi) \Delta \phi - \epsilon \nabla \phi \cdot \nabla \mathbf{v} \cdot \nabla \phi + \frac{1}{\epsilon} W'(\phi) \partial^\bullet \phi \, d\mathbf{x} \\
&= \frac{\sigma}{E_*} \int_{\Omega} \left(\epsilon \nabla \phi \cdot \nabla \partial^\bullet \phi - \epsilon \nabla \phi \cdot \nabla \mathbf{v} \cdot \nabla \phi + \frac{1}{\epsilon} W'(\phi) \partial^\bullet \phi \right) \, d\mathbf{x} \\
&= \frac{\sigma}{E_*} \int_{\Omega} \left(-\epsilon \Delta \phi + \frac{1}{\epsilon} W'(\phi) \right) \partial^\bullet \phi + \mathbf{v} \cdot (\nabla \cdot (\epsilon \nabla \phi \otimes \nabla \phi)) \, d\mathbf{x} \\
&\stackrel{(2.36)}{=} \int_{\Omega} -\frac{\delta E^\phi}{\delta \phi} \nabla \cdot \mathbf{j} + \mathbf{v} \cdot (\nabla \cdot (\epsilon \tilde{\sigma} \nabla \phi \otimes \nabla \phi)) \, d\mathbf{x} , \tag{2.43}
\end{aligned}$$

where $\delta E^\phi / \delta \phi = \tilde{\sigma} (-\epsilon \Delta \phi + W'(\phi) / \epsilon)$ with $\tilde{\sigma} = \sigma / E_*$ denotes the (scaled) variational derivative of the interfacial energy, see Eq. (2.9). The term $\delta E^\phi / \delta \phi$ is also referred to as chemical potential. Note that the boundary condition $\mathbf{n}_\Omega \cdot \nabla \phi = 0$ on $\partial\Omega$ was used here, which effectively leads to a contact angle of 90° at the outer boundary of the domain. A more general contact angle condition is discussed in Sec. 2.3.

Summing up the calculated expressions, the time derivative of E_{total}^ϕ reads

$$\begin{aligned}
d_t E_{\text{total}}^\phi &= \int_{\Omega} -\frac{\eta(\phi)}{2} |\nabla \mathbf{v} + \nabla \mathbf{v}^T|^2 + \mathbf{F} \cdot \mathbf{v} + \frac{|\mathbf{v}|^2}{2} \rho'(\phi) \nabla \cdot \mathbf{j} \\
&\quad - \frac{\delta E^\phi}{\delta \phi} \nabla \cdot \mathbf{j} + \mathbf{v} \cdot (\nabla \cdot (\epsilon \tilde{\sigma} \nabla \phi \otimes \nabla \phi)) \, d\mathbf{x} \tag{2.44}
\end{aligned}$$

Furthermore, two terms in (2.44) can be reformulated applying integration by parts and using that $\rho'(\phi)$ is constant:

$$\begin{aligned}
\int_{\Omega} \frac{|\mathbf{v}|^2}{2} \rho'(\phi) \nabla \cdot \mathbf{j} &= \int_{\Omega} -\rho'(\phi) \mathbf{v} \cdot (\nabla \mathbf{v} \cdot \mathbf{j}) = \int_{\Omega} \rho'(\phi) \mathbf{v} \cdot \nabla \cdot (\mathbf{v} \otimes \mathbf{j}) \, d\mathbf{x} , \\
\int_{\Omega} -\frac{\delta E^\phi}{\delta \phi} \nabla \cdot \mathbf{j} \, d\mathbf{x} &= \int_{\Omega} \mathbf{j} \cdot \nabla \left(\frac{\delta E^\phi}{\delta \phi} \right) \, d\mathbf{x} ,
\end{aligned}$$

where no flux $\mathbf{j} \cdot \mathbf{n}_\Omega = 0$ at the outer boundary of the domain is assumed.

This finally yields the **total energy time derivative**

$$\begin{aligned}
d_t E_{\text{total}}^\phi &= \int_{\Omega} -\frac{\eta(\phi)}{2} |\nabla \mathbf{v} + \nabla \mathbf{v}^T|^2 + \mathbf{j} \cdot \nabla \left(\frac{\delta E^\phi}{\delta \phi} \right) \\
&\quad + \mathbf{v} \cdot [\mathbf{F} + \rho'(\phi) \nabla \cdot (\mathbf{v} \otimes \mathbf{j}) + \epsilon \tilde{\sigma} \nabla \cdot (\nabla \phi \otimes \nabla \phi)] \, d\mathbf{x} . \tag{2.45}
\end{aligned}$$

Hence, choosing

$$\mathbf{F} = -\rho'(\phi)\nabla \cdot (\mathbf{v} \otimes \mathbf{j}) - \epsilon\tilde{\sigma}\nabla \cdot (\nabla\phi \otimes \nabla\phi) \quad (2.46)$$

$$\mathbf{j} = -m(\phi)\nabla \left(\frac{\delta E^\phi}{\delta\phi} \right) \quad (2.47)$$

for some mobility function $m(\phi) > 0$ leads to non-increasing energy,

$$d_t E_{\text{total}}^\phi = - \int_{\Omega} \frac{\eta(\phi)}{2} |\nabla\mathbf{v} + \nabla\mathbf{v}^T|^2 + \frac{1}{m(\phi)} |\mathbf{j}|^2 \, dx \leq 0. \quad (2.48)$$

2.2.6 Navier-Stokes-Cahn-Hilliard model

The latter subsections allow for the formulation of a thermodynamically consistent diffuse interface model for incompressible two-phase flow with constant surface tension and phase-dependent density and viscosity. The momentum conservation equation is referred to as Navier-Stokes equation, and the conservation of the phase field as Cahn-Hilliard equation. The governing system of equations reads

$$\begin{aligned} \partial^\bullet (\rho(\phi)\mathbf{v}) - \rho'(\phi)\nabla \cdot (\mathbf{v} \otimes m(\phi)\nabla q) \\ - \nabla \cdot (\eta(\phi) (\nabla\mathbf{v} + \nabla\mathbf{v}^T)) + \nabla p = -\tilde{\sigma}\epsilon\nabla \cdot (\nabla\phi \otimes \nabla\phi) \end{aligned} \quad (2.49)$$

$$\nabla \cdot \mathbf{v} = 0 \quad (2.50)$$

$$\partial^\bullet \phi = \nabla \cdot (m(\phi)\nabla q) \quad (2.51)$$

$$\tilde{\sigma} \left(\frac{1}{\epsilon} W'(\phi) - \epsilon \Delta\phi \right) = q, \quad (2.52)$$

with constant $\rho'(\phi)$, constant $\tilde{\sigma} = \sigma/E_*$, and $q = \delta E^\phi/\delta\phi$ denoting the chemical potential. The mobility $m(\phi) > 0$ can be chosen arbitrarily. However, a thoughtless choice, while maintaining thermodynamic consistency, could render the phase field unusable and prevent this diffuse interface model from converging to the sharp interface model. The mobility should be small enough that the phase field is primarily advected with the hydrodynamic flow, and big enough that the phase field takes a tangent hyperbolic profile with the desired interface thickness. These limits depend strongly on space and time scales, and in practice are often determined by trial and error. Moreover, this model converges to the sharp interface model in Sec. 2.1 only by choosing certain mobilities. For example, for $m = M_0$ constant, the model would not converge. In this case, minimization of the diffuse interface energy would be dominant for $\epsilon \rightarrow 0$, whereby the interface strives for spherical shapes independent of the surrounding flow. Consequently the phase field would not primarily be advected with the

hydrodynamic flow for small ϵ . According to [7, 5], common choices that ensure convergence are

$$m(\phi) = \epsilon M_0 \text{ and} \tag{2.53}$$

$$m(\phi) = M_0 [\phi(1 - \phi)]_+ , \tag{2.54}$$

where $[\cdot]_+$ denotes the positive part of the quantity in brackets. Note that the values of ϕ can slightly exceed the interval $[0, 1]$, since in general the phase field does not satisfy a maximum principle. In this thesis, the choice of mobility corresponds to Eq. (2.53). In particular, no ϕ - dependent mobility is considered.

For completeness, the boundary conditions at the solid boundary $\partial\Omega$ are repeated here:

$$\mathbf{v} = \mathbf{0} \quad (\text{no flow across the boundary}), \tag{2.55}$$

$$\mathbf{n}_\Omega \cdot \nabla q = 0 \quad (\text{no flux}), \tag{2.56}$$

$$\mathbf{n}_\Omega \cdot \nabla \phi = 0 \quad (\text{contact angle } 90^\circ). \tag{2.57}$$

Moreover, in practical applications one often defines an initial condition on $\phi = \phi(\mathbf{x}, t)$ according to

$$\phi(\mathbf{x}, 0) = \phi_*(D_\pm(\mathbf{x})) \tag{2.58}$$

with a tangent hyperbolic function ϕ_* and a signed distance function D_\pm that describes the desired initial interface, see Eq. (2.16) or (2.18).

2.3 Soft wetting

2.3.1 Background

In the following, basic information about wetting is briefly introduced, which has already been extensively described in the available literature, see e.g. [22, 23].

Everywhere in nature we encounter three-phase constellations in which a gas, a liquid and a solid material come together. A typical example is a liquid droplet surrounded by air, sitting on a solid surface and forming a three-phase contact line. A balance between adhesive and cohesive forces determines to what extent the droplet connects to the surface. The term wetting generally refers to the ability of a liquid to be in contact with a solid. It is not limited to liquid-gas but also includes immiscible liquid-liquid constellations, e.g. an interface between water and oil coming into contact with glass. Wetting phenomena are highly multiscale in terms of space and time. While the contact line region may be in nanoscale or even smaller, droplets itself are typically in the millimeter range. And the time scale on which a liquid droplet typically assumes its steady state when it touches a solid surface is tiny compared to the characteristic time scale of many macroscopic processes, such as a

droplet rolling over a sloping surface.

A distinction is made between the two limit cases non-wetting and complete wetting. Staying with the droplet perspective, non-wetting can be illustrated by water-repellent surfaces on which a droplet rolls off. For example, the leaves of the lotus flower have almost non-wetting properties and are the namesake of the lotus effect [24]. Note, however, that even lotus leaves do not exhibit non-wetting in a strict sense. Due to very weak adhesion forces, a tiny fraction of the water droplet surface is in contact with the leaf. A typical illustration of complete wetting is automotive paint. There, a droplet should not roll off the surface, but rather spread out completely over the surface. The extent of wetting is influenced by the surface energies. The smaller the energy of the solid-liquid interface in relation to the solid-ambient interface, the more likely a droplet tends to wet the surface completely in order to minimize the energy.

A common relation between the surface energies and the contact angle of a droplet on a flat, rigid surface is Young’s equation, which is frequently used in the literature. Another commonly used relation is Neumann’s law, which holds for three liquid phases. Both cases can be found in Fig. 2.4. Note that the second equation of Neumann’s law for $\beta = 180^\circ$ reduces to Young’s equation. Neumann’s law applies under the conditions that the three angles add up to 360° and that one surface tension value (in N/m) must not be greater than the sum of the other two.

While the contact angle relations of these two cases are well known, things get more complicated when droplets come into contact with soft elastic solids. This case is referred to as soft wetting in this thesis. Compared to the wetting of rigid surfaces, the understanding of the dynamic processes involved in soft wetting is not as mature and is currently the subject of intensive research, see [25] for a review. The transition from a rigid substrate (infinite elasticity) to a fluid phase (zero elasticity) with a soft-elastic substrate in between is discussed in [23], considering the validity of Young’s equation and Neumann’s law. Formally, the elastocapillary length

$$\ell = \sigma/G \tag{2.59}$$

with surface tension σ and elastic (shear) modulus G is important here. In [23] it was suggested that the transition from Young’s equation to Neumann’s law occurs when the elastocapillary length is of the order of molecular interactions. From the latter work, it can be concluded that the contact angle is approximately described by Neumann’s law (or a variation of it) if ℓ is sufficiently larger than the molecular scale. This results from the fact that capillary forces, compared to elastic forces, can prevail locally at the contact line and deform the elastic substrate according to the surface tensions involved. In this respect, the term “soft wetting” may also be defined for materials that are soft enough such that the elastocapillary length is sufficiently large, taking into account typical surface tension values (e.g. of water or oil). The elastocapillary length itself gives a characteristic length scale within which the substrate is deformed.

In Chapter 5 of this thesis, soft wetting scenarios are simulated in which the phase field interface takes a certain angle with a boundary part of the computational domain (cf. Fig. 2.4). The parameters are chosen such that ℓ is several orders of magnitude larger than the molecular scale. It turns out that the results fit well with Neumann's law. It is important to ensure that the interface thickness ϵ as a parameter of the phase field model does not conflict with the physically motivated elastocapillary length. Therefore, ϵ is chosen sufficiently smaller than ℓ in later settings, which ensures the correct formation of the contact angle.

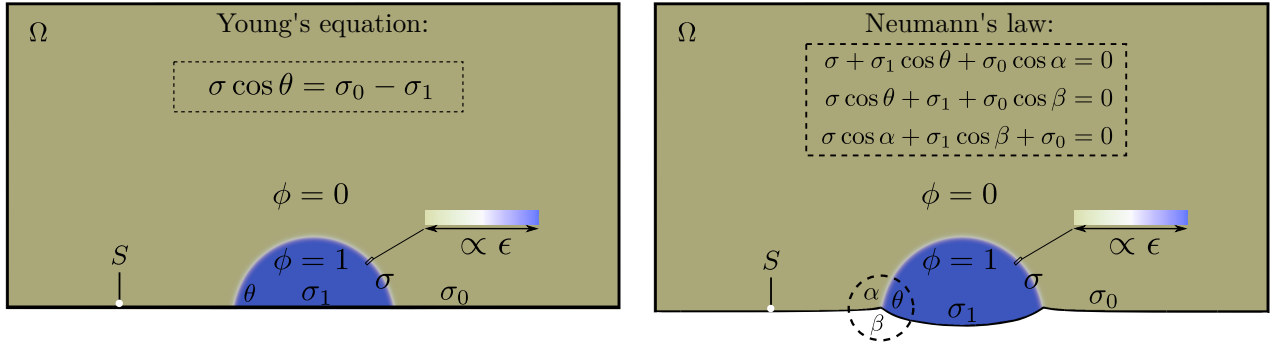


Figure 2.4: Binary fluid modeling a droplet in contact to a boundary part S . The color indicates the phase field ϕ . The symbols of the (constant) surface tension parameters are positioned at the associated places: σ is the surface tension of the phase field interface and σ_i is that of the subset of S in contact with the phase described by $\phi = i$ (for $i = 0, 1$). In addition, common relations are stated that predict stationary three-phase contact angles, the formation of which depends only on surface tension. **Left:** Rigid boundary $\partial\Omega$. **Right:** Deformable bottom boundary $S \subset \partial\Omega$.

2.3.2 Deformable boundary and contact angle condition

In the following, a typical wetting scenario is illustrated by a rectangular domain whose bottom boundary $S \subset \partial\Omega$ represents a substrate wetted by a droplet, see Fig. 2.4. The result of this subsection is a contact angle condition for the model from Sec. 2.2.6, describing the contact angle of the intersection of the phase field interface with S . This condition is valid for both a rigid and a deformable bottom boundary.

So far in this chapter, a closed system with rigid boundary $\partial\Omega$ has been considered. Here, $\mathbf{v} = \mathbf{0}$ is assumed on the rigid boundary part $\partial\Omega \setminus S$, while the part S is either also rigid or deforms with a non-zero flow velocity. Note that in the latter case the zero flow condition (2.55) does not apply on S . In both cases, Ω is still a closed system, and the calculation of the energy time derivative $d_t E_{\text{total}}^\phi$ in Sec. 2.2.5 can be used here.

To be more specific, the following boundary integrals result from integration by parts in the calculation

in Sec. 2.2.5:

$$\int_S (\mathbf{v} \otimes \mathbf{n}_S) : (-p\mathbb{I} + \eta(\phi) (\nabla \mathbf{v} + \nabla \mathbf{v}^T)) \, dS \text{ (from kinetic energy Eq. (2.42)) ,} \quad (2.60)$$

$$\tilde{\sigma}\epsilon \int_S (\mathbf{n}_S \cdot \nabla \phi) \partial^\bullet \phi - \mathbf{v} \cdot ((\nabla \phi \otimes \nabla \phi) \cdot \mathbf{n}_S) \, dS \text{ (from diffuse interface energy Eq. (2.43)) ,} \quad (2.61)$$

with $\mathbf{n}_S = \mathbf{n}_\Omega|_S$ denoting the outer surface normal to S . The first occurring boundary integral (2.60) can be neglected if S is assumed rigid, i.e. $\mathbf{v}|_S = \mathbf{0}$. Furthermore, in contrast to the previous section, the boundary integral (2.61) is non-zero this time since the restriction to a 90° contact angle ($\mathbf{n}_\Omega \cdot \nabla \phi = 0$) should be removed on S . This holds regardless of whether S is deformable or not. The 90° contact angle condition should only remain on $\partial\Omega \setminus S$. Note that in the calculation in Sec. 2.2.5 further boundary integrals occurred including the term $\mathbf{j} \cdot \mathbf{n}_\Omega$, all of which are neglected here due to the assumed no-flux condition.

Moreover, note that in case of a deformable boundary part S , the deformation is influenced by a surface tension force, which contributes to the formation of the contact angle. The second integrand term in (2.61) gives rise to this force. Additionally, a surface tension of S should be introduced. This can be realized by the wall energy contribution in a general form,

$$E_S = \int_S \sigma_S(\phi) \, dS,$$

with some interpolation $\sigma_S(0) = \sigma_0$ and $\sigma_S(1) = \sigma_1$, where σ_0 and σ_1 denote constant surface tension parameters belonging to the respective phases (see Fig. 2.4). The specification of $\sigma_S(\phi)$ will be derived in the next subsection. The time derivative can be calculated by

$$d_t E_S = \int_S (\sigma_S(\phi) \kappa \mathbf{n}_S - \nabla_S \sigma_S(\phi)) \cdot \mathbf{v} + \sigma'_S(\phi) \partial^\bullet \phi \, dS, \quad (2.62)$$

with κ and ∇_S denoting the total curvature of S and the surface gradient with respect to S , respectively. In case of deformability, the first two (velocity-dependent) integrand terms in Eq. (2.62) give rise to a force acting on S , comparable to Eq. (2.4). Note that the term total curvature is occasionally also referred to in the literature as mean curvature, which in both cases refers to the sum of the principal curvatures of the surface under consideration [26]. It can also be equated to $\kappa = \nabla_S \cdot \mathbf{n}_S$, where $\nabla_S \cdot$ denotes the surface divergence with respect to S .

Adding up a first part of the terms from (2.60)-(2.62) yields an additional contribution to the energy time derivative on S , namely

$$\mathbf{v} \cdot (-p\mathbf{n}_S + \eta (\nabla \mathbf{v} + \nabla \mathbf{v}^T) \cdot \mathbf{n}_S - \nabla_S \sigma_S + \sigma_S \kappa \mathbf{n}_S - \tilde{\sigma}\epsilon (\nabla \phi \otimes \nabla \phi) \cdot \mathbf{n}_S) . \quad (2.63)$$

This contribution vanishes for rigid boundaries due to $\mathbf{v}|_S = \mathbf{0}$. To maintain the thermodynamic

consistency of the system, it is sufficient to set (2.63) to zero. Therefore, in contrast to the model in Sec. 2.2.6, the change to a deformable boundary part S necessitates the replacement of the no-flow condition (2.55) on S by

$$\mathbb{S}_\Omega \cdot \mathbf{n}_S - \nabla_S \sigma_S + \sigma_S \kappa \mathbf{n}_S = 0 \quad (2.64)$$

with the bulk stress contribution $\mathbb{S}_\Omega := -p\mathbb{I} + \eta(\nabla \mathbf{v} + \nabla \mathbf{v}^T) - \tilde{\sigma} \epsilon \nabla \phi \otimes \nabla \phi$, whose divergence appears in the momentum equation (2.49).

The remaining boundary terms, namely the third term in Eq. (2.62) together with the first term in Eq. (2.61) lead to the condition

$$\partial^\bullet \phi (\tilde{\sigma} \epsilon \mathbf{n}_S \cdot \nabla \phi + \sigma'_S(\phi)) \leq 0 \quad \text{on } S \quad (2.65)$$

in terms of thermodynamic consistency. This justifies the **dynamic contact angle condition**

$$\partial^\bullet \phi = -\nu (\tilde{\sigma} \epsilon \mathbf{n}_S \cdot \nabla \phi + \sigma'_S(\phi)) \quad \text{on } S \quad (2.66)$$

with a relaxation parameter $\nu > 0$. The limit $\nu \rightarrow \infty$ yields the **static contact angle condition**

$$\tilde{\sigma} \epsilon \mathbf{n}_S \cdot \nabla \phi = -\sigma'_S(\phi) \quad \text{on } S. \quad (2.67)$$

Note that this replaces the boundary condition (2.57) to remove the 90° contact angle limitation.

The setting considered here will be extended in Chapter 5. There, the phase field approach will be connected to an ALE approach, modeling a two-phase fluid Ω_f in contact to a deformable, (visco-)elastic solid substrate Ω_S with a sharp free boundary $\Gamma = \Omega_f \cap \Omega_S$ in between (see also Sec. 2.4 for a brief overview of this method). As will be demonstrated, the simulated droplets in Chapter 5 reach an equilibrium state. In the absence of elasticity, the stationary angles are determined by the surface tension values, which is ensured by the above contact angle conditions.

Remark. *Note that the static contact angle condition can also be derived from the constrained minimization problem*

$$\begin{aligned} \tilde{\sigma} \int_\Omega \frac{\epsilon}{2} |\nabla \phi|^2 + \frac{1}{\epsilon} W(\phi) \, d\mathbf{x} + \int_S \sigma_S(\phi) \, dS \rightarrow \min \\ \text{such that } \int_\Omega \phi \, d\mathbf{x} = \text{const.} \end{aligned}$$

in the stationary case, i.e. $\mathbf{v} = \mathbf{0}$ and $d_t \phi = 0$, see [27] for details.

2.3.3 Wall energy specification

Rigid boundary

In the following, a specification of the wall energy density $\sigma_S(\phi)$ is obtained for the case of a flat, rigid bottom boundary S .

A desirable property for the wetting scenarios here is that each level set of the phase field intersects the rigid boundary with the same angle. This can be formulated by

$$\mathbf{n}_S \cdot \frac{\nabla\phi}{|\nabla\phi|} = \cos\theta. \quad (2.68)$$

In addition, Young's equation from Fig. 2.4 should apply. These two assumptions are consistent with the static contact angle condition Eq. (2.67), see [27, 28] for details. With this information, a formulation of $\sigma'_S(\phi)$ can first be determined:

$$\begin{aligned} \sigma'_S(\phi) &\stackrel{(2.67)}{=} -\tilde{\sigma}\epsilon\mathbf{n}_S \cdot \nabla\phi \stackrel{(2.68)}{=} \tilde{\sigma}\epsilon|\nabla\phi| \frac{\sigma_1 - \sigma_0}{\sigma} \\ &\stackrel{(2.13),(2.11)}{=} \tilde{\sigma}\epsilon \frac{\sqrt{2k}}{\epsilon} \phi(1-\phi) \frac{\sigma_1 - \sigma_0}{\tilde{\sigma}(\sqrt{k}/(3\sqrt{2}))} \\ &= 6\phi(1-\phi)(\sigma_1 - \sigma_0), \end{aligned}$$

where the equipartition of energy Eq. (2.13) is used. Note that the scaling of the physical surface tension σ is chosen as described in Sec. 2.2, i.e. $\sigma = E_*\tilde{\sigma}$ with $E_* = \sqrt{k}/(3\sqrt{2})$ and double well parameter k . The above result leads to the definition of the wall energy density as

$$\sigma_S(\phi) = (\sigma_1 - \sigma_0)(3\phi^2 - 2\phi^3) + \sigma_0, \quad (2.69)$$

and therefore the conditions $\sigma_S(0) = \sigma_0$ and $\sigma_S(1) = \sigma_1$ are fulfilled. For further details on the wall energy contribution see e.g. [29, 30].

Deformable Boundary

As opposed to a rigid boundary, the normal \mathbf{n}_S on a deforming boundary part S varies in space and time which introduces additional numerical challenges and errors. In the present model as well as in recent soft wetting approaches [28, 31, 32] the three-phase contact line singularity is regularized by a phase field interface and therefore not exactly represented. Consequently, in contrast to a rigid boundary, the calculation of \mathbf{n}_S depends on both the grid accuracy at the contact line and the diffuse interface thickness. This affects the contact angle conditions Eqs. (2.66) and (2.67). These challenges raise the question of whether Neumann's law (Fig. 2.4) can be confirmed by numerical simulations, and if so, with what accuracy. Moreover, it should generally be considered to what extent the bulk

elasticity of deformable substrates contributes to the stationary contact angle.

In fact, the universality of Neumann’s law for the wetting of soft-elastic substrates has already been confirmed numerically. A strategy presented in [33], called goal-adaptive finite-element method, applies a localized force with a remarkably fine grid resolution in the vicinity of the contact line singularity. The results suggest that the force balance at the contact line, i.e. the formation of the stationary contact angle, is governed solely by the values of surface tension (here: σ , σ_1 and σ_0). In particular, an influence of bulk elasticity on the stationary angle could be excluded in the latter work.

It should be noted here that in the phase field approaches in [28, 31] and in this thesis, Neumann’s law does not appear directly in the governing equations of the models. In all these works the static contact angle condition Eq. 2.67 is implemented, which corresponds to Young’s equation (see [27, 28]). Furthermore, the grid resolution at the contact line is significantly finer in the goal-adaptive finite-element method [33] than in the aforementioned phase field approaches. Nevertheless, these phase field approaches are capable of providing convincingly good agreement of numerical results with Neumann’s law as long as the substrate is not elastic. In Sec. 5.4.3, this is demonstrated by simulations of droplets on a fluid substrate. Note further that Neumann’s law can be interpreted as a generalization of Young’s equation for three deformable interfaces, which can be proven by setting $\beta = \pi$ in the second equation (right part in Fig. 2.4).

This thesis follows the approach in [28] and uses the contact angle condition (2.67) together with an appropriate wall energy density (here (2.69)) for both rigid and deformable boundaries.

2.4 Numerical representation of free boundaries

This section briefly outlines the way ternary fluid-structure interaction problems are numerically represented in this thesis.

When it comes to the numerical representation of a free boundary on a computational grid, one can distinguish between an implicit and an explicit description of the boundary. Implicit descriptions use an additional (scalar) function. In Sec. 2.2 the phase field model was introduced as such a method. The phase field function assigns a scalar value to each grid point of a computational domain. As discussed in Sec. 2.2, the exact position of the free boundary can then be described e.g. as a level set with $\phi = 0.5$, while the bulk phases are represented by $\phi \approx 1$ and $\phi \approx 0$. The diffuse interface can thus be simulated moving freely on a rigid (Eulerian) grid, allowing for topological changes such as droplet merging or droplet splitting. However, this decisive advantage may be accompanied by losses of efficiency if a high resolution of the grid at the free boundary makes numerical calculations more expensive.

Further examples of methods with implicit description of the free boundary are the level-set method [34] or the volume-of-fluid method [35].

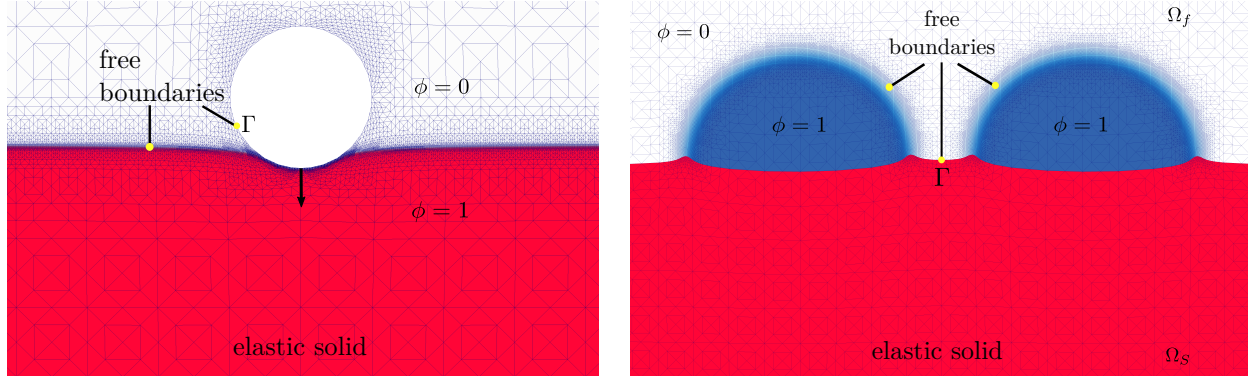


Figure 2.5: Schemes of phase field-ALE settings used in this thesis. The images each show a section of an exemplary computational grid. The phase field is denoted by ϕ , and Γ denotes a sharp boundary whose grid points are considered to be material points. **Left:** Setting in Chapter 4. **Right:** Setting in Chapter 5, where Ω_f and Ω_S denote separate domains (fluid and solid) that are aligned at Γ .

An explicit description can be given, for example, by identification of the free boundary with grid points of the computational domain, which are modeled as material points and thus move with flow velocity. This yields a sharp representation of the free boundary. A common choice is the ALE method (arbitrary Lagrangian-Eulerian) [4], which will also be used in this thesis. A typical setting is illustrated in Fig. 2.1: A computational domain Ω with rigid boundary $\partial\Omega$ is considered, within which the free boundary Γ moves with flow velocity. The grid points on $\partial\Omega$ correspond to the Eulerian view, those on the free boundary Γ to the Lagrangian view. The bulk phases Ω_1 and Ω_0 are separated from each other but aligned on Γ . In order to keep a proper shape of the grid in the bulk phases, the grid motion can there be defined as a harmonic extension of the boundary motion.

Another example of an explicit description of free boundaries is the immersed-boundary method [36]. Such methods are fast and efficient in general, but limited to simple geometries, since numerical grids are usually not allowed to be distorted arbitrarily for stability reasons.

In this thesis, combinations of the phase field approach and the ALE method are used to describe the (up to three different types of) free boundaries that move between each two adjacent bulk phases. The first of two different settings contains the contact between two solids and a fluid. One of the solids is represented by the numerical grid and moved with the ALE method, the other one is described together with the fluid by a phase field. It is important to emphasize here that the phase field approach can be used not only to describe interfaces between two fluids, but also to describe the interface between a fluid and an elastic solid. A corresponding model is developed in Chapter 3. The first phase field-ALE setting is exemplarily shown in the left part of Fig. 2.5. This illustration is oriented to Chapter 4, where one of the solids is represented as a hole in the numerical grid.

In the second setting, the three phases consist of a two-phase fluid, represented by a phase field, and an elastic solid. The fluid domain Ω_f and the elastic solid domain Ω_S are separated from each other,

but aligned at the sharp interface Γ , see the right part of Fig. 2.5. The sharp interface is moved with the ALE method. As discussed in Chapter 5, a wide variety of soft wetting scenarios can be simulated with this phase field - ALE setting.

Chapter 3

Development of a phase field model for fluid-structure interaction (FSI)

This chapter introduces a phase field model for binary fluid–structure interaction (FSI). It is an extension of the phase field model for two-phase flows presented in Sec. 2.2 with the additional contribution of a phase-dependent elasticity. The model developed in the present chapter forms the basis for the application in Chapter 4. The content presented here was previously published by the author in Mokbel et al. [7] with minor variations in notation and structure. Further background details on the mathematical model can also be found in [5].

At the beginning of the chapter, an introduction to modeling approaches for FSI problems is given, in particular clarifying the advantages of the present method and its differences from the popular ALE method. Sec. 3.2 starts by recapitulating the sharp-interface equations for FSI, where the momentum and mass balance equations are identical to those previously introduced in Sec. 2.1. The equations are extended to a phase field formulation with phase-dependent elastic stress in Sec. 3.3. The model is based on a thermodynamically consistent derivation (Sec. 3.4), which relates to the arguments in Sec. 2.2.5. Subsequently, an axisymmetric formulation of the problem is introduced, described in Sec. 3.5 including the corresponding time discretization. Numerical tests are presented in Sec. 3.6. Special focus is put on a comparison to the ALE reference solution of an elastic cell traversing a cylindrical channel. After this validation, the potential of the method is demonstrated in Sec. 3.7, by simulating

- (i) a solid object moving through a fluidic channel without grid remeshing,
- (ii) FSI with strong surface energy, i.e. surface tension forces,
- (iii) contact dynamics of a bouncing ball, and
- (iv) adhesion of an elastic object to a rigid wall.

The chapter closes with conclusions on the applicability of the method in Sec. 3.8.

3.1 Introduction

In fluid-structure interaction (FSI) problems, a solid structure interacts with an internal or surrounding fluid. Such problems arise in many scientific and engineering applications, for example in aeroelasticity, sedimentation, biological fluids and biomechanics, see [37] for a review. Yet the modeling of FSI problems is mathematically challenging due to the fundamental differences of the involved materials: a continually deforming (i.e. flowing) fluid, as opposed to a structurally rigid solid whose atoms are tightly bound to each other.

Most modeling approaches deal with this discrepancy by introducing two different coordinate systems and two numerical meshes for the two materials. The most popular approach is the arbitrary Lagrangian-Eulerian (ALE) method [4] in which the computational domain is subdivided into a fluid domain Ω_f and a structure domain Ω_S (cf. Sec. 2.4). The (elastic) structure is described there in the Lagrangian coordinate system, with deformations captured in a displacement vector field. On the contrary, the fluid domain is described in an Eulerian coordinate system and the variable of interest is the velocity field. Both meshes are aligned at the fluid-solid interface which is typically moved with the calculated velocity. While this methodology provides a sound mathematical description and leads to a very accurate domain representation, it also comes with limitations on the evolution of the solid structure, which breaks down for large deformations or large translational and rotational movements. Hence, even simple scenarios like an elastic body moving through a viscous fluid may become impossible to simulate, since technically advanced (re-)triangulation methods and clever interpolations are needed. This has led to the development of alternative modeling approaches in recent years, in particular fully Eulerian formulations [38] and interface capturing methods.

As mentioned in Sec. 2.4, interface capturing methods implicitly describe the interface between two domains by an additional field variable. Most popular interface capturing methods are the level-set [34], volume-of-fluid [39], and phase field method, see Sec. 2.2. Only a few years ago numerical schemes were developed to describe fluid-structure interactions in level-set methods [40, 41, 42] and volume-of-fluid methods [35].

Phase field methods offer some distinct advantages over other interface capturing methods, depending on the application of interest. For example, they can intrinsically include mass conservation and transport stabilization and allow for fully discrete energy stable schemes, see e.g. [43, 44], for two-phase flows. Furthermore, these methods offer a simple mechanism to couple the multi-phase system to additional physical processes, for example on the interface or in the bulk phases, see for examples [45, 46, 47]. In case of a non-negligible surface energy, phase field methods allow for a monolithic coupling of interface advection and flow equations, which can prevent time step restrictions due to stiff interfacial forces [48].

While phase field methods are state-of-the-art for multi-phase flow problems, there is only a sparse supply of phase field models for FSI, see e.g. [49]. This might be due to the fact, that the interface in phase field methods is diffuse with a finite thickness, making it harder to combine the solid and the fluid material in a consistent way.

This chapter presents an improved phase field method for fluid-structure interaction along with analytical and numerical validation. Physically, the method describes the interaction of a viscous fluid with a viscoelastic solid, including surface tension at the interface in between. In particular, this method can distinguish between three types of solids: purely elastic materials, viscoelastic Maxwell materials, and viscoelastic Kelvin-Voigt materials. The method is capable to handle very large deformations as well as topological changes like contact of the solid to a wall. It is based on a fully Eulerian description of the velocity field in both, the fluid and the elastic domain. Viscous and elastic stresses in the Navier–Stokes equations are restricted to the corresponding domains by multiplication with their characteristic functions. The solid is described as a hyperelastic neo-Hookean material and the elastic stress is obtained by solving an additional Oldroyd-B-like equation. Thermodynamically consistent forces are derived by energy variation. Convergence of the derived equations to the traditional sharp interface formulation of fluid–structure interaction was shown by matched asymptotic analysis in Mokbel et al. [7], which will not be repeated in this chapter. The model is evaluated in a challenging benchmark scenario of an elastic body traversing a fluid channel. A comparison to reference values from arbitrary Lagrangian-Eulerian (ALE) simulations shows very good agreement. Among the distinct advantages of this method is the avoidance of re-triangulations and the stable inclusion of surface tension. Furthermore, contact dynamics can be simply included into the model, as demonstrated by simulating a ball bouncing off a wall. This scenario can be extended to include adhesion of the ball. Although only simulations of fluid-structure interaction problems are presented in this chapter, the model is capable of simulating any combination of viscous fluids, viscoelastic structures, and elastic structures.

It should also be emphasized here that the list of advantages of the present approach has only recently been extended by further studies proving the existence of weak solutions for such a system in two dimensions, see [50], where the authors refer to Mokbel et al. [7].

3.2 Sharp interface model for FSI

In preparation for the formulation of the phase field model, this section first presents the sharp interface equations for FSI. This is an extension of the model in Sec. 2.1, which is written down again here for completeness.

Let the computational domain $\Omega \subseteq \mathbb{R}^d$ be divided into a fluid domain and a solid domain. To be consistent with the phase field model in Mokbel et al. [7], these domains are called Ω_{-1} (fluid) and Ω_1 (solid) in this chapter, in contrast to the notation in Chapter 2. A common velocity field $\mathbf{v} : \Omega \rightarrow \mathbb{R}^d$

is introduced to indicate movements of the fluid and the solid material. Further, the material derivative is denoted by $\partial^\bullet = d_t + \mathbf{v} \cdot \nabla$. Throughout this chapter, incompressible elastic materials are considered, i.e. the Poisson ratio is $1/2$. Balance laws for momentum and mass yield the evolution equations

$$\partial^\bullet(\rho_i \mathbf{v}) = \nabla \cdot \mathbb{S}_i + \mathbf{F} \quad \text{in } \Omega_i \quad (3.1)$$

$$\nabla \cdot \mathbf{v} = 0 \quad \text{in } \Omega_i \quad (3.2)$$

for $i = -1, 1$, where \mathbf{v} , \mathbf{F} , ρ_i and \mathbb{S}_i denote velocity, body force defined in Ω , density in Ω_i and stress in Ω_i , respectively. Note that the ρ_i are both assumed to be constant in space and time.

To describe the elastic stress in the Eulerian framework, the left Cauchy-Green strain tensor \mathbb{B} is introduced. This strain tensor is typically calculated from the deformation gradient tensor \mathbb{F} , as $\mathbb{B} = \mathbb{F}\mathbb{F}^T$. In the present phase field approach, there will be no access to the initial coordinates of a material point to calculate \mathbb{F} . Instead, we use the identity $\partial^\bullet \mathbb{F} = \nabla \mathbf{v}^T \mathbb{F}$ (see e.g. [51]) from which one can easily compute the following evolution equation for \mathbb{B} ,

$$\partial^\bullet \mathbb{B} - \nabla \mathbf{v}^T \cdot \mathbb{B} - \mathbb{B} \cdot \nabla \mathbf{v} = 0 \quad \text{in } \Omega_1. \quad (3.3)$$

Note that a row-wise nabla operator is used here, i.e. $(\mathbb{B} \cdot \nabla \mathbf{v})_{ij} = \mathbb{B}_{ik} \partial_k v_j$. The left-hand side is also known as the upper-convected Maxwell time derivative that rotates and stretches with the deformation. The initial condition for Eq. (3.3) is given by the strain in the undeformed configuration $\mathbb{B} = \mathbb{I}$, where \mathbb{I} is the identity matrix. The corresponding elastic stress for a hyperelastic neo-Hookean material is given by $G(\mathbb{B} - \mathbb{I})$, where G is the shear modulus. In a fluid, the elastic stress vanishes since there is no strain, i.e.

$$\mathbb{B} = \mathbb{I} \quad \text{in } \Omega_{-1} \quad (3.4)$$

for all times. The total phase-dependent stress is then given by the elastic stress plus the fluid stress already introduced in Sec. 2.1,

$$\mathbb{S}_i = G_i(\mathbb{B} - \mathbb{I}) - p\mathbb{I} + \eta_i(\nabla \mathbf{v} + \nabla \mathbf{v}^T), \quad (3.5)$$

where p denotes the pressure defined in Ω , and the constants G_i and η_i denote the shear modulus and the viscosity of the respective phase. In particular $G_{-1} = 0$ in a purely viscous fluid, and $\eta_1 = 0$ if the elastic solid has no additional viscosity.

Finally, two jump conditions are specified at the fluid-solid interface Γ ,

$$[[\mathbf{v}]]_\Gamma = 0, \quad [[\mathbb{S}]]_\Gamma \cdot \mathbf{n} = -\sigma \kappa \mathbf{n}, \quad (3.6)$$

where $[[f]]_\Gamma = f_{-1} - f_1$ denotes the jump in f across the interface and \mathbf{n} is the normal pointing into

Ω_1 . The first condition is the continuity of the velocity. The second condition is the interfacial force balance including a possible surface tension force at the fluid-solid interface with surface tension σ and total curvature κ . Note that in this chapter a constant surface tension is assumed and consequently the Marangoni term $\nabla_{\Gamma}\sigma$ mentioned in Sec. 2.1 is omitted in the second of the above conditions.

3.3 Phase field modeling

The phase field model presented in the following is an extension of the corresponding model in Sec. 2.2. To adopt the notation from Mokbel et al. [7], let ϕ denote a phase field that distinguishes between the fluid domain ($\phi \approx -1$) and the solid domain ($\phi \approx 1$) within a computational domain Ω . Hence the subdomain Ω_i in the sharp interface approach is now approximated by the domain where $\phi \approx i$. Since the phase field approach allows mixing of the two domains in the (narrow) interface region, the velocity field is now defined to be the volume-averaged velocity of this mixture, see Sec. 2.2.5 and [5] for details. The density is chosen as a linear combination of the (constant) densities in the two phases: $\rho(\phi) = \rho_1(1 + \phi)/2 + \rho_{-1}(1 - \phi)/2$. Balance laws for mass and momentum yield the evolution equations for phase field and velocity:

$$\partial^\bullet \phi = -\nabla \cdot \mathbf{j} \quad \text{in } \Omega \quad (3.7)$$

$$\partial^\bullet(\rho(\phi)\mathbf{v}) = \nabla \cdot \mathbb{S}(\phi) + \mathbf{F} \quad \text{in } \Omega \quad (3.8)$$

$$\nabla \cdot \mathbf{v} = 0 \quad \text{in } \Omega \quad (3.9)$$

where the stress depends now on the phase field. The force \mathbf{F} and the flux \mathbf{j} are specified later to meet the requirement of non-increasing energy.

To obtain an equation for the diffuse elastic strain tensor, Eqs. (3.4) and (3.3) need to be combined. A typical approach in phase field modeling is to multiply an equation with a characteristic function of its domain (here: Ω_{-1} or Ω_1) and to extend the domain then to the larger computational domain (here: Ω), see [52]. A similar approach is followed here, i.e. Eq. (3.4) is multiplied with a function $\alpha(\phi)$ and Eq. (3.3) with a function $\lambda(\phi)$. By adding both results, the common equation for the diffuse elastic strain tensor is obtained as

$$\lambda(\phi) (\partial^\bullet \mathbb{B} - \nabla \mathbf{v}^T \cdot \mathbb{B} - \mathbb{B} \cdot \nabla \mathbf{v}) + \alpha(\phi)(\mathbb{B} - \mathbb{I}) = 0. \quad (3.10)$$

For $\alpha = 0$ the equation reduces to the strain evolution for an elastic solid Eq. (3.3), while for $\lambda = 0$ it reduces to the strain description of a fluid, i.e. Eq. (3.4). In case $\alpha = 1$, Eq. (3.10) is also known as Oldroyd-B equation. This equation is used to describe Maxwell-type viscoelasticity with λ being the relaxation time controlling the dissipation of elastic stress. The above generalization of the Oldroyd-B equation to arbitrary α leads to the relaxation time λ/α . Note that this ratio is the only free (spatially varying) parameter of Eq. (3.10), but the introduction of α effectively allows to choose this ratio equal

to infinity in some region of the computational domain by setting $\alpha = 0$ there.

The total phase-dependent stress is then given by

$$\mathbb{S}(\phi) = G(\phi)(\mathbb{B} - \mathbb{I}) - p\mathbb{I} + \eta(\phi)(\nabla\mathbf{v} + \nabla\mathbf{v}^T) \quad (3.11)$$

where $\eta(\phi)$ is the viscosity and $G(\phi)$ is the shear modulus of the respective phase. Note that both \mathbf{v} and p are not assumed to be phase-dependent quantities. For all the phase-dependent quantities, the following linear interpolations are used:

$$\begin{aligned} G(\phi) &= G_1(1 + \phi)/2 + G_{-1}(1 - \phi)/2 \\ \eta(\phi) &= \eta_1(1 + \phi)/2 + \eta_{-1}(1 - \phi)/2 \\ \lambda(\phi) &= \lambda_1(1 + \phi)/2 + \lambda_{-1}(1 - \phi)/2 \\ \alpha(\phi) &= \alpha_1(1 + \phi)/2 + \alpha_{-1}(1 - \phi)/2. \end{aligned}$$

Note that in practice it is often additionally required that $G(\phi) = G_1$ for $\phi > 1$ and $G(\phi) = G_{-1}$ for $\phi < -1$ to limit G to physically reasonable values. The reason is that the phase field does not satisfy a maximum principle, i.e. its values can slightly exceed the interval $[-1, 1]$, which may lead to unphysical values especially for large differences between G_1 and G_{-1} . The same applies to the remaining interpolated quantities.

Modeling the interaction of an elastic solid ($\phi = 1$) with a fluid ($\phi = -1$) is now possible by inserting the given physical parameters for the elastic shear modulus G_1 , the fluid viscosity η_{-1} and setting $G_{-1} = \eta_1 = \alpha_1 = \lambda_{-1} = 0$. It remains to specify α_{-1} and λ_1 which can be interpreted to control the relaxation time in the diffuse interface region where a mixture of fluid and elastic phase is present. Note that due to the structure of Eq. (3.10) the only free parameter here is the ratio λ_1/α_{-1} , which can also be thought of as an interface relaxation time. Obviously, this time has to be scaled somehow with the characteristic time scale T of the considered problem, which suggests to simply use $\lambda_1/\alpha_{-1} = T$, for example by setting $\alpha_{-1} = 1, \lambda_1 = T$. This parameter choice will also be numerically tested in Sec. 5.4.

An overview of the parameters can be found in Tab. 3.1. Note that also viscoelastic material phases can be modeled. For Kelvin-Voigt viscoelasticity it suffices to add a viscosity inside of the elastic material. For Maxwell viscoelasticity one chooses $\alpha_1 = 1$ and just prescribes the Maxwell relaxation time for λ_1 . Hence, any combination of two phases, be it viscous, viscoelastic or solid, can be modeled by choosing the parameters as given in Tab. 3.1.

viscosity	shear modulus	relax. time		corresponding material
$\eta(\phi)$	$G(\phi)$	$\lambda(\phi)$	$\alpha(\phi)$	
*	0	0	1	viscous fluid
0	*	T	0	elastic solid
*	*	T	0	viscoelastic Kelvin-Voigt
0	*	*	1	viscoelastic Maxwell

Table 3.1: Different material laws can be obtained by different choice of parameters. The star symbol ‘*’ marks parameters that are given by the physical problem itself, T indicates the characteristic time scale of the given problem. Adapted from Mokbel et al. [7].

3.4 Energy dissipation

To close the system of equations, it remains to specify the flux \mathbf{j} and force \mathbf{F} to obtain a thermodynamically consistent evolution. The calculation is essentially based on that in Sec. 2.2.5 and this time is extended to include the elastic contribution. For completeness, some intermediate results from Sec. 2.2.5 are mentioned again here. The total energy E_{fsi} of the system is now the sum of kinetic, elastic [53] and diffuse interface energy (cf. Eq. (2.30)), i.e.

$$E_{\text{fsi}} = \underbrace{\int_{\Omega} \frac{\rho(\phi)}{2} |\mathbf{v}|^2}_{E_{\text{kin}}} + \underbrace{\frac{G(\phi)}{2} \text{tr}(\mathbb{B} - \ln \mathbb{B} - \mathbb{I})}_{E_{\text{el}}} + \underbrace{\tilde{\sigma} \left(\frac{\epsilon}{2} |\nabla \phi|^2 + \frac{1}{\epsilon} W(\phi) \right)}_{E^{\phi}} \, \text{d}\mathbf{x}. \quad (3.12)$$

Here, ‘ $\text{tr}(A)$ ’ is the trace of a matrix A , ϵ the interface thickness, W the double-well potential and $\tilde{\sigma}$ the (scaled) surface tension, whose scaling depends on the choice of W (cf. Sec. 2.2.4). The double-well potential is chosen here as $W(\phi) = \frac{1}{4}(1 - \phi^2)^2$, which leads to $\tilde{\sigma} = \frac{3}{2\sqrt{2}} \cdot \sigma$.

3.4.1 Energy time derivative

The time evolution of the energy can now be computed using Eqs. (3.7) - (3.11). The intermediate steps in the computation of the time derivative of both the kinetic energy and the diffuse interface energy can be found in Sec. 2.2.5. After a brief recapitulation of the computational results for these two contributions to the energy evolution, the focus in the following is on the inclusion of the elastic contribution.

At this point it should be noted that the identities Eqs. (2.38) - (2.41) are useful for the computation of the energy time derivative. As in Sec. 2.2.5, boundary integrals that arise from integration by parts are neglected here since appropriate boundary conditions are assumed. Also the assumption of a closed system remains here, i.e. the domain Ω moves with the flow field, which simplifies the calculations since material derivatives appear under the integral. This can be ensured in particular by the boundary condition $\mathbf{v} \cdot \mathbf{n}_{\Omega} = 0$, with \mathbf{n}_{Ω} denoting the outer normal to the domain boundary $\partial\Omega$.

Referring to Eq. (2.42), the **time derivative of the kinetic energy** reads

$$d_t E_{\text{kin}} = \int_{\Omega} -\frac{\eta(\phi)}{2} |\nabla \mathbf{v} + \nabla \mathbf{v}^T|^2 - G(\phi) \mathbb{B} : \nabla \mathbf{v} + \mathbf{v} \cdot \mathbf{F} + \frac{\rho'(\phi)}{2} |\mathbf{v}|^2 \nabla \cdot \mathbf{j} \, \mathrm{d}\mathbf{x}, \quad (3.13)$$

where either no flow across the outer boundary ($\mathbf{v}|_{\partial\Omega} = 0$), or no force, i.e.

$$(\eta(\phi) (\nabla \mathbf{v} + \nabla \mathbf{v}^T) - p\mathbb{I} + G(\phi) (\mathbb{B} - \mathbb{I})) \cdot \mathbf{n}_{\Omega} = 0 \quad \text{on } \partial\Omega,$$

was assumed. Note that the term $G(\phi)\mathbb{B}$ in Eq. (3.13) results from the contribution of elastic stress in Eq. (3.11).

Furthermore, the **time derivative of the diffuse interface energy** (Eq. (2.43)) reads

$$d_t E^{\phi} = \int_{\Omega} -\frac{\delta E^{\phi}}{\delta \phi} \nabla \cdot \mathbf{j} + \mathbf{v} \cdot (\nabla \cdot (\epsilon \tilde{\sigma} \nabla \phi \otimes \nabla \phi)) \, \mathrm{d}\mathbf{x}, \quad (3.14)$$

with $\delta E^{\phi}/\delta \phi := \tilde{\sigma} (-\epsilon \Delta \phi + W'(\phi)/\epsilon)$ denoting the (scaled) variational derivative of the energy, cf. Eq. (2.9). Note that the boundary condition $\mathbf{n}_{\Omega} \cdot \nabla \phi = 0$ on the outer boundary $\partial\Omega$ is used here, which effectively leads to a contact angle of 90° . Other contact angles can be treated by inclusion of a wall energy, see Sec. 2.3.2.

As discussed in [53], $\mathbb{B} \in \mathbb{R}^{d \times d}$ is assumed to be a symmetric positive definite matrix (see [54] for a proof of this property) and therefore the trace of the matrix logarithm $\ln \mathbb{B}$ can be calculated by

$$\mathrm{tr}(\ln \mathbb{B}) = \sum_{i=1}^d \ln \xi_i \quad (3.15)$$

with the eigenvalues ξ_i . The **time derivative of the elastic energy** can be calculated by

$$\begin{aligned} d_t E_{\text{el}} &= \int_{\Omega} \partial^\bullet \left(\frac{G(\phi)}{2} \right) \mathrm{tr}(\mathbb{B} - \ln \mathbb{B} - \mathbb{I}) + \frac{G(\phi)}{2} \partial^\bullet \mathrm{tr}(\mathbb{B} - \ln \mathbb{B} - \mathbb{I}) \, \mathrm{d}\mathbf{x} \\ &\stackrel{(3.7), (2.39)}{=} \int_{\Omega} -\frac{G'(\phi)}{2} \nabla \cdot \mathbf{j} \mathrm{tr}(\mathbb{B} - \ln \mathbb{B} - \mathbb{I}) + \frac{G(\phi)}{2} \mathrm{tr}(\partial^\bullet (\mathbb{B} - \ln \mathbb{B})) \, \mathrm{d}\mathbf{x} \\ &= \int_{\Omega} -\frac{G'(\phi)}{2} \nabla \cdot \mathbf{j} \mathrm{tr}(\mathbb{B} - \ln \mathbb{B} - \mathbb{I}) \, \mathrm{d}\mathbf{x} + \int_{\{\lambda=0\}} \frac{G(\phi)}{2} \mathrm{tr}((\mathbb{I} - \mathbb{B}^{-1}) \partial^\bullet \mathbb{B}) \, \mathrm{d}\mathbf{x} \\ &\quad + \int_{\Omega \setminus \{\lambda=0\}} \frac{G(\phi)}{2} \mathrm{tr}((\mathbb{I} - \mathbb{B}^{-1}) \partial^\bullet \mathbb{B}) \, \mathrm{d}\mathbf{x} \\ &\stackrel{(3.10)}{=} \int_{\Omega} -\frac{G'(\phi)}{2} \nabla \cdot \mathbf{j} \mathrm{tr}(\mathbb{B} - \ln \mathbb{B} - \mathbb{I}) \, \mathrm{d}\mathbf{x} \\ &\quad + \int_{\Omega \setminus \{\lambda=0\}} \frac{G(\phi)}{2} \mathrm{tr} \left((\mathbb{I} - \mathbb{B}^{-1}) \left(\nabla \mathbf{v}^T \cdot \mathbb{B} + \mathbb{B} \cdot \nabla \mathbf{v} - \frac{\alpha(\phi)}{\lambda(\phi)} (\mathbb{B} - \mathbb{I}) \right) \right) \, \mathrm{d}\mathbf{x}. \end{aligned} \quad (3.16)$$

Note that Eq. (3.10) yields the boundedness of the last integrand in the set $\Omega \setminus \{\lambda = 0\}$ given the solution is sufficiently smooth. Summing up the three components yields the variation of the total energy as

$$\begin{aligned} d_t E_{\text{fsi}} &= \int_{\Omega} -\frac{\eta(\phi)}{2} |\nabla \mathbf{v} + \nabla \mathbf{v}^T|^2 - G(\phi) \mathbb{B} : \nabla \mathbf{v} + \mathbf{v} \cdot \mathbf{F} + \frac{\rho'(\phi)}{2} |\mathbf{v}|^2 \nabla \cdot \mathbf{j} \\ &\quad - \frac{G'(\phi)}{2} \nabla \cdot \mathbf{j} \operatorname{tr}(\mathbb{B} - \ln \mathbb{B} - \mathbb{I}) - \frac{\delta E^\phi}{\delta \phi} \nabla \cdot \mathbf{j} + \mathbf{v} \cdot (\nabla \cdot (\epsilon \tilde{\sigma} \nabla \phi \otimes \nabla \phi)) \, d\mathbf{x} \\ &\quad + \int_{\Omega \setminus \{\lambda=0\}} \frac{G(\phi)}{2} \operatorname{tr} \left((\mathbb{I} - \mathbb{B}^{-1}) \left(\nabla \mathbf{v}^T \mathbb{B} + \mathbb{B} \nabla \mathbf{v} - \frac{\alpha(\phi)}{\lambda(\phi)} (\mathbb{B} - \mathbb{I}) \right) \right) \, d\mathbf{x}. \end{aligned} \quad (3.17)$$

In order to reformulate the trace term in the last line, the symmetry of \mathbb{B} and the following properties can be used:

$$\operatorname{tr}(\mathbb{A} \mathbb{B} \mathbb{A}^{-1}) = \operatorname{tr}(\mathbb{B}) \quad \text{for a regular matrix } \mathbb{A} \quad (3.18)$$

$$\operatorname{tr}(\mathbb{A} \mathbb{B}) = \mathbb{A} : \mathbb{B}^T = \mathbb{A}^T : \mathbb{B} \quad (3.19)$$

$$\operatorname{tr}(\nabla \mathbf{v}) = \nabla \cdot \mathbf{v} = 0, \quad (3.20)$$

which yields for $\lambda \neq 0$

$$\begin{aligned} &\operatorname{tr} \left((\mathbb{I} - \mathbb{B}^{-1}) \left(\nabla \mathbf{v}^T \mathbb{B} + \mathbb{B} \nabla \mathbf{v} - \frac{\alpha(\phi)}{\lambda(\phi)} (\mathbb{B} - \mathbb{I}) \right) \right) \\ &\stackrel{(3.18), (3.19)}{=} 2\mathbb{B} : \nabla \mathbf{v} - 2\operatorname{tr}(\nabla \mathbf{v}) - \frac{\alpha(\phi)}{\lambda(\phi)} \operatorname{tr}(\mathbb{B} + \mathbb{B}^{-1} - 2\mathbb{I}) \\ &\stackrel{(3.20)}{=} 2\mathbb{B} : \nabla \mathbf{v} - \frac{\alpha(\phi)}{\lambda(\phi)} \operatorname{tr}(\mathbb{B} + \mathbb{B}^{-1} - 2\mathbb{I}). \end{aligned} \quad (3.21)$$

Note that also the last term of Eq. (3.21) is bounded, which follows from Eq. (3.10) and

$$|\operatorname{tr}(\mathbb{B} + \mathbb{B}^{-1} - 2\mathbb{I})| \leq C \|\mathbb{B} - \mathbb{I}\| \quad (\text{for a constant } C > 0)$$

in a neighborhood of the identity matrix. Moreover, it can be used that

$$\int_{\{\lambda=0\}} G(\phi) \mathbb{B} : \nabla \mathbf{v} \, d\mathbf{x} = \int_{\{\lambda=0\}} G(\phi) (\mathbb{B} - \mathbb{I}) : \nabla \mathbf{v} + G(\phi) \mathbb{I} : \nabla \mathbf{v} \stackrel{(3.20)}{=} 0, \quad (3.22)$$

which exploits the relation $\mathbb{B} = \mathbb{I}$ for $\lambda = 0$.

Equations (3.21) and (3.22) lead to a simplified version of (3.17):

$$\begin{aligned} d_t E_{\text{fsi}} &= \int_{\Omega} -\frac{\eta(\phi)}{2} |\nabla \mathbf{v} + \nabla \mathbf{v}^T|^2 + \mathbf{v} \cdot \mathbf{F} + \frac{\rho'(\phi)}{2} |\mathbf{v}|^2 \nabla \cdot \mathbf{j} - \nabla \cdot \mathbf{j} \frac{\delta E^\phi}{\delta \phi} \\ &\quad - \frac{G'(\phi)}{2} \nabla \cdot \mathbf{j} \operatorname{tr}(\mathbb{B} - \ln \mathbb{B} - \mathbb{I}) + \mathbf{v} \cdot (\nabla \cdot (\epsilon \tilde{\sigma} \nabla \phi \otimes \nabla \phi)) \, d\mathbf{x} \\ &\quad - \int_{\Omega \setminus \{\lambda=0\}} \frac{G(\phi)\alpha(\phi)}{2\lambda(\phi)} \operatorname{tr}(\mathbb{B} + \mathbb{B}^{-1} - 2\mathbb{I}) \, d\mathbf{x}. \end{aligned}$$

A final step in preparing the formulation of force and flux is the following reformulation of the density term in (3.17), applying integration by parts twice and using that $\rho'(\phi)$ is constant:

$$\int_{\Omega} \frac{\rho'(\phi)}{2} |\mathbf{v}|^2 \nabla \cdot \mathbf{j} = \int_{\Omega} -\rho'(\phi) \mathbf{v} \cdot (\nabla \mathbf{v} \cdot \mathbf{j}) = \int_{\Omega} \mathbf{v} \cdot (\nabla \cdot (\rho'(\phi) \mathbf{v} \otimes \mathbf{j})) \, d\mathbf{x}.$$

3.4.2 Force and flux

The argumentation in the previous subsection leads to

$$\begin{aligned} d_t E_{\text{fsi}} &= \int_{\Omega} -\frac{\eta(\phi)}{2} |\nabla \mathbf{v} + \nabla \mathbf{v}^T|^2 \\ &\quad + \mathbf{j} \cdot \nabla \left[\frac{G'(\phi)}{2} \operatorname{tr}(\mathbb{B} - \ln \mathbb{B} - \mathbb{I}) + \tilde{\sigma} \left(\frac{1}{\epsilon} W'(\phi) - \epsilon \Delta \phi \right) \right] \\ &\quad + \mathbf{v} \cdot \left[\mathbf{F} + \nabla \cdot (\rho'(\phi) \mathbf{v} \otimes \mathbf{j}) + \epsilon \tilde{\sigma} \nabla \cdot (\nabla \phi \otimes \nabla \phi) \right] \, d\mathbf{x} \\ &\quad - \int_{\Omega \setminus \{\lambda=0\}} \frac{G(\phi)\alpha(\phi)}{2\lambda(\phi)} \operatorname{tr}(\mathbb{B} + \mathbb{B}^{-1} - 2\mathbb{I}) \, d\mathbf{x} \end{aligned} \quad (3.23)$$

under appropriate boundary conditions. Note that the last term is non-negative for any given tensor \mathbb{B} and bounded as explained in Sec. 3.4.1. Consequently, the choice

$$\mathbf{F} = -\nabla \cdot (\rho'(\phi) \mathbf{v} \otimes \mathbf{j}) - \epsilon \tilde{\sigma} \nabla \cdot (\nabla \phi \otimes \nabla \phi), \quad (3.24)$$

$$\mathbf{j} = -m(\phi) \nabla \left[\frac{G'(\phi)}{2} \operatorname{tr}(\mathbb{B} - \ln \mathbb{B} - \mathbb{I}) + \tilde{\sigma} \left(\frac{1}{\epsilon} W'(\phi) - \epsilon \Delta \phi \right) \right] \quad (3.25)$$

for some mobility function $m(\phi) > 0$ yields the non-increasing energy

$$\begin{aligned} d_t E_{\text{fsi}} &= - \int_{\Omega} \frac{\eta(\phi)}{2} |\nabla \mathbf{v} + \nabla \mathbf{v}^T|^2 + \frac{1}{m(\phi)} |\mathbf{j}|^2 \, d\mathbf{x} \\ &\quad - \int_{\Omega \setminus \{\lambda=0\}} \frac{G(\phi)\alpha(\phi)}{2\lambda(\phi)} \operatorname{tr}(\mathbb{B} + \mathbb{B}^{-1} - 2\mathbb{I}) \, d\mathbf{x} \\ &\leq 0. \end{aligned}$$

A comparison with the corresponding model in Chapter 2 shows that the force given by Eq. (3.24) equals the one given by Eq. (2.46). Moreover, the flux given by Eq. (3.25) is supplemented by an additional contribution compared to the version in Eq. (2.47).

3.4.3 Governing equations

This subsection summarizes the governing equations for the thermodynamically consistent phase field model for fluid-structure interaction. As an extension of the model in Sec. 2.2.6, it describes an incompressible two-phase flow with constant surface tension and phase-dependent density and viscosity. A key advantage of the present model is that it can describe any combination of viscous, viscoelastic and elastic materials by choosing the parameters accordingly, as previously highlighted in Tab. 3.1. The system of equations reads

$$\partial^\bullet(\rho(\phi)\mathbf{v}) + \frac{\rho_{-1} - \rho_1}{2} \nabla \cdot (\mathbf{v} \otimes m(\phi) \nabla q) \quad (3.26)$$

$$-\nabla \cdot (\eta(\phi) (\nabla \mathbf{v} + \nabla \mathbf{v}^T) + G(\phi) (\mathbb{B} - \mathbb{I})) + \nabla p = -\tilde{\sigma} \epsilon \nabla \cdot (\nabla \phi \otimes \nabla \phi), \quad (3.27)$$

$$\nabla \cdot \mathbf{v} = 0,$$

$$\partial^\bullet \phi = \nabla \cdot (m(\phi) \nabla q), \quad (3.28)$$

$$\frac{G'(\phi)}{2} \text{tr}(\mathbb{B} - \ln \mathbb{B} - \mathbb{I}) + \tilde{\sigma} \left(\frac{1}{\epsilon} W'(\phi) - \epsilon \Delta \phi \right) = q, \quad (3.29)$$

$$\lambda(\phi) (\partial^\bullet \mathbb{B} - \nabla \mathbf{v}^T \cdot \mathbb{B} - \mathbb{B} \cdot \nabla \mathbf{v}) + \alpha(\phi) (\mathbb{B} - \mathbb{I}) = 0. \quad (3.30)$$

Note that the (constant) derivative of the density $\rho(\phi) = \rho_1(1 + \phi)/2 + \rho_{-1}(1 - \phi)/2$ with respect to ϕ appears on the left side of Eq. (3.26), cf. Sec. 3.3.

Numerical tests indicate that when the chemical potential q , as defined in Eq. (3.29), is used in the evolution equation of the phase field, the resulting ϕ does not provide a good description of the interface layer because of the contributions of the elastic strain. Since the primary purpose of ϕ is to track the two-phase interface, a simplified version of q is used in the numerical simulations, which omits the strain-dependent terms,

$$q = \frac{1}{\epsilon} W'(\phi) - \epsilon \Delta \phi \quad (3.31)$$

replacing Eq. (3.29). This amounts to a classical advected Cahn-Hilliard equation for ϕ , which is now also independent of the surface tension. Note that the resulting system is no longer variational and does not necessarily decrease the energy. However, this effect tends to be of higher order since, if Eq. (3.31) is used, away from the interface $W'(\phi) = \Delta \phi = 0$ and near the interface ϕ locally equilibrates yielding $W'(\phi) \approx \epsilon^2 \Delta \phi$ and thus $q \approx 0$. Note that, if $q = 0$, then the total energy is non-increasing (i.e. $d_t E_{\text{fsi}} \leq 0$), which follows from Eq. (3.23). Numerical results in this chapter and a comparison with the results of an ALE model will confirm the versatile applicability of this model

variant.

At this point, the reader is referred to Mokbel et al. [7] where relations of the present phase field model in the sharp interface limit (i.e. $\epsilon \rightarrow 0$) are derived with the aid of formal asymptotic expansions. This derivation was kindly provided by Helmut Abels as part of the joint work and is outside the scope of this thesis. Provided that suitable power series expansions exist, the matched asymptotic analysis shows the convergence of the derived equations to the traditional sharp interface formulation of the FSI equations.

3.5 Axisymmetric setup and time-discrete equations

In this chapter, numerical tests will be conducted in an axisymmetric setting. The axisymmetric approach allows 3D simulations using a 2D domain, which reduces computational effort. In preparation, the following shows a corresponding reformulation of the governing system of equations in the time-discrete version.

The introduction of axisymmetry is accompanied by the use of cylindrical coordinates. Thereby the 2D meridian domain

$$\Omega_{2D} = \{(x_0, r) \mid 0 \leq x_0 \leq a, 0 \leq r \leq b\}$$

represents the 3D domain

$$\Omega = \{(x_0, x_1, x_2) \mid x_1 = r \cos(\theta), x_2 = r \sin(\theta), (x_0, r) \in \Omega_{2D}, \theta \in [0, 2\pi)\},$$

see Fig. 3.1 for an illustration. Note that Ω_{2D} defines a rectangular domain with lengths a, b . In the following, all fields are defined on Ω_{2D} . The velocity field on this domain is defined to consist of only axial and radial components $\mathbf{v} = (v_0, v_r)$. The gradient, divergence and Laplace operator in the cylindrical coordinate system are defined by

$$\nabla = (\partial_{x_0}, \partial_r), \quad \tilde{\nabla} \cdot = \left(\partial_{x_0}, \frac{1}{r} + \partial_r \right), \quad \tilde{\Delta} = \tilde{\nabla} \cdot \nabla = \partial_{x_0 x_0} + \partial_{rr} + \frac{1}{r} \partial_r.$$

As derivatives in azimuthal (θ -) direction vanish, the strain tensor assumes the form

$$\mathbb{B} := \begin{pmatrix} B_{00} & B_{01} & 0 \\ B_{10} & B_{11} & 0 \\ 0 & 0 & B_{\theta\theta} \end{pmatrix}.$$

Furthermore, the matrices

$$\mathbb{B}_{2D} := \begin{pmatrix} B_{00} & B_{01} \\ B_{10} & B_{11} \end{pmatrix}, \quad \mathbb{I}_{2D} := \begin{pmatrix} 1 & 0 \\ 0 & 1 \end{pmatrix}$$

are introduced for a shorter notation.

The density ρ is assumed to be constant. Hence, the corresponding term in Eq. (3.26) can be neglected. The lower, upper, right, and left boundaries are denoted by Γ_1 , Γ_2 , Γ_3 and Γ_4 , respectively. In the comparison study with ALE simulations of cells flowing through a channel, the computational domain is moved along with the cell velocity. Therefore, the spatially averaged velocity of the cell, named \mathbf{v}_b , is subtracted from the velocity in the advection terms in Eqs. (3.26), (3.28) and (3.30). This modification helps to reduce the amount of remeshing and also leads to a consistent comparison with the ALE model which also applied such a co-moving grid.

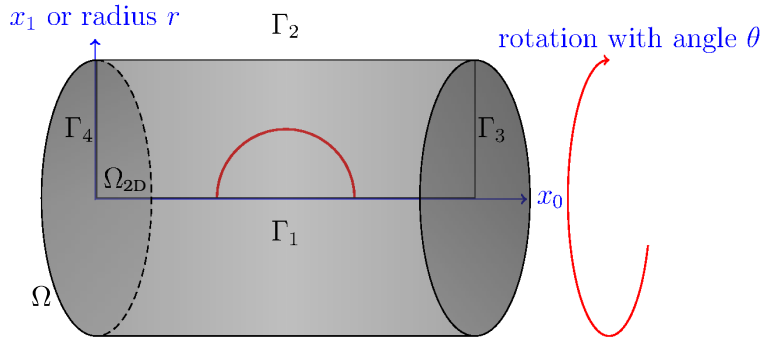


Figure 3.1: Illustration of the axisymmetric computational domain. The boundary line segments Γ_1 to Γ_4 circumscribe the rectangular 2D domain Ω_{2D} . The use of axisymmetric terms in the governing system of equations allows to simulate the flow of an initially spherical object through a cylinder. Adapted from Mokbel et al. [7].

Time discretization

Time-discrete axisymmetric equations can now be formulated for the setup introduced above. Note that the governing system of equations here is a specification of (3.26)-(3.30) with additional axisymmetric terms. Let τ denote the time step size for an equidistant time partitioning. Hereafter, $d_t f^n = (f^n - f^{n-1}) / \tau$ is considered as the discrete time derivative with a scalar variable f and time step index n . The following systems in Ω_{2D} are solved at each time step:

Navier-Stokes system

$$\begin{aligned} & \rho \left(d_t \mathbf{v}^n + (\mathbf{v}^{n-1} - \mathbf{v}_b) \cdot \nabla \mathbf{v}^n \right) + \nabla p^n - \tilde{\nabla} \cdot \left(\eta^{n-1} \left(\nabla \mathbf{v}^n + (\nabla \mathbf{v}^n)^T \right) \right) \\ &= \frac{\eta^{n-1}}{r} \begin{pmatrix} 0 \\ -\frac{2}{r} v_r^n \end{pmatrix} + \tilde{\nabla} \cdot \left(G^{n-1} (\mathbb{B}_{2D}^{n-1} - \mathbb{I}_{2D}) \right) - (\mathbb{B}_{\theta\theta}^{n-1} - 1) \frac{G^{n-1}}{r} \begin{pmatrix} 0 \\ 1 \end{pmatrix} \\ & \quad - \epsilon \tilde{\sigma} \tilde{\nabla} \cdot (\nabla \phi^n \otimes \nabla \phi^{n-1}) \end{aligned} \quad (3.32)$$

$$\tilde{\nabla} \cdot \mathbf{v}^n = 0 \quad (3.33)$$

where $\eta^n = \eta(\phi^n)$, $G^n = G(\phi^n)$.

Cahn-Hilliard system

The Cahn-Hilliard system is split into two second order equations which are assembled together:

$$d_t \phi^n + (\mathbf{v}^n - \mathbf{v}_b) \cdot \nabla \phi^{n-1} - \tilde{\nabla} \cdot (m(\phi^{n-1}) \nabla q^n) = 0 \quad (3.34)$$

$$q^n + \epsilon \tilde{\Delta} \phi^n - \frac{1}{\epsilon} W'(\phi^n) = 0. \quad (3.35)$$

To avoid the nonlinear terms, a Taylor expansion of linear order for $W'(\phi^n)$,

$$\begin{aligned} W'(\phi^n) &= (\phi^n)^3 - \phi^n \\ &\approx 3(\phi^{n-1})^2 \phi^n - 2(\phi^{n-1})^3 - \phi^n, \end{aligned} \quad (3.36)$$

is chosen. Note that the Navier-Stokes and Cahn-Hilliard system are fully coupled here, due to the appearance of ϕ^n in (3.32) and \mathbf{v}^n in (3.34). Consequently, the systems are assembled and solved monolithically. This coupling is adopted from [48, Sec. 4.1] and relaxes the stiffness of surface tension forces.

Oldroyd-B system

Based on the calculated solution of the Navier-Stokes and Cahn-Hilliard systems at the current time step n , the Oldroyd-B system can be solved separately at the same time step:

$$\begin{aligned} & \lambda(\phi^n) \left(d_t \mathbb{B}_{2D}^n + (\mathbf{v}^n - \mathbf{v}_b) \cdot \nabla \mathbb{B}_{2D}^n - \nabla \mathbf{v}^n \cdot \mathbb{B}_{2D}^{n-1} - \mathbb{B}_{2D}^{n-1} \cdot (\nabla \mathbf{v}^n)^T \right) \\ &= D (\Delta \mathbb{B}_{2D}^n - \Delta \mathbb{B}_{2D}^{n-1}) - \alpha(\phi^n) (\mathbb{B}_{2D}^n - \mathbb{I}) \end{aligned} \quad (3.37)$$

$$\begin{aligned} & \lambda(\phi^n) \left(d_t \mathbb{B}_{\theta\theta}^n + (\mathbf{v}^n - \mathbf{v}_b) \cdot \nabla \mathbb{B}_{\theta\theta}^n - 2 \frac{v_r^n}{r} \mathbb{B}_{\theta\theta}^{n-1} \right) \\ &= D (\Delta \mathbb{B}_{\theta\theta}^n - \Delta \mathbb{B}_{\theta\theta}^{n-1}) - \alpha(\phi^n) (\mathbb{B}_{\theta\theta}^n - \mathbb{I}). \end{aligned} \quad (3.38)$$

Note that (3.37) - (3.38) express five equations for the five unknowns of the elastic stress tensor, one of which is redundant due to symmetry of \mathbb{B}_{2D} . A small artificial diffusion term has been added to ensure numerical stability, whereupon natural no-flux boundary conditions emerge. The diffusion parameter is set to $D = 2 \cdot 10^{-10} \text{ m}^2$ in the numerical tests in the following section.

3.6 Numerical tests

Numerical tests are indispensable to validate numerical models and to assess their accuracy. Nowadays, a standard benchmark for fluid-structure interaction is the Turek-Hron channel flow [55, 56], which induces oscillations of a thin elastic bar attached to a rigid object. Obviously, the phase field model is not well suited to represent such a thin structure, since the corresponding interface thickness would be required to be much thinner than the structure itself, resulting in an extremely fine grid and very high computational costs. Consequently, a different benchmark system is chosen here that serves the current purpose of testing the phase field model in a practically relevant situation.

In particular, the flow of a deforming solid ball through a fluid-filled channel is considered. This offers at least two benefits. Firstly, it highlights the ability of interface capturing methods to account for movements of the solid and fluid domains with respect to each other. Secondly, the test scenario is based on a physically relevant simulation of biological cells traversing a flow channel. Cells are approximated as homogeneous incompressible elastic solids surrounded by a cortex with an active surface tension. While this active tension is neglected in the benchmark stage, it will be added to the model later to illustrate the opportunity of phase field models to stabilize the stiffness arising between interface advection and surface forces [48].

Note that many typical modeling approaches consider cells as fluid-filled elastic membranes, see for example [57]. While the approximation as a membrane is a valid choice for red blood cells whose bulk is relatively soft, the focus here is on most other animal cell types whose mechanical response is dominated by the elasticity of the cell bulk. Such cells are also often immersed in a liquid environment in biological processes as well as in biotechnical applications, for example for ultra-fast identification of cell mechanical properties [58], which serves as a reference for this benchmark.

3.6.1 Test setup

The benchmark simulations assume an initially spherical solid object, also referred to as a *cell*, flowing through a fluid-filled channel. To be consistent with the reference simulations [58], the solid object and the channel are considered to be axisymmetric. Axisymmetry effectively reduces the problem to a two-dimensional flow with axisymmetric operators. For this purpose, the corresponding setup of Sec. 3.5 is used here. Accordingly, Ω_{2D} denotes the computational domain, which is a two-dimensional rectangle whose lower boundary represents the symmetry axis, see Fig. 3.1 for an illustration. Here, $\Omega_{2D} = [0, 40] \mu\text{m} \times [0, 10] \mu\text{m}$ which corresponds to a cylindrical channel of radius $10 \mu\text{m}$, see Fig. 3.2

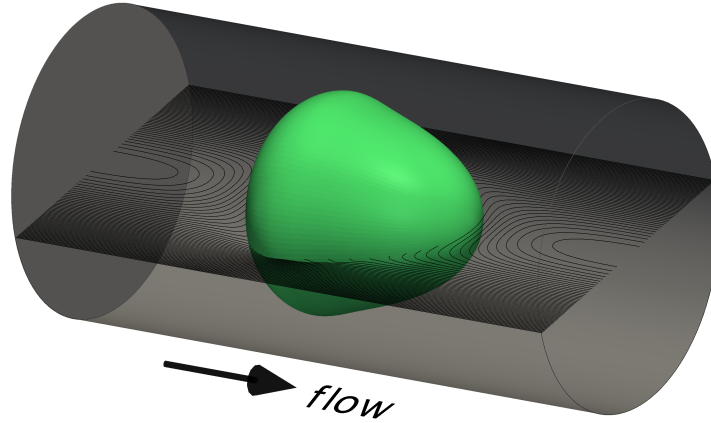


Figure 3.2: Illustration of the simulated scenario. An initially spherical elastic cell (green) is deformed by pressure and shear forces as it flows through a fluid-filled cylindrical channel. Streamlines (black) visualize fluid movement relative to cell velocity. From Mokbel et al. [7].

for an illustration of the benchmark test scenario.

Surface tension forces are neglected at first, since the fluid-structure part of the method is to be benchmarked. Moreover, the following physical parameters are chosen for the simulations:

$$\eta_1 = \eta_{-1} = 10 \text{ Pa} \cdot \text{s}, \quad \rho_1 = \rho_{-1} = 1000 \frac{\text{kg}}{\text{m}^3}, \quad G_{-1} = 0.$$

The shear modulus of the cell, G_1 , is related to its Young's modulus E by $E = 3G_1$. Different values of E are used in the tests. The radius of the initially spherical cell is set to $R = 6 \mu\text{m}$.

Unless otherwise stated, the standard model parameters are $\epsilon = 0.0125 \mu\text{m}$ and constant mobility $m(\phi) = 10^{-8} \text{ m}^3\text{s/kg}$. The characteristic time scale of the considered problem is approximately $T = 1 \text{ ms}$. The parameters for the Oldroyd-B equation are chosen accordingly

$$\alpha_1 = 0, \quad \alpha_{-1} = 1, \quad \lambda_1 = 1 \text{ ms}, \quad \lambda_{-1} = 0,$$

as suggested in Tab. 3.1. Note that the only free parameter here is λ_1 and the influence of variations in λ_1 will be evaluated later in the numerical tests.

Boundary conditions

The following boundary conditions apply for the velocity:

$$\mathbf{v} = 0 \quad \text{on } \Gamma_2, \quad (3.39)$$

$$v_r = 0 \quad \text{on } \Gamma_1, \quad (3.40)$$

see Fig. 3.1 for the denotations. Equation (3.39) corresponds to a no-slip condition at the channel wall and (3.40) avoids a radial flow at the symmetry axis. In the case of channel flow, periodic boundary conditions apply for \mathbf{v} on Γ_4 and Γ_3 , as well as the boundary conditions

$$p = 0 \quad \text{on } \Gamma_3, \quad (3.41)$$

$$p = p_0 \quad \text{on } \Gamma_4, \quad (3.42)$$

where $p_0 > 0$ imposes the desired pressure difference between Γ_4 and Γ_3 driving the flow through the channel. As for the velocity, periodic boundary conditions are given for all fields but the pressure on Γ_3 and Γ_4 , which effectively leads to a channel of infinite length. No-flux conditions for the Cahn-Hilliard system are used on the other boundaries.

The initial pressure difference between the channel inlet and outlet is set to $p_0 = 2500$ Pa. This pressure difference is adapted during the simulation such that a constant flow rate of $4e-11$ m³/s appears, see [58] for details on the adaption algorithm. Note that in this sense Eq. (3.42) is an initial boundary condition for the channel inlet, while the zero-pressure condition for the outlet Eq. (3.41) holds throughout the runtime of a simulation.

Numerical framework

The problem is discretized in the finite element toolbox AMDiS [59, 60] with an adaptive mesh refinement strategy. Coarsening and refinement of the mesh are controlled by the phase field function such that the region $\phi \in [-0.9, 0.9]$ is resolved by at least five degrees of freedom across the interface. Away from the interface the fixed grid size $h = 0.625$ μm is chosen. P1 finite elements are used for the pressure and P2 elements for the other variables.

In the numerical tests below, at each time step, a system is solved for approximately 230,000 degrees of freedom (in total for all solution variables). In an exemplary case, the computational costs on a single core amounted to approximately 18 seconds per time step (including the time for remeshing), referring to Fig. 3.4(a) with $\epsilon = 2.5e-8$ m. The duration of the complete simulation depends on the chosen time step size τ . In the mentioned case, it was set to $\tau = 5e-7$ seconds, and the obtained duration was about 14 hours.

3.6.2 Benchmark quantity

After being deformed by pressure and shear forces, the solid will assume a stationary shape whereupon its flow becomes purely translational. We aim in particular to reproduce this state of stationary deformation. Note that this is a highly challenging problem for a phase field method, since the structure needs to resist any movement, while the fluid keeps flowing around it and continuous movement takes place, even in the diffuse interface.

In order to quantify the stationary deformation, let it be defined by

$$\text{deformation} = 1 - \text{circularity} = 1 - \frac{2\sqrt{A\pi}}{P},$$

where A and P denote the area and the perimeter of the 2D view of the deformed object, measured by a piecewise linear approximation of the zero-level of ϕ . This definition of a deformation provides a measure of the deviation of the cell shape from a circle. It has been shown in [58] that it is a delicate measure that can be uniquely related to the exact elastic modulus of the cell. This quantity is therefore used here as a main indicator for comparison of the phase field model with the ALE reference solution.

Reference values for the stationary cell shapes are given in [58] for various cell sizes, flow rates and elastic moduli. There, an ALE method was employed using a co-moving grid to keep the cell in the center of the computational domain throughout the simulation. The data in [58] has been shown to be extremely accurate in terms of spatial and temporal discretization errors and has been widely used for comparisons to corresponding experiments. The experimental technique, called Real-Time-Deformability Cytometry (RT-DC), can be used to probe mechanical properties of biological cells in flow [61]. A validation study with purely elastic spherical particles showed very good agreement between ALE simulations and experiments.

3.6.3 Simulation results

This section provides a comparison of the phase field method presented in this chapter with the ALE reference data and performs a parameter study to justify the choice of λ_1 , ϵ and m , respectively.

Fig. 3.2 illustrates the idea of the actually simulated 3D scenario. It shows a stationary state shape in the cylinder, together with the streamlines of the flow. Fig. 3.3 presents the cell shape for different times. The initially spherical cell deforms due to fluid pressure and shear forces until it assumes a quasi-stationary state. A comparison with the ALE reference shape shows excellent agreement (Fig. 3.3, right).

Fig. 3.4 shows the corresponding evolution of the cell deformation. Fig. 3.4(a) investigates the dependence of the deformation evolution on the interface width ϵ . The deformation decreases with decreasing ϵ , and very good agreement with the ALE reference value is already found for the smallest values of ϵ . However for $\epsilon \rightarrow 0$ the deformation seems to converge to a value smaller than the reference solution. This is not surprising since, according to Sec. 2.2.6, convergence to the sharp interface limit is achieved only when the constant mobility is decreased proportionally to ϵ (cf. Eq. (2.53)). Note that the mobility controls the intrinsic Cahn-Hilliard dynamics that aims to reduce the surface and therefore decreases deformation.

Accordingly, the sensitivity of the results is tested with respect to changes in the mobility in Fig. 3.4(b).

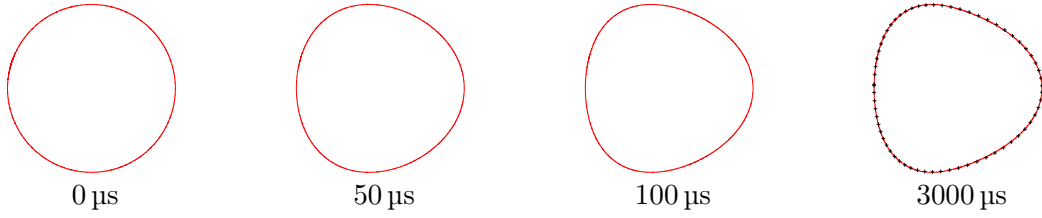


Figure 3.3: Cell shape at different times with Young’s modulus $E = 6 \text{ kPa}$ and initial cell radius $R = 6 \mu\text{m}$, which corresponds to the parameter set discussed in Fig. 3.4. Remarkable changes of the shape occur within the first $100 \mu\text{s}$. The last image compares the stationary shape of the phase field method with the ALE reference shape (black crosses). Image from Mokbel et al. [7].

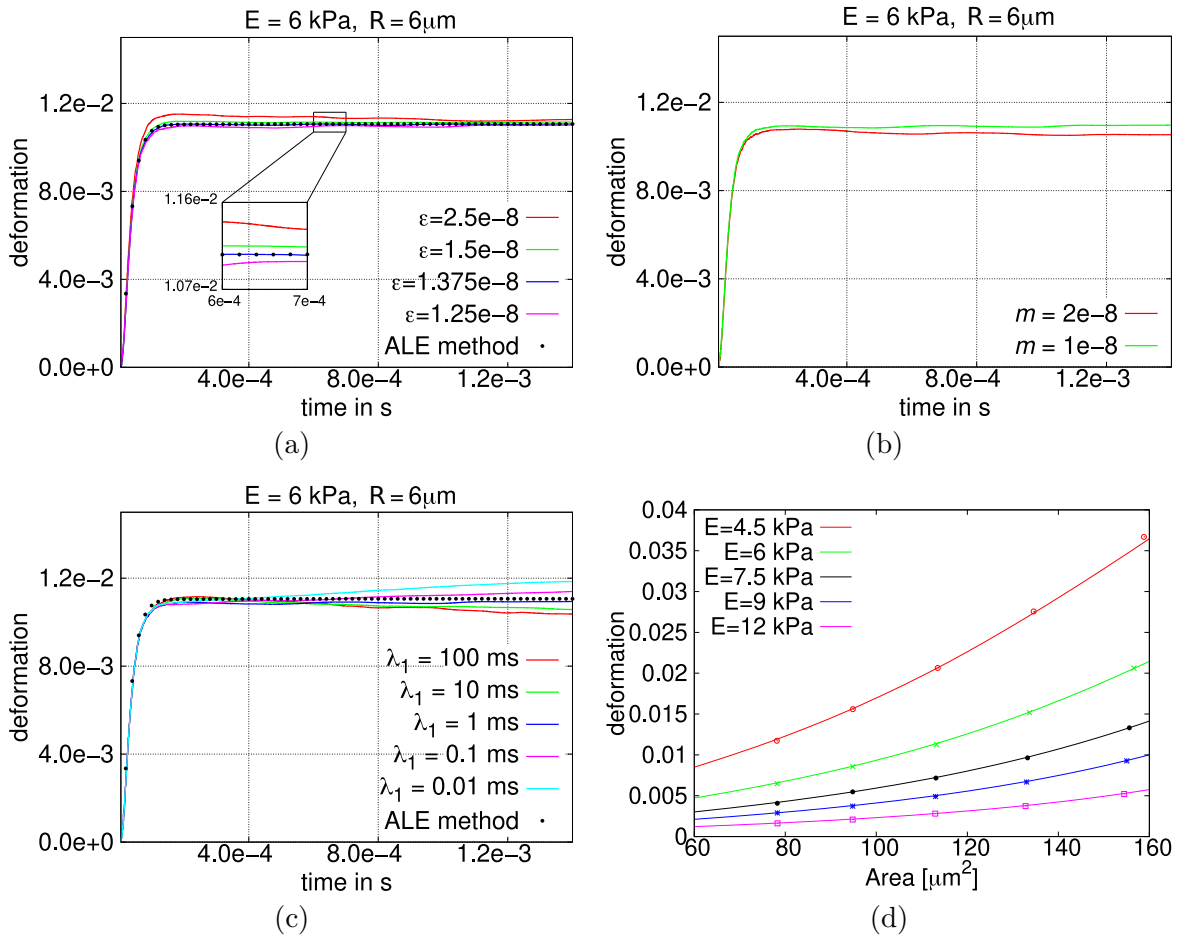


Figure 3.4: Cell deformation in comparison to ALE reference values for varying parameters. Parts (a)-(c) assume the fixed physical parameters $E = 6 \text{ kPa}$, $R = 6 \mu\text{m}$. The standard model parameters are $\lambda_1 = 1 \text{ ms}$, $\epsilon = 1.25 \cdot 10^{-8} \text{ m}$ and $m = 10^{-8} \text{ m}^3\text{s/kg}$. One of these parameters is varied to investigate the influence of interface thickness ϵ (a), mobility m (b) and interfacial relaxation time λ_1 (c). Part (d) provides stationary deformation values at $t = 1.4 \text{ ms}$ for different cell sizes and elastic moduli. Lines depict the reference results of the ALE method and marker points represent those of the present phase field method. Adapted from Mokbel et al. [7].

As expected, higher mobility leads to a decrease in the steady-state deformation. But the quantitative effect of the Cahn-Hilliard dynamics is relatively low, as the deformation curve changes only slightly when the mobility is doubled.

Next, the only free parameter in the Oldroyd-B equation λ_1 is varied. It turns out that small variations of λ_1 have almost no influence on the evolution and steady state of the cell shape. To push the model to its limits, λ_1 is varied across several orders of magnitude in Fig. 3.4(c). This leads for very small λ_1 to a continuous increase of the cell deformation without reaching a stationary state. In this case, the very small value of λ_1 results in a very small relaxation time in the diffuse interface region and hence to a large dissipation of elastic stress there. The drop in elastic stress causes the cell to become increasingly deformed. On the other hand, when λ_1 is very large, a small amount of elastic stress from the diffuse interface may accumulate in the fluid, leading to increased stiffening of the fluid and a decrease in cell deformation. It can be concluded that the parameter λ_1 has to be carefully chosen with a good choice being in the range of the problem's characteristic time scale.

Finally, Fig. 3.4(d) shows that the results of the phase field method are accurate over a range of cell sizes and elastic moduli. Here, cells of five different sizes were simulated in the range $\approx 77 \mu\text{m}^2$ to $160 \mu\text{m}^2$. Five different values for the Young's modulus between 4.5 kPa and 12 kPa were chosen for each cell size. As seen in Fig. 3.4(d), the stationary deformation values of the phase field method are in excellent agreement with the ALE reference values.

3.7 Illustration of the method's potential

This section provides further simulation studies in order to illustrate the potential of the presented phase field FSI model. The scenario of a cell in a cylindrical channel is retained here at first, but this time with the inclusion of surface tension. This demonstrates the model's capability to simulate elastic bodies with strong surface tension, as they are common in biological applications. Therefore, three different values for the surface tension are chosen: $\sigma = 5\text{e-}4 \text{ N/m}$, $\sigma = 1\text{e-}3 \text{ N/m}$ and $\sigma = 5\text{e-}3 \text{ N/m}$. Further parameters are the Young's modulus $E = 3 \text{ kPa}$ and the cell radius $R = 6 \mu\text{m}$. Fig. 3.5 shows that the surface tension has a strong influence on the stationary cell shape, which varies from triangular ($\sigma = 5\text{e-}4 \text{ N/m}$) to almost circular ($\sigma = 5\text{e-}3 \text{ N/m}$). The stiff surface tension forces are treated here with a monolithic coupling of the interface advection and flow equations which relaxes any related time step restrictions [48, Sec. 4.1].

A next step is the simulation of the inflow and outflow of the cell. Such simulations are of great interest for biotechnological applications as the dynamics of cell deformation provides additional information on the cell's state. The setting includes a realistic computational channel domain with a conical

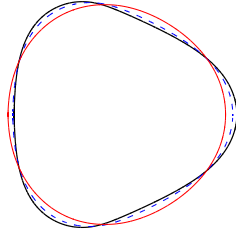


Figure 3.5: Comparison of the steady state shapes for varying surface tension: $\sigma = 5e-4$ N/m (black), $\sigma = 1e-3$ N/m (blue dashed), $\sigma = 5e-3$ N/m (thin red). From Mokbel et al. [7].

inlet/outlet of 45° [61]. The chosen parameter set is:

$$E = 1.5 \text{ kPa}, \quad \sigma = 1e-3 \text{ N/m}, \quad \lambda_1 = 1 \text{ ms}, \quad m = 10^{-8} \text{ m}^3\text{s/kg},$$

$$\text{cell radius } R = 8 \text{ }\mu\text{m}, \quad \epsilon = 0.1 \text{ }\mu\text{m}.$$

As for the cylindrical domain, a pressure difference is implemented between the left and the right boundary, which induces the flow. Fig. 3.6 shows a cut through the computational domain, the initial cell position and various cell shapes during the traversal of the channel.

The deformation curve in Fig. 3.6 shows a strong increase of cell deformation (elongation) during inflow, followed by a drop in deformation as soon as the cell is completely within the cylindrical part of the channel. The elongated cell almost approaches a stationary shape around $t = 2$ ms, but as it is already close to the outlet, the stationary state is never reached. Instead the cell starts to become shorter and wider. This leads to a drop in the deformation, followed by a peak when the cell reaches a maximum thickness and an oblate shape as it leaves the cylindrical channel. Afterwards, the cell relaxes back to a sphere.

Note that such simulations are typically challenging for ALE methods as re-triangulations and interpolations are needed to reconnect the different grids while they move past each other. The present phase field model needs neither re-triangulations nor interpolations to simulate this test case.

The final step is to illustrate the capability of the phase field method to deal with contact between an elastic material and a rigid wall. This is realized by simulating a bouncing elastic ball immersed in a fluid. The fluid fills a cylindrical column of height $40 \text{ }\mu\text{m}$ and radius $10 \text{ }\mu\text{m}$. The ball of radius $R = 6 \text{ }\mu\text{m}$ is initially placed in the middle of the column. The parameters for this test are

$$\eta_1 = 4 \text{ }\mu\text{Pa} \cdot \text{s}, \quad \eta_{-1} = 10 \text{ }\mu\text{Pa} \cdot \text{s}, \quad E = 500 \text{ Pa}, \quad \rho_1 = 1000 \text{ kg/m}^3,$$

$$\rho_{-1} = 100 \text{ kg/m}^3, \quad \lambda_1 = 1 \text{ ms}, \quad \epsilon = 0.2 \text{ }\mu\text{m}, \quad m = 2 \cdot 10^{-9} \text{ m}^3\text{s/kg}.$$

A gravity force of magnitude $10^3 \text{ m/s}^2 \rho(\phi)$ is included to make the ball fall down. A no-slip condition

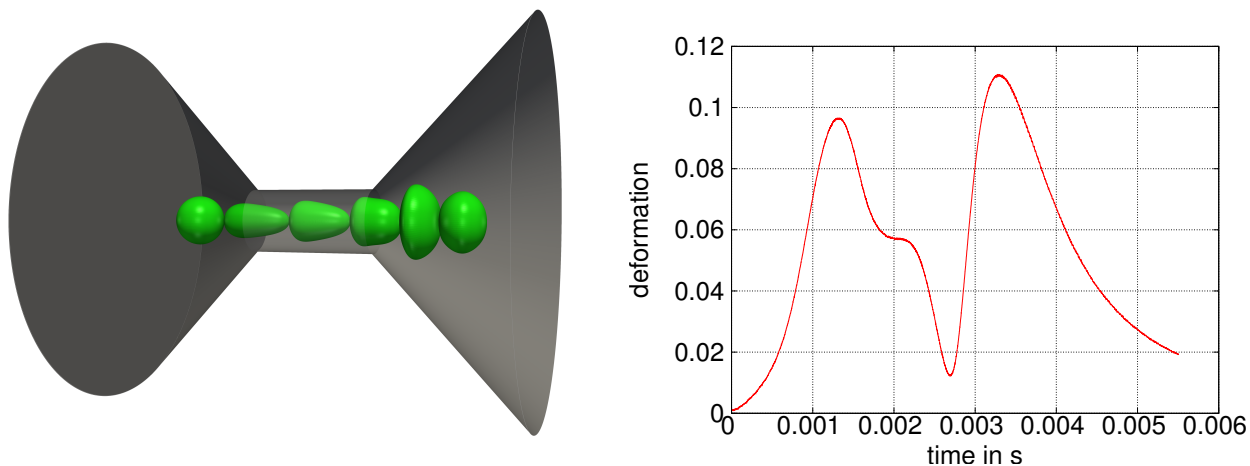


Figure 3.6: Simulation of cell inflow/outflow in a modified channel geometry. The length of the narrow cylindrical channel is $40\ \mu\text{m}$. **Left:** Snapshots of cell shapes at $t = 0\ \text{ms}$, $1.25\ \text{ms}$, $1.927\ \text{ms}$, $2.595\ \text{ms}$, $3.6\ \text{ms}$, $5.509\ \text{ms}$. **Right:** Cell deformation over time. From Mokbel et al. [7].

$\mathbf{v} = 0$ is specified at the top and bottom boundary of the liquid column. An additional non-wetting condition, $\phi = -1$, on all domain boundaries ensures that the ball is repelled from the boundaries. A free-slip condition is imposed at the sides of the column.

Snapshots of the simulation results are shown in Fig. 3.7. The ball and the fluid around it are accelerated as the ball starts falling in the beginning of the simulation. Around $t = 0.18\ \text{ms}$ the ball ‘touches’ the rigid wall whereupon it is compressed in the direction of motion. After the maximum compression is reached at around $t = 0.2\ \text{ms}$, the stored elastic energy is transformed into kinematic energy and the ball starts jumping upwards. This bouncing up and down is repeated several times, but quickly damped due to the viscosity of the surrounding fluid, such that the ball assumes a resting position ‘lying’ on the rigid wall.

Note that no special treatment is needed to realize the contact dynamics here. The only thing is the non-wetting condition, $\phi = -1$, which needs to be imposed at the contact boundary.

Next, the simulation is extended even further by adding adhesion of the ball to the substrate (wall). Adhesive behavior is not only typical for fluids but also for some solid objects, like biological cells. Adhesion appears as soon as the surface tension σ_{ws} between the wall and the solid object is lower than the fluid-solid surface tension σ . According to the Young’s equation (see Sec. 2.3) the balance of surface energies leads to the contact angle θ with $\cos\theta = (\sigma_{wf} - \sigma_{ws})/\sigma$, where σ_{wf} is the wall-fluid surface tension. The contact angle can be included by the Neumann boundary condition $\mathbf{n} \cdot \nabla\phi = \cos\theta \cdot (1 - \phi^2)/(\sqrt{2}\epsilon)$, which can be derived by adding a wall potential to the system energy, cf. Sec. 2.3.3.

The simulation of the bouncing ball is repeated now with this new boundary condition to model

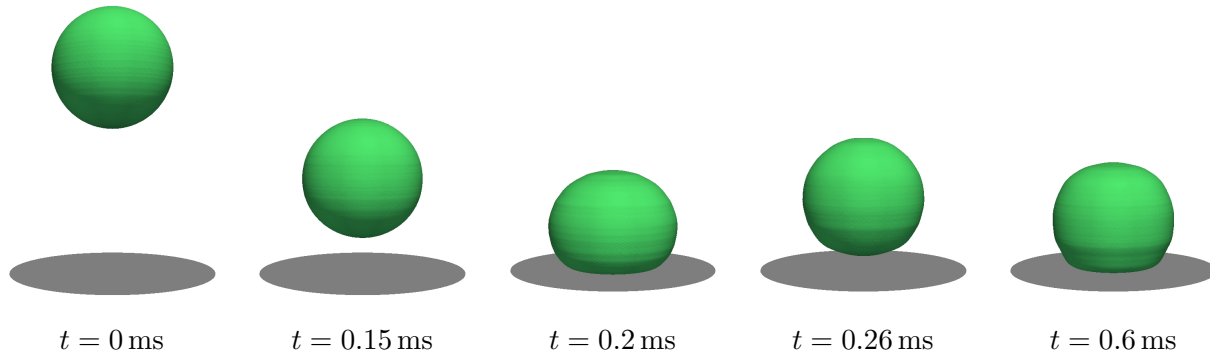


Figure 3.7: Simulation snapshots of an elastic ball bouncing off a rigid wall at different times. From Mokbel et al. [7].

adhesion. The parameters are as before, except for the mobility which is increased by a factor of 40 to overcome the typical stress singularity at the contact line and obtain the correct contact angles, see [17] for a discussion. Fig. 3.8 shows the corresponding time evolution for three contact angles. For the smaller contact angles ($\theta = 45^\circ, 90^\circ$) the ball starts to adhere immediately after the first contact with the wall. Still, the ball is compressed shortly after contact and the elastic energy is released by lifting the ball up. But this time the ball remains bound to the wall and the oscillations are even more quickly damped. The ball develops an almost stationary position around $t = 0.4$ ms. In case of the larger contact angle, $\theta = 135^\circ$, the adhesion is too weak to keep the ball at the wall after first contact, which leads to the same bouncing as previously observed for the no-contact case.

3.8 Conclusion

This chapter presented the novel phase field model for fluid-structure interaction from Mokbel et al. [7]. The model is based on a monolithic Navier–Stokes equation that solves for the velocity field in both, the fluid and the elastic domain. Viscous and elastic stresses are restricted to the corresponding domains by multiplication with their characteristic functions. To obtain the elastic stress, an additional Oldroyd-B-like equation is solved including an interfacial relaxation time. To close the system of equations, globally thermodynamically consistent forces and fluxes were derived using energy variation arguments. Matched asymptotic analysis, not presented here but in [7], shows the convergence of the derived equations to the traditional sharp interface formulation of FSI equations.

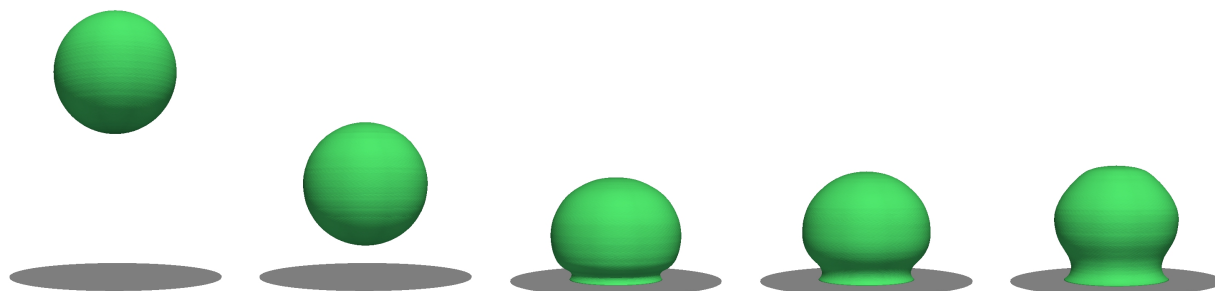
Several numerical tests were conducted to validate the applicability and accuracy of the new model. A challenging benchmark scenario of an elastic cell traversing a fluid channel was employed and results are compared to reference values from ALE simulations [58]. This resulted in very good agreement for various cell sizes and elastic moduli. In particular, it was shown that the interface thickness ϵ and the mobility m are small enough to influence the results only marginally. Results were also shown to be robust with respect to the introduced interfacial relaxation time.

The final focus was on highlighting some distinct advantages of the new model as compared to traditional ALE approaches for FSI. The movement of a solid object through a fluidic channel without grid re-triangulations was demonstrated. Furthermore, strong surface tension forces were included into the model, whose stable discretization is one of the advantages of phase field models. At last, it was shown how easy it is to incorporate contact dynamics into the model by simulating a ball bouncing off a wall. The argumentation concluded with the simulation of adhesion of an elastic ball to a rigid wall, a scenario that, to the author's knowledge, could not be simulated by any other FSI model prior to the publication of Mokbel et al. [7].

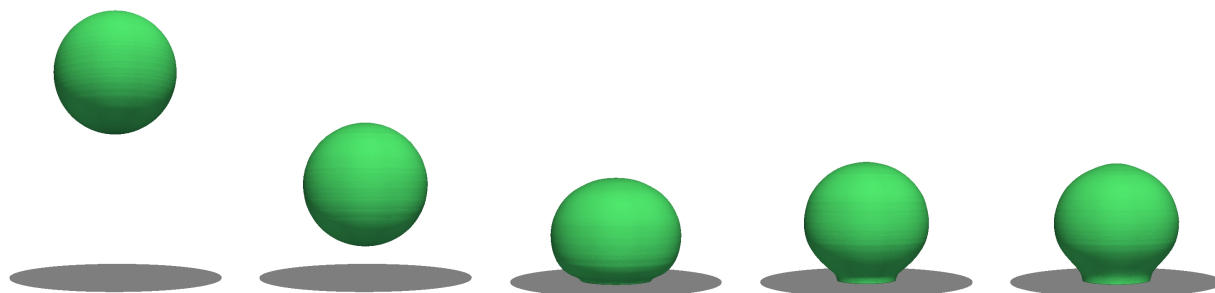
While the simulations were restricted to fluid-structure interaction in this chapter, the model is capable to simulate any combination of viscous fluids, viscoelastic structures and purely elastic structures. The proposed phase field model is therefore well suited to tackle a range of complicated multiphysics problems in the future.

A specific application case using the model is discussed in the context of a ternary FSI problem in the following chapter.

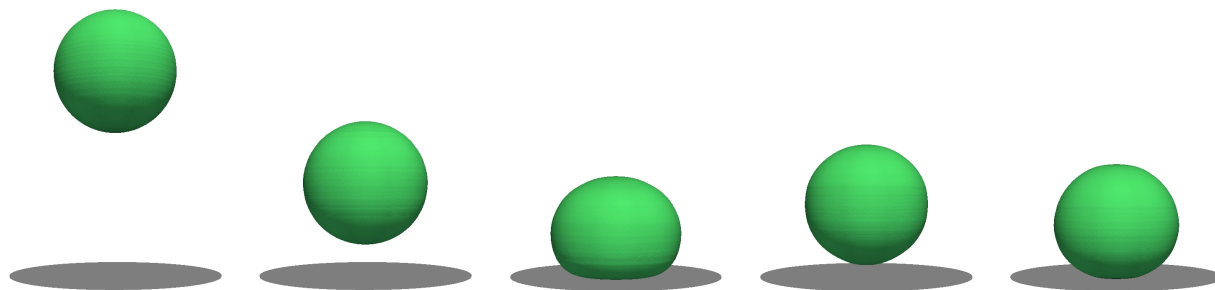
contact angle $\theta = 45^\circ$



contact angle $\theta = 90^\circ$



contact angle $\theta = 135^\circ$



$t = 0$ ms

$t = 0.15$ ms

$t = 0.2$ ms

$t = 0.26$ ms

$t = 0.4$ ms

Figure 3.8: Simulation snapshots of an adhesive elastic ball bumping into a rigid wall. The adhesive properties are determined by the involved surface energies through the contact angle θ (see text). From Mokbel et al. [7].

Chapter 4

Phase field coupled to a rigid body: A ternary FSI approach for atomic force microscopy (AFM)

This chapter presents an application of the model from Chapter 3. In contrast to the two-phase setting in the latter chapter, the model will now be extended to simulate a ternary FSI scenario. More precisely, it treats the interaction between a rigid body, a (visco-)elastic solid and a fluid, as illustrated earlier in the left part of Fig. (2.5). This setup enables simulations of atomic force microscopy (AFM) experiments [62], which are briefly described in Sec. 4.1.

The content presented here was previously published by the author in [9] as a joint work with Shada Abuhattum, where an explicit model capable of extracting viscoelastic properties of cells was developed. For this purpose, numerical simulations were performed together with AFM experiments, the latter kindly provided by Shada Abuhattum along with the biological insights. These experimental and biological aspects are also presented in this chapter to demonstrate the potential of the mathematical model from Chapter 3. The present content differs only slightly from [9] in terms of notation and structure. However, background information on resources and experimental and statistical methods are not discussed here, and the reader is referred to [9] in this regard.

The following introduction also includes an overview of the structure in this chapter.

4.1 Introduction

The viscoelastic behavior of soft materials, especially cells and tissues, has been extensively investigated due to its importance in many biological and physiological processes that take place during development and even disease [63, 64, 65]. Many techniques are used to quantify the mechanical

properties of cells, among them micropipette aspiration [66], optical stretching [67], deformability cytometry [61] and atomic force microscopy (AFM)[62]. The AFM, in particular, is still nowadays one of the most popular methods due to its conformity with various material types and geometries and the rather simple analysis process of the material properties.

For a typical AFM indentation measurement, a cantilever, with a distinct tip shape, moves towards the sample with a predefined velocity and indents it until a prescribed force is reached. The cantilever then moves upwards while detaching from the sample. The deflection and displacement signals of the cantilever are processed further to extract the mechanical properties of the sample. Generally, a Hertzian model is fitted to the approach part of the force-indentation curves to quantify the apparent Young's modulus [68]. When applying the Hertzian model, several assumptions need to be considered, such as the material being homogeneous, isotropic and linearly elastic. Cells and tissues, however, show not only elastic but viscous behavior that is evident from the hysteresis between the approach and retraction segments of the force-indentation curve. Consequently, assessing this viscoelastic behavior is imperative for understanding the complex nature of biological matter [69, 70].

A number of studies utilized AFM to measure the viscoelastic properties of cells in both time and frequency domains, see e.g. [65, 70, 71, 72, 73, 74]. Ideally, to investigate the whole range of the viscoelastic behavior one needs to probe the material for a long time and observe its response or apply oscillatory signals and evaluate its phase lag. These approaches require the user to alter the probing method and add several steps to account for the time-dependent drift or the effect of the hydrodynamic drag of the surrounding medium. On top of that, in many studies the biological materials were probed with a linear approach followed by immediate retraction movement [75, 76, 77]. The force-indentation curves from these studies were used to evaluate the apparent elastic modulus of the probed material using the standard Hertzian model. However, additional information concerning energy dissipation can still be extracted from the same curves to evaluate the viscoelasticity of the material.

This chapter proposes a new fitting model to extract the viscoelastic properties of soft materials from AFM force-indentation curves. Sec. 4.2 starts with the mathematical model, referring to Chapter 3, and the setup for the present simulations. Afterwards, Sec. 4.3.1 provides a validation of the extended numerical model. In particular, the effect of viscoelasticity on force-indentation curves is discussed. As a basis for the construction of the fitting model, a combination of Maxwell and Kelvin-Voigt models is developed to describe soft materials. Numerical simulations of the indentation of such a material with a spherical indenter are then performed. It turns out that the proposed Kelvin-Voigt-Maxwell (KVM) model adequately captures the force-indentation curves of materials with different mechanical characteristics. Furthermore, the numerical results lead to the proposal of an explicit force-indentation relation (i.e. the new fitting model), see Sec. 4.3.2. This explicit relation simplifies the association of the mechanical properties with physically meaningful components and processes. Finally, the developed model is applied to a number of samples, including poroelastic and viscoelastic hydrogels in Sec. 4.4.1 as well as HeLa cells in two different cell cycle phases, interphase and mitotic, see Sec. 4.4.2. It will

be demonstrated that the distinct nature of the hydrogels, arising from the different cross-linking mechanisms, can be described with the fitting model. For the HeLa cells, the mitotic cells have a higher apparent elasticity and a lower apparent viscosity, implying a stiffer actin cortex and a diluted cytoplasm protein concentration, when compared with interphase cells. The chapter concludes with a discussion on the method in Sec. 4.5.

The findings in this chapter demonstrate that the proposed model can reliably extract viscoelastic properties from conventional force-indentation curves. Moreover, the model is able to assess the contribution of the different elastic and viscous elements, and thus allows a direct comparison between the viscoelastic nature of different materials.

4.2 Extension of the phase field model for FSI

The numerical method is based on the phase field model of contact and fluid-structure interaction problems presented in Chapter 3 and published by the author in [7]. This previous work describes an efficient method to simulate the interaction between a fluid and a (visco-)elastic phase. A monolithic Navier-Stokes equation was solved for the velocity field in both, the fluid and the elastic domain. Viscous and elastic forces were restricted to the respective domains via multiplication with characteristic functions. The elastic stress was obtained by an additional Oldroyd-B-like equation which was coupled to the Navier-Stokes equation.

4.2.1 Simulated scenario

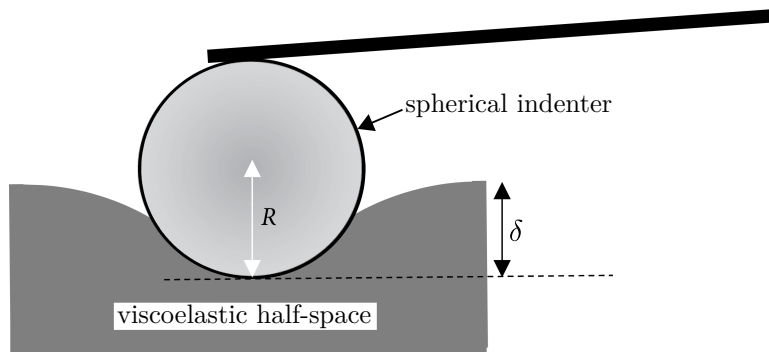


Figure 4.1: Simplified scheme of a spherical indenter moved into a deformable material according to AFM. R and δ denote indenter radius and indentation depth, respectively. Adapted from [78].

This chapter adopts the last-mentioned fundamental features and extends the model in order to simulate a three-phase scenario, including the interaction between a viscoelastic phase, a purely viscous phase and a rigid body. In particular, a numerical model is developed here to simulate the process of indenting a viscoelastic half-space immersed in a liquid medium with a rigid spherical indenter, see Fig. 4.1 for an illustration. The thickness of the indented viscoelastic material is chosen sufficiently

large (relative to the indenter radius) and bottom boundary effects are negligible. Based on the approach in Chapter 3, the surface of the viscoelastic material is represented by a phase field ϕ . Generally, in phase field models the surface is not described as sharp, but instead as a diffusive region with a finite thickness (here $\epsilon = 25$ nm). The presence of this diffuse transition region mimics a coarse-grained description of the irregularity of cell surfaces and leads to a numerically stable contact algorithm.

In the numerical simulation, the rigid indenter is moved with a prescribed velocity through the liquid medium towards the viscoelastic material, while the necessary force is constantly computed. This is detailed in Sec. 4.2.2. Inertial forces are neglected in the present scenario. The viscosity of the liquid medium is set to the value of water (here: 0.001 Pa·s), which gives a negligible force contribution from liquid drag: According to Stokes law the drag force is $\approx 2.4 \cdot 10^{-4}$ nN for a spherical indenter of radius $R = 2.5$ μm at a typical velocity of 5 $\mu\text{m}/\text{s}$, which is four orders of magnitude smaller than the typically measured material resistance. Once the indenter comes into contact with the viscoelastic body, the material is deformed and the force starts to increase as viscous and elastic forces counteract the deformation. Once a maximum indentation is reached, the indenter is immediately pulled out of the material in opposite direction.

Note that the surface tension between liquid and substrate phase is omitted in this chapter.

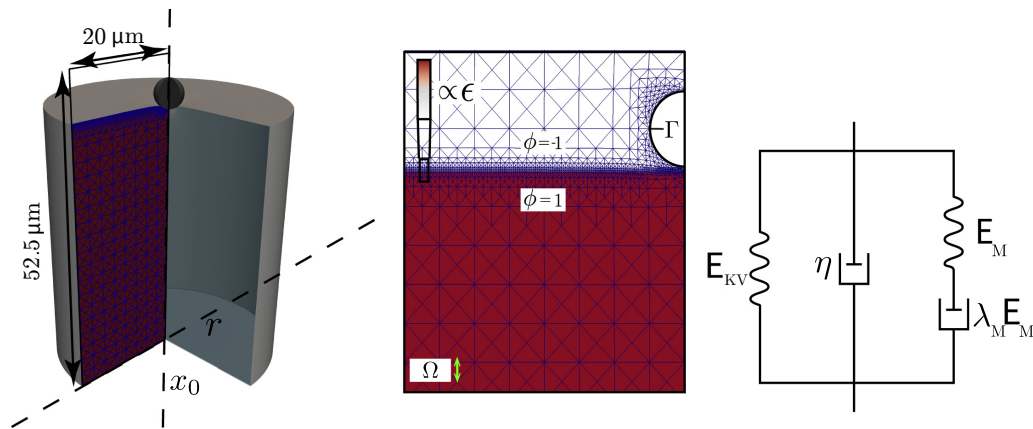


Figure 4.2: Numerical setup for simulating the indentation of viscoelastic material. **Left:** Illustration of the 3D scenario with axisymmetry, and the respective dimensions. The axis of rotation is denoted by x_0 , the radial axis by r . **Middle:** Grid representation of a two-dimensional cross section of the domain (Ω). The color code indicates the phase field ϕ . The red part with $\phi = 1$ represents the viscoelastic material. The white part with $\phi = -1$ represents the liquid medium. Γ denotes the boundary of the indenter, represented by a moving finite element grid. The right boundary of Ω is the axis of rotation. **Right:** Schematic representation of the used neo-Hookean Kelvin-Voigt-Maxwell model. Springs correspond to elastic components and dashpots to viscous components. Adapted from [9].

4.2.2 Mathematical model

As introduced in Sec. 3.5, the considered setup is axisymmetric, thus a 3D scenario can be simulated on a 2D grid (see left and middle part of Fig. 4.2). The two-dimensional computational domain is denoted by $\Omega \subset \mathbb{R}^2$ in this chapter. The model comes with a full Eulerian description of the (common) velocity field $\mathbf{v} : \Omega \rightarrow \mathbb{R}^2$ in the whole domain. Let $\mathbf{v} := (v_0, v_r)$ denote the axial and the radial component, referring to the axis of symmetry. Furthermore, let (x_0, r) denote the axial and the radial component of the position of grid points, where $x_0 = 0$ at the bottom boundary (i.e. at the bottom of the substrate). The boundary conditions $v_r = 0$ on the axis of symmetry ($r = 0$) and $v_0 = 0$ at the bottom boundary apply here.

Indenter dynamics

A crucial modification with respect to the setup in Chapter 3 is the inclusion of the rigid indenter itself. Since it is not necessary to solve any hydrodynamics inside the indenter, the corresponding phase is simply represented by a spherical hole in the computational domain Ω (see middle part of Fig. 4.2). On the indenter boundary $\Gamma \subset \partial\Omega$ it applies $v_0 = v_I$ and $v_r = 0$, where v_I is the prescribed (constant) indenter velocity. The motion is realized by a moving finite element grid with velocity $v_{\text{Grid}} : \Omega \rightarrow \mathbb{R}$ which describes the movement of grid points in axial direction. Note that the grid points do not change their radial position in the simulations. Here, a concertina-like movement is chosen, i.e. $v_{\text{Grid}} = v_I \cdot \min(1, x_0/x_I)$, where x_I denotes the axial position of the advancing (bottom) point of the indenter.

As motivated in Sec. 2.4, an ALE approach is used to account for the moving grid. This amounts to replacing material derivatives ∂^\bullet by $d_t + (\mathbf{v} - (v_{\text{Grid}}, 0)^T) \cdot \nabla$, where d_t is the time derivative along a moving grid point.

The indenter boundary experiences a **force** which is calculated by

$$(F_{x_0}, F_r)^T = 2\pi \int_{\Gamma} \mathbb{S} \cdot \mathbf{n}_{\Gamma} \, d\Gamma,$$

where the absolute value of the axial component F_{x_0} yields the viscoelastic response of the material and will be compared to the force F from the (mechanical) models later in this chapter. The radial component F_r is neglected, as the indenter only moves in axial direction. Furthermore, $\mathbb{S} = -p\mathbb{I} + \eta(\phi)(\nabla\mathbf{v} + \nabla\mathbf{v}^T)$ is the stress tensor, \mathbf{n}_{Γ} is the normal on Γ pointing outside Ω , p the pressure and η the (phase-dependent) viscosity. Note that according to Sec. 4.2.1, the viscosity is set to the value of water in the liquid medium throughout this chapter, while it will be varied in the viscoelastic half-space. The interpolations of η and further phase-dependent parameters are described in Sec. 3.3.

It can be summarized that the rigid indenter as a third phase in this model extension is simply modeled

as a semicircular part $\Gamma \subset \partial\Omega$ of the domain boundary, interacting with the other phases by means of a velocity boundary condition and a defined grid motion. The force F_{x_0} is calculated at the end of each simulation time step from the current values for \mathbf{v} and p . Further note that in this work adhesion between the indenter and the elastic substrate is avoided by setting a phase field boundary condition (here $\phi = -1$ on Γ).

Strain evolution

In Chapter 3, the structure could either be modeled as purely elastic, or as a Kelvin-Voigt or Maxwell material. The choice of the material was made on the basis of certain model parameters (see Table 3.1).

To account for the more complex rheology of many synthetic materials and biological cells, a combined Kelvin-Voigt-Maxwell model (KVM) is used here. Such a model can be represented by choosing a specific combination of springs and dashpots (see Fig. 4.2 Right). The involved four material parameters are (E_{KV}) elastic Young's modulus, (η) viscosity, (E_M) an additional Young's modulus which relaxes over time and (λ_M) viscoelastic relaxation time of the Maxwell component. According to Chapter 3, both elastic components are modeled by a hyperelastic neo-Hookean material law. The Kelvin-Voigt and Maxwell stresses contribute to the total stress in parallel. To extend the phase field FSI model in this respect, two Oldroyd-B-like equations are solved and the model parameters are set once according to Kelvin-Voigt and once according to Maxwell. This results in two different quantities that add up to the total elastic stress. In particular, the system now includes two strain tensors \mathbb{B}_{KV} , \mathbb{B}_M with the corresponding elastic stresses $\frac{1}{3}E_{KV}(\phi)(\mathbb{B}_{KV} - \mathbb{I})$ and $\frac{1}{3}E_M(\phi)(\mathbb{B}_M - \mathbb{I})$ in order to differentiate between Kelvin-Voigt and Maxwell elasticity. Note here that the incompressibility assumption is adopted from Chapter 3 and that the elastic parameters are scalar fields that depend on the phase field ϕ . In the ambient fluid $E_{KV} = E_M = 0$ applies. The strain tensors are calculated by their evolution equations

$$\lambda_i(\phi) (\partial^\bullet \mathbb{B}_i - \nabla \mathbf{v}^T \cdot \mathbb{B}_i - \mathbb{B}_i \cdot \nabla \mathbf{v}) + \alpha_i(\phi) (\mathbb{B}_i - \mathbb{I}) = 0 \quad \text{for } i \in \{KV, M\}.$$

The phase-dependent interpolations from Sec. 3.3 can now be used for λ_i and α_i . Following the notation there, the parameter choice this time is $\alpha_{KV,1} = 0$, $\alpha_{M,1} = 1$, $\lambda_{KV,1} = 1$ second and $\lambda_{M,1} = \lambda_M$ seconds, where the latter value is identical to the Maxwell relaxation time introduced in this chapter (cf. Fig. 4.2 Right). In the ambient fluid, $\alpha_{i,-1} = 1$ and $\lambda_{i,-1} = 0$ seconds applies for $i \in \{KV, M\}$. For further information about these parameters, see Table 3.1.

Finally, the remaining parameters of the model are the constant mobility $m = 1\text{e-}11\text{ m}^3\text{s/kg}$, the interface width $\epsilon = 2.5\text{e-}8\text{ m}$, a fixed grid size of $h = 2.5\text{e-}6\text{ m}$ away from the interface and $h = 7.8125\text{e-}8\text{ m}$ at the interface. The time step size is $\tau = 2.5\text{e-}5\text{ s}$. The numerical simulation

method was implemented in the finite element toolbox AMDiS [59, 60]. For further details and instructions to reproduce the simulations in this chapter, see [9].

4.3 Numerical results

4.3.1 Model validation using Hertzian theory

In the following, the simulated force-indentation curves are considered and a comparison is made with the available Hertzian contact mechanics theory.

Purely hyperelastic material

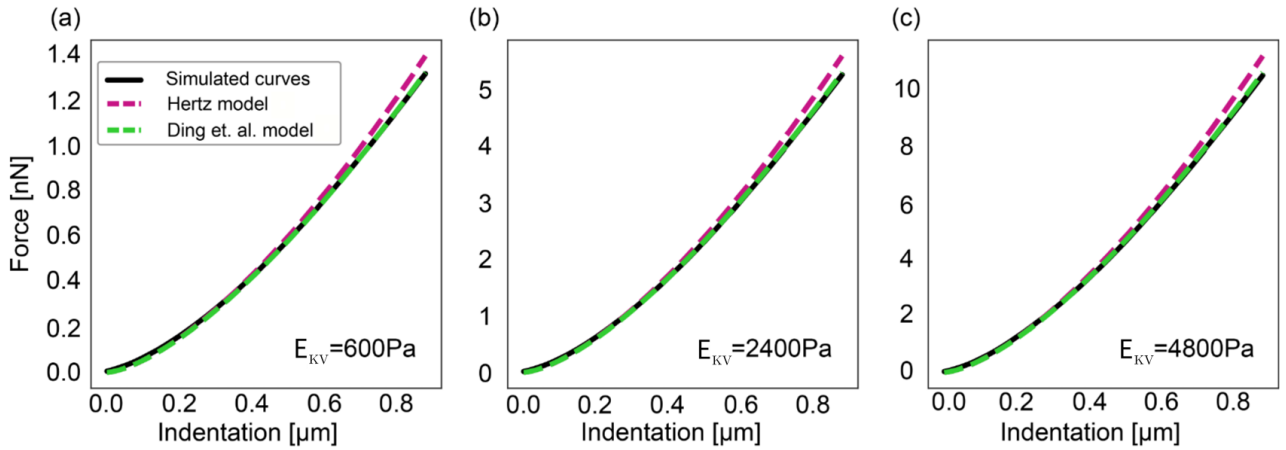


Figure 4.3: Validation of the numerical model with purely elastic material having different elasticity values: (a) 600 Pa, (b) 2400 Pa and (c) 4800 Pa. The black continuous line depicts the force-indentation curve retrieved from the indentation simulation. The pink and green dashed lines correspond to the Hertz and Ding et al. models described in Eqs. (4.1) and (4.2). Adapted from [9].

To validate the numerical model, a purely hyperelastic material ($\eta = E_M = \lambda_M = 0$) is first simulated, consisting of a single spring (cf. Fig. 4.2 Right). Due to the lack of viscous components, no hysteresis is to be expected in the resulting force-indentation curves. Therefore, the focus is on the approach part of the curves while comparing them with both the Hertz model [68] and the model of Ding et al. [79]. The force-indentation relations of the latter mentioned models read

$$F = \frac{4}{3} \frac{E_{KV}}{1 - \nu^2} \sqrt{R\delta^3} \quad (\text{Hertz model [68]}), \quad (4.1)$$

$$F = \frac{4}{3} \frac{E_{KV}}{1 - \nu^2} \sqrt{R\delta^3} \left(1 - 0.15 \frac{\delta}{R} \right) \quad (\text{Ding et al. [79]}), \quad (4.2)$$

where F and δ are the force and the indentation depth, respectively, ν and R are the Poisson's ratio of the material and radius of the spherical indenter, respectively. Since incompressible (visco-)elastic materials are considered here, $\nu = 0.5$ throughout this chapter. In the numerical tests, $R = 2.5 \mu\text{m}$ is

chosen and the maximum indentation depth is $0.88\ \mu\text{m}$. Note that the indenter velocity ($v_I = 5\ \mu\text{m/s}$ in the simulations) does not affect the force-indentation relation according to models (4.1) and (4.2).

While the Hertz model is valid only for very small (linearly) elastic deformations, the model from Ding et al. is applicable for a larger range of deformations as it has been derived numerically using a hyperelastic material law. Both models fitted very well to the simulated data in the range of small indentations and, as expected, the Ding et al. model fitted the data better in the range of large indentations, see Fig. 4.3.

The effect of viscoelasticity on force-indentation curves

Indenting a biological material with AFM often exhibits a hysteresis between approach and retraction curves, which implies the presence of viscoelastic behavior. To account for viscoelasticity, the simplest two viscoelastic models that can be used are a Kelvin-Voigt solid (spring and dashpot connected in parallel) and a Maxwell liquid (spring and dashpot connected in series). It is important to note that when referring, throughout the chapter, to the mechanical model name such as Kelvin-Voigt or Maxwell model, the intention is the contact model based on that specific mechanical model.

This time, in the simulations, the indenter is moved at the constant velocity $v_I = 5\ \mu\text{m/s}$ up to the maximum indentation depth, followed by an instantaneous retraction at velocity $-v_I$. Increasing the viscosity of the Kelvin-Voigt material led to a higher deviation from the Hertzian curve Eq. (4.2), see Fig. 4.4(a). Similarly, the indentation curve deviated more from the Hertzian curve with decreasing the relaxation time λ_M of the Maxwell material, see Fig. 4.4(b).

Comparing both models, the hysteresis between the approach and retraction curves appeared distinctively different. While the Kelvin-Voigt model shows a hysteresis where the difference between the curves increases with indentation depth, the Maxwell model shows a hysteresis where the difference between the curves is the smallest at the largest indentation depth. In addition, a jump, that is dependent on the viscosity value, can be observed between the approach and retraction curves of the Kelvin-Voigt model. These distinctive features combined together are present when visually inspecting an AFM force-indentation curve (see Fig. 4.4(d) for an exemplary experimental curve).

The Kelvin-Voigt model describes successfully the creep compliance of the material and its ability to regain the original shape after the load is removed. However, it fails in describing the relaxation of a viscoelastic material. On the other hand, the Maxwell model describes very well the stress relaxation but fails in describing the creep of the material [80].

Taken together, to capture both the relaxation and the ability of the indented material to regain its original shape as observed in AFM indentation experiments on soft materials, Kelvin-Voigt (spring E_{KV} , dashpot η) and Maxwell (spring E_M , dashpot $\lambda_M E_M$) materials are connected in parallel (KVM model) to represent viscoelasticity in the half-space (Fig. 4.4(c)). The force-indentation curves of the KVM model combine the characteristics of the two simple Kelvin-Voigt and Maxwell models. This is

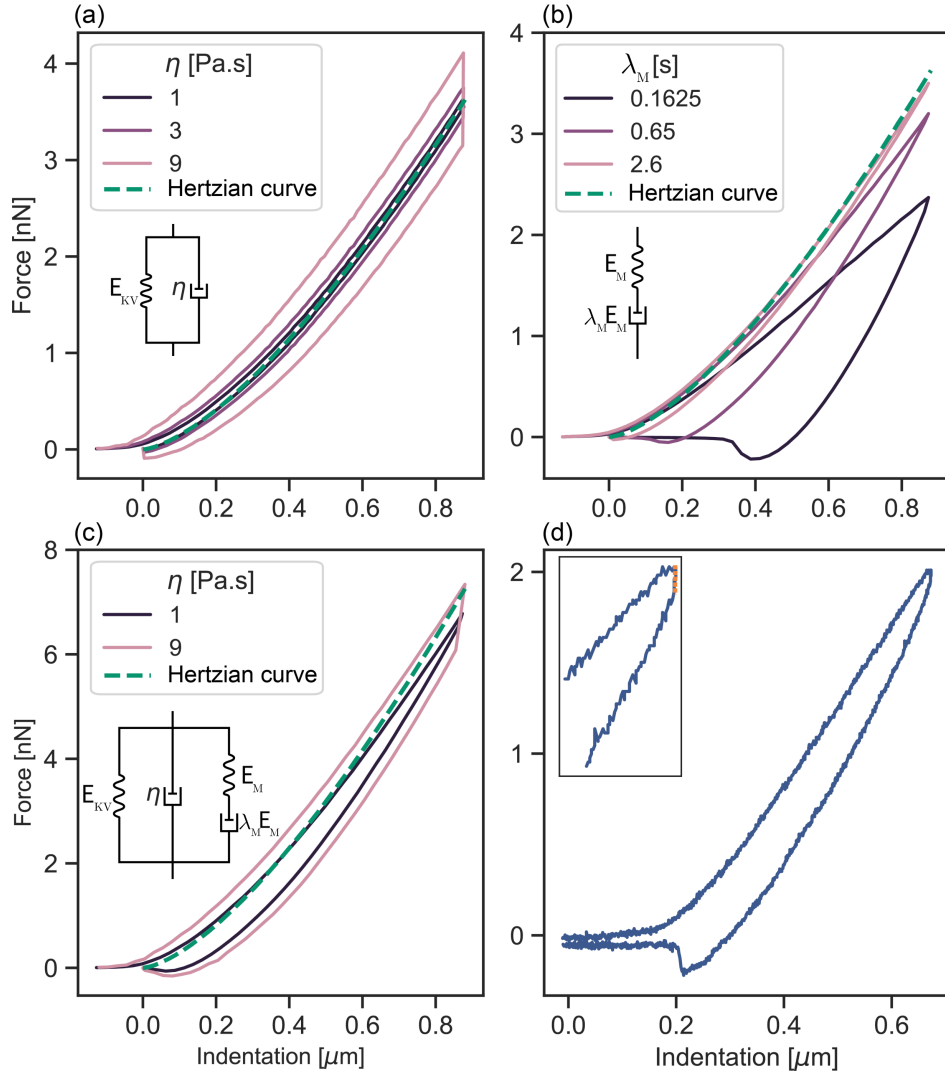


Figure 4.4: Force-indentation curves of different viscoelastic materials. For (a)-(c), solid lines represent simulation results and green dashed lines show the corresponding (modified) Hertz model curves Eq. (4.2). (a) Kelvin-Voigt material simulated with varying viscosity η values and $E_{KV} = 1650$ Pa. (b) Maxwell material simulated with varying relaxation time λ_M values and $E_M = 1650$ Pa. (c) Kelvin-Voigt-Maxwell (KVM) simulated with varying viscosity η values, $\lambda_M = 0.65$ s, $E_{KV} = 1650$ Pa and $E_M = 1650$ Pa. For the green dashed line (Hertz model), the Young's modulus is set to $E_{KV} = 3300$ Pa. (d) Representative AFM force-indentation curve of a cell (see [9] for resources). The orange dashed line in the inset highlights the force jump at the end of the approach and beginning of the retraction curves. This jump resembles the jump seen in (a) and (c) for the Kelvin-Voigt and KVM models. For all the subfigures, the radius of the indenter is $R = 2.5$ μm and the velocity is $v_I = 5$ $\mu\text{m/s}$. Adapted from [9].

specifically observed in the hysteresis as well as the force jump (immediate loss of force) between the approach and retraction curves, which resemble very well the representative force-indentation curve of a cell measured by AFM (Fig. 4.4(d)). Also note that the model captures two characteristics of experimental data which were not reproduced with any other numerical method yet: (i) the onset of a

force response already slightly before contact and (ii) the negative force as the indenter detaches from the sample. These contributions stem from the diffuse description of the substrate surface and the inclusion of the liquid medium which provides a force before contact (to drain fluid out of the contact region) and a corresponding negative (sinking) force upon detachment.

4.3.2 Explicit relation of force and indentation

This subsection first proposes an explicit relation between force and indentation. Furthermore, a parameter range is established for which the simulated force-indentation curves fit the proposed model. Finally, a set of simulation results is presented to demonstrate the validity of the model together with its ability to describe various viscoelastic material models. For detailed information about the fitting algorithm used in the following, see [9].

AFM force-indentation curves are typically evaluated by fitting to analytical functions relating the force to the indentation as shown in Eq. (4.1) and Eq. (4.2). In the Ding et al. model, the effects of larger indentation were accounted for by multiplying the Hertz model with an additional term, while maintaining the explicit relation between force and indentation. A similar procedure is now followed here and the model of Ding et al. is supplemented with terms that take into account the viscoelastic behavior of the KVM material.

The total force acting on the KVM material is equal to the sum of the forces exerted by each of the elements connected in parallel, cf. Fig. 4.4(c): $F_{\text{total}} = F_0 + F_1 + F_2$, where F_0 is the force exerted by the spring E_{KV} , F_1 is the force exerted by the Maxwell elements E_M and $\lambda_M E_M$ and finally F_2 is the force exerted by the dashpot η . For elastic solids, the force exerted by the spring E_{KV} is linearly related to the value of the elasticity E_{KV} . In fact, this can be assumed to be the force derived for the Hertz model or any other model that corrects for larger indentations, such as the Ding et al. model. This force is denoted by F_{elastic} in the following. Similarly, the force exerted by the Maxwell element is linearly related to the value of the spring E_M , however, combined with an exponential decay due to the dissipation in the dashpot $\lambda_M E_M$. Finally, the force exerted by the dashpot η can be described as a drag force acting on the segment of the indenter that is in contact with the material. Hence, the force-indentation relation $F(\delta)$ can be described as follows:

$$F(\delta) = F_{\text{elastic}}(E_{KV}, \delta) + F_{\text{elastic}}(E_M, \delta) \cdot \exp\left(\frac{-\Lambda_1 \delta}{v_I \lambda_M}\right) + \Lambda_2 \delta^{\Lambda_3} R^{\Lambda_4} \eta v_I, \quad (4.3)$$

where

$$F_{\text{elastic}}(E, \delta) = \frac{4}{3} \frac{E}{1 - \nu^2} \sqrt{R \delta^3} \left(1 - 0.15 \frac{\delta}{R}\right) \quad (4.4)$$

and E_{KV} , E_M , λ_M and η correspond to the KVM model elements shown in Fig. 4.4(c). v_I is the velocity of the indenter, cf. Sec. 4.2.2.

The functional form Eq. (4.3) contains four fitting parameters, $(\Lambda_1, \dots, \Lambda_4)$, which are determined from matching this function to simulated force-indentation curves. Note that the condition $\Lambda_3 + \Lambda_4 = 1$ should hold to maintain the correct dimension. Using simulations for a wide range of parameter values led to $\Lambda_1 = 0.365$, $\Lambda_2 = 7.25$, $\Lambda_3 = \Lambda_4 = \frac{1}{2}$.

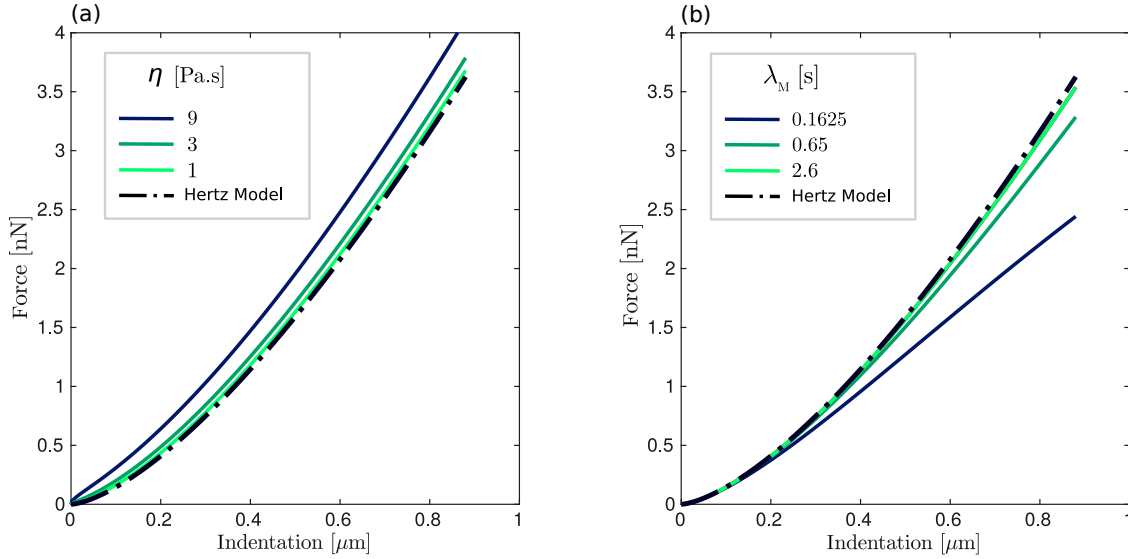


Figure 4.5: Force evolution during the indentation, using parts of the explicit relation Eq. 4.3. (a) Force evolution of $F = F_{\text{elastic}}(E_{KV}, \delta) + \Lambda_2 \delta^{\Lambda_3} R^{\Lambda_4} \eta v_I$, where $E_{KV} = 1650$ Pa and the viscosity η was varied. (b) Force evolution of $F = F_{\text{elastic}}(E_M, \delta) \cdot \exp((-\Lambda_1 \delta) / (v_I \lambda_M))$, where $E_M = 1650$ Pa and the relaxation time λ_M was varied. The dashed black lines depict the force-indentation relation of the Ding et al. model Eq. (4.2) with a Young’s modulus of 1650 Pa. For both subfigures, the radius of the indenter is $R = 2.5$ μm , the Poisson’s ratio $\nu = 0.5$ and the velocity $v_I = 5$ $\mu\text{m/s}$.

Force evolution

To illustrate the influence of the terms in Eq. (4.3) on the evolution of the force versus the indentation, Fig. 4.5 shows in (a) the force evolution of $F = F_{\text{elastic}}(E_{KV}, \delta) + \Lambda_2 \delta^{\Lambda_3} R^{\Lambda_4} \eta v_I$ and in (b) the force evolution of $F = F_{\text{elastic}}(E_M, \delta) \cdot \exp(\frac{-\Lambda_1 \delta}{v_I \lambda_M})$. Varying the viscosity η or the relaxation time λ_M exhibits the expected approximation to the Hertz curve, similar to the behavior of the curves from simulations of Kelvin-Voigt and Maxwell materials, cf. Fig. 4.4(a) and (b).

It is important to note that the fitting model is valid for a specific range of ratios between the Maxwell relaxation time λ_M and the indentation time t_{ind} , see Fig. 4.6. The viscosity η is neglected in this validity study. If the relaxation time λ_M is significantly larger than the time t_{ind} in which the material was probed, the effects of E_{KV} and E_M become redundant and cannot be distinguished anymore. In this case the material will be depicted as dominantly elastic with an elastic modulus of $E_{KV} + E_M$. This is shown by the curve “ $\lambda_M \rightarrow \text{inf}$ ” (dashed black) in Fig. 4.6, which simply represents the relation

$F(\delta) = F_{\text{elastic}}(E_{KV} + E_M, \delta)$ with $E_{KV} = E_M = 900$ Pa.

Similarly, if λ_M is significantly smaller than t_{ind} , the material will relax quickly at the onset of indentation and will be depicted as a pure Kelvin-Voigt model, making E_M arbitrary. This is represented by the curve “ $E_M = 0$ ” (dashed red) in Fig. 4.6, which corresponds to the relation $F(\delta) = F_{\text{elastic}}(E_{KV}, \delta)$ with $E_{KV} = 900$ Pa. The limiting cases $\lambda_M \rightarrow 0$ and $\lambda_M \rightarrow \infty$ thus enclose the range of possible force-indentation curves, with the other parameters remaining unchanged. To obtain meaningful results, the fitting range of λ_M is bound in the algorithm to be dependent on t_{ind} (here: $t_{\text{ind}} = 0.176$ s), where the upper and lower limits were set to $10 t_{\text{ind}}$ and $t_{\text{ind}}/5$, respectively.

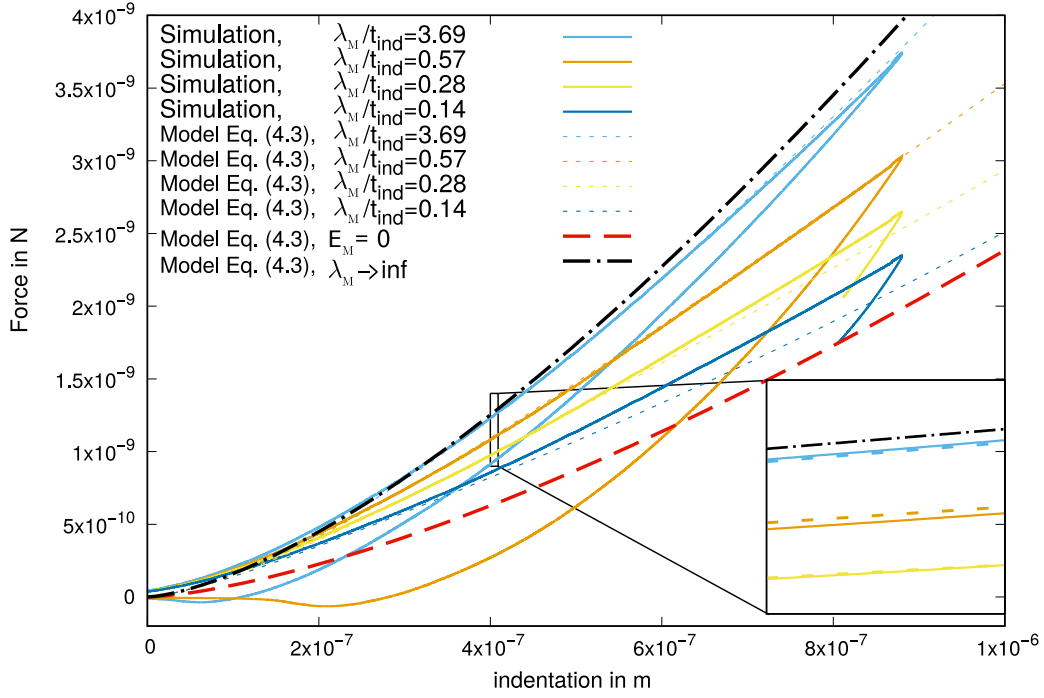


Figure 4.6: Validity study of the fitting model Eq. (4.3) in different parameter ranges. Simulation results (solid lines) are shown with varying values for the Maxwell relaxation time λ_M . The indentation time is set to $t_{\text{ind}} = 0.176$ s. The ratio of the Maxwell relaxation and the indentation time is shown in the figure. The remaining parameters used for the simulations are: $v_I = 5 \mu\text{m/s}$, $E_{KV} = E_M = 900$ Pa, $R = 2.5 \mu\text{m}$. The viscosity η is neglected here. Adapted from [9].

Therefore, in order to give a clear view on the elasticity and the dissipation in different time scales, it is most advantageous to evaluate the total unrelaxed elasticity $E_u = E_{KV} + E_M$ contained in the material and the apparent elasticity measured in the time scale of the indentation measurement $E_{\text{app}} = E_{KV} + E_M \exp(-\Lambda_1 \delta / v_I \lambda_M)$ as well as the apparent viscosity η . These moduli lead to a more robust and stable evaluation of the model parameters even at the extreme cases of the ratio $\lambda_M / t_{\text{ind}}$.

Validation by means of different viscoelastic material models

To demonstrate the ability of the explicit force-indentation relation Eq. (4.3) to fit to materials with different mechanical characteristics, indentation is simulated in Kelvin-Voigt, standard linear liquid (SLL; Maxwell element and a viscous dashpot in parallel) and Kelvin-Voigt-Maxwell model half-spaces. In this way, the agreement of the fitted values of the elastic and viscous components with the values chosen in the simulations can be evaluated. Note that the model parameters of the strain evolution equations must be chosen accordingly to distinguish between the material models, as described in Sec. 4.2.2. As indicated in Fig. 4.7, the fitted values are quite close to the simulated values, and the fitting model can distinguish the different mechanical models used in the simulations. In the following section, the fitting model is applied to experimental AFM data from different materials.

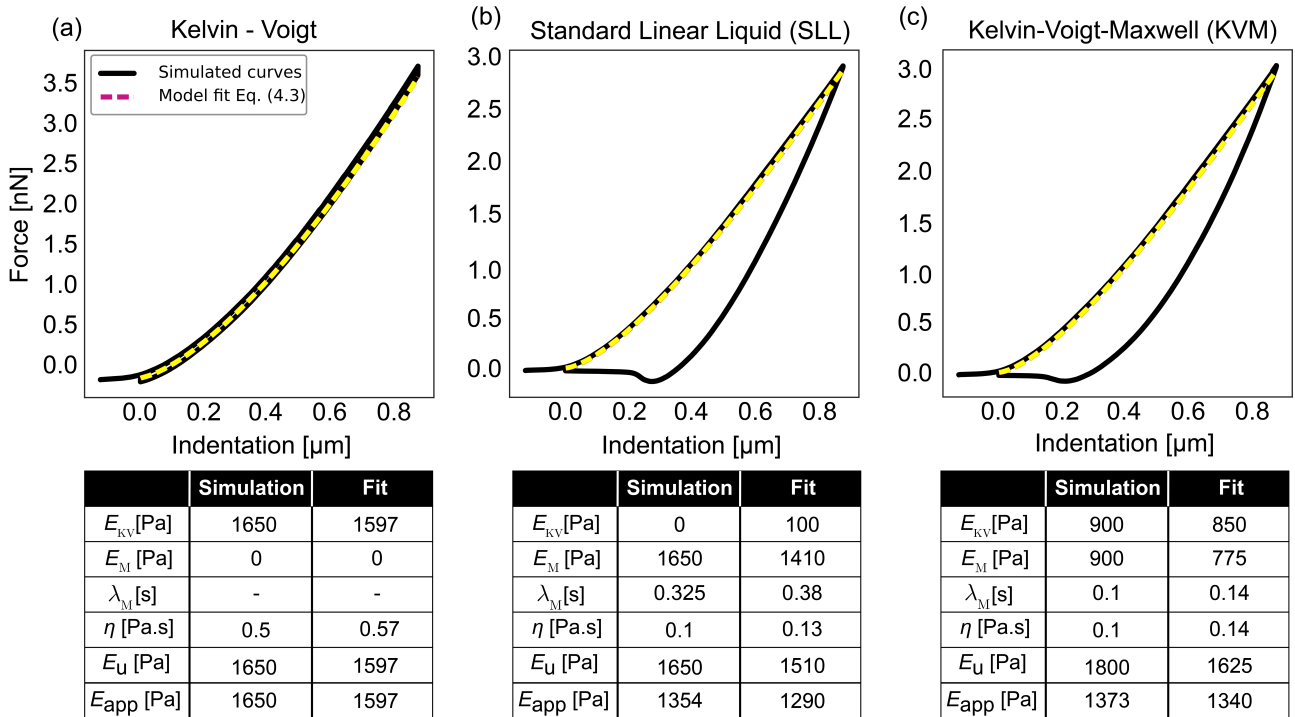


Figure 4.7: Validation of the fitting model Eq. (4.3) using simulated force-indentation curves with different material properties. (a) Kelvin-Voigt, (b) standard linear liquid and (d) Kelvin-Voigt-Maxwell. The solid black lines depict the force-indentation curves retrieved from the simulations. The yellow dashed lines depict the model fits. The tables below each curve show the simulated and fitted values of the mechanical parameters. The remaining parameters used for the simulations are: $v_I = 5 \mu\text{m/s}$, $R = 2.5 \mu\text{m}$, $t_{ind} = 0.176 \text{ s}$. Adapted from [9].

4.4 Probing mechanical properties of various materials

4.4.1 Viscoelastic properties of hydrogels

To investigate the fitting model performance on measured AFM curves, the mechanical properties of two hydrogels were evaluated: polyacrylamide (PAAm) and low-gelling-point agarose hydrogels. The PAAm hydrogel is chemically crosslinked using ammonium persulfate while the agarose hydrogel is physically crosslinked by reducing the temperature of the solution. This difference in the crosslinking mechanisms leads to an inherent difference in their mechanical properties, where the PAAm hydrogel can be described as an elastic network swollen with a liquid solvent [81] and the agarose hydrogel is described as a viscoelastic network. The time dependence of the PAAm hydrogel arises from the necessity of the solvent to move through the elastic polymer network during deformation, while in the agarose hydrogel it comes from the time-dependent nature of the crosslinks between the polymers.

AFM measurements were performed to generate force-indentation curves of the hydrogels at different indenter velocities 5, 10 and 15 $\mu\text{m/s}$, followed by an evaluation of their mechanical properties by fitting Eq. (4.3) to the curves. Representative force-indentation curves are shown in Fig. 4.8 at the end of this section. Moreover, Fig. 4.9(a) and (c) show the two moduli E_{KV} and E_M for the PAAm and agarose hydrogels, respectively. The apparent viscosity η of the two hydrogels at different velocities is shown in Fig. 4.9(b) for PAAm and Fig. 4.9(d) for agarose.

The PAAm hydrogels showed similar values of the Kelvin-Voigt elastic modulus E_{KV} at all indentation velocities (2.45 ± 0.04 , 2.24 ± 0.01 and 2.48 ± 0.11 kPa, mean \pm standard error of the mean, for velocities of 5, 10 and 15 $\mu\text{m/s}$, respectively), while the Maxwell elastic modulus E_M was considerably lower for PAAm hydrogels. The agarose hydrogels had higher values of E_M compared to E_{KV} , pointing towards a viscoelastic network that relaxes over time. The apparent viscosity values η for both hydrogels decreased with higher indentation velocities (for PAAm, $\eta = 1.3 \pm 0.07$, 1.02 ± 0.03 , 0.95 ± 0.02 Pa·s, and for agarose, $\eta = 0.45 \pm 0.02$, 0.21 ± 0.01 , 0.17 ± 0.01 Pa·s for velocities of 5, 10 and 15 $\mu\text{m/s}$, respectively).

The unrelaxed modulus $E_u = E_{KV} + E_M$ and the apparent modulus $E_{\text{app}} = E_{KV} + E_M \exp\left(\frac{-\Lambda_1 \delta}{v_I \lambda_M}\right)$ for PAAm and agarose hydrogels at different indentation velocities are shown in Fig. 4.10(a) and (b), respectively. As expected, the PAAm hydrogels had similar values for unrelaxed and apparent moduli ($E_u, E_{\text{app}} = 2.45 \pm 0.04$, 2.64 ± 0.05 , 2.7 ± 0.07 kPa for velocities of 5, 10 and 15 $\mu\text{m/s}$, respectively), a behavior indicative of the elastic network. The agarose hydrogels, though, showed lower values of the apparent Young's modulus when compared with the unrelaxed modulus ($E_u = 2.25 \pm 0.07$, 2.15 ± 0.08 , 2.07 ± 0.06 kPa and $E_{\text{app}} = 1.38 \pm 0.06$, 1.33 ± 0.06 , 1.21 ± 0.05 kPa for velocities of 5, 10 and 15 $\mu\text{m/s}$, respectively). This difference in the values of the unrelaxed and the apparent moduli originates from the relaxation of the viscoelastic network during the measurement time. In summary, the ability of the model to describe the mechanical behavior of two different hydrogels was demonstrated here.

4.4.2 Viscoelastic properties of HeLa cells in interphase and mitosis

HeLa cells are a type of cell line originally derived from human cancer cells. They are robust and reproduce very quickly, which makes them a valuable resource for scientific research. For more details on the corresponding AFM measurements and the samples studied here, the reader is referred to [9].

In particular, viscoelastic properties of interphase and mitotic HeLa cells were measured. Representative force-indentation curves are shown in Fig. 4.11. Comparing the Kelvin-Voigt modulus E_{KV} , the interphase cells appeared overall more compliant than the mitotic cells ($E_{KV} = 0.8 \pm 0.06$ kPa for interphase and $E_{KV} = 2.2 \pm 0.3$ kPa for mitotic) as shown in Fig. 4.12(a). Interestingly, the mitotic cells also had a significantly higher value of the Maxwell modulus E_M which relaxes during the indentation measurement time ($E_M = 0.0 \pm 0.0$ kPa for interphase and $E_M = 0.76 \pm 0.17$ kPa for mitotic). The relaxing elastic component could be attributed to the difference in the actin cortex arrangement between spread interphase cells and round mitotic cells. Furthermore, the apparent viscosity η was higher for the interphase cells ($\eta = 2.71 \pm 0.18$ Pa·s for interphase and $\eta = 1.71 \pm 0.06$ Pa·s for mitotic cells).

Owing to the presence of a Maxwell modulus component E_M in the mechanical characterization of the mitotic cells, their apparent Young's Modulus appeared, although not statistically significant, lower when compared with the unrelaxed modulus ($E_u = 3.0 \pm 0.28$ kPa and $E_{app} = 2.7 \pm 0.28$ kPa) as shown in Fig. 4.12(c). The interphase cells had similar values of the unrelaxed ($E_u = 0.8 \pm 0.06$ kPa) and apparent ($E_{app} = 0.8 \pm 0.07$ kPa) moduli. Here it was shown that the viscoelastic properties of mitotic and interphase cell states can now be easily compared via a simple force-indentation measurement.

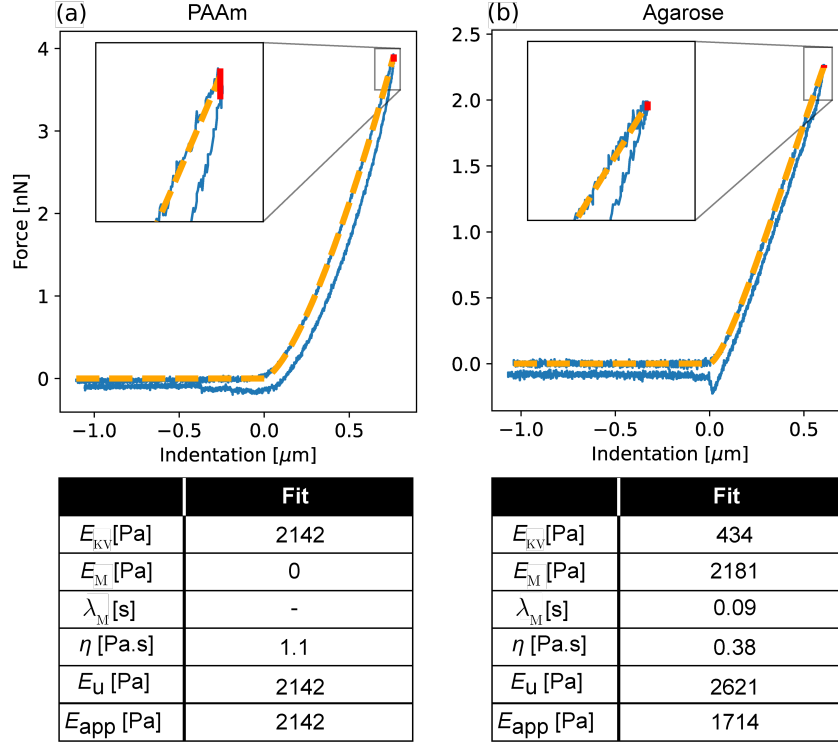


Figure 4.8: Representative force-indentation curves for (a) PAAm and (b) agarose hydrogels, see [9] for resources. The blue line shows the force-indentation curve acquired by AFM, the dashed orange line shows the approach curve using the fitting model in Eq. (4.3). The fitted parameters are shown in the table below each figure. The vertical red line highlights the jump at the end of the approach and the beginning of the retraction curve, regarding the AFM measurements. For these measurements, the radius of the indenter is $R = 2.5 \mu\text{m}$ and the indentation velocity is $v_I = 5 \mu\text{m/s}$. Adapted from [9].

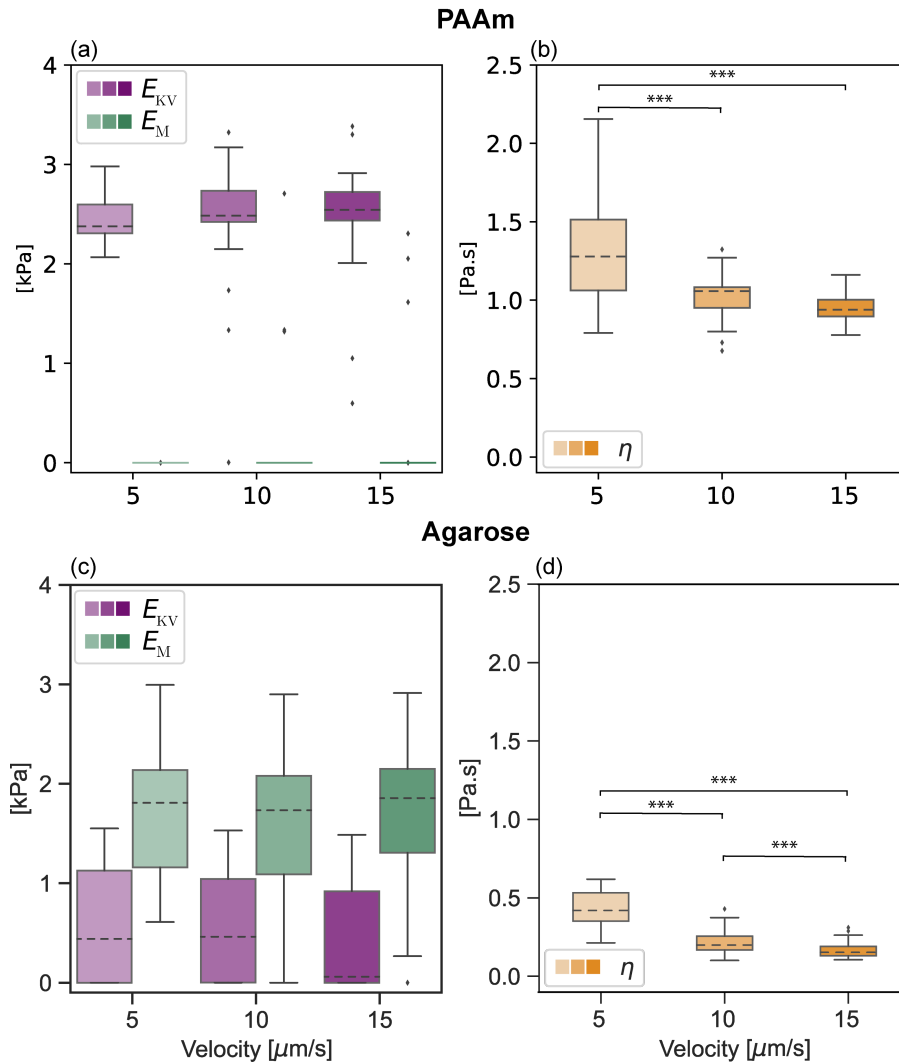


Figure 4.9: Mechanical characterization of polyacrylamide (PAAm) hydrogel ((a) and (b)) and agarose hydrogel ((c) and (d)) indented with a spherical indenter at different velocities using AFM, see [9] for resources. (a) and (c) show the elastic moduli E_{KV} (purple) and E_M (green) for PAAm and agarose hydrogels, respectively. (b) and (d) show the apparent viscosity η (orange) for PAAm and agarose hydrogels, respectively. Data are presented as box-whisker plots (25th, 50th, 75th percentiles, whiskers indicate 10th and 90th percentiles). Results of a statistical test (Kruskal Wallis) are shown. *** denotes p values < 0.001 , pointing to significantly different viscosity values. The number of curves analyzed for every hydrogel at a specific indentation velocity is 27 – 36. Each hydrogel was measured in four different areas. Adapted from [9].

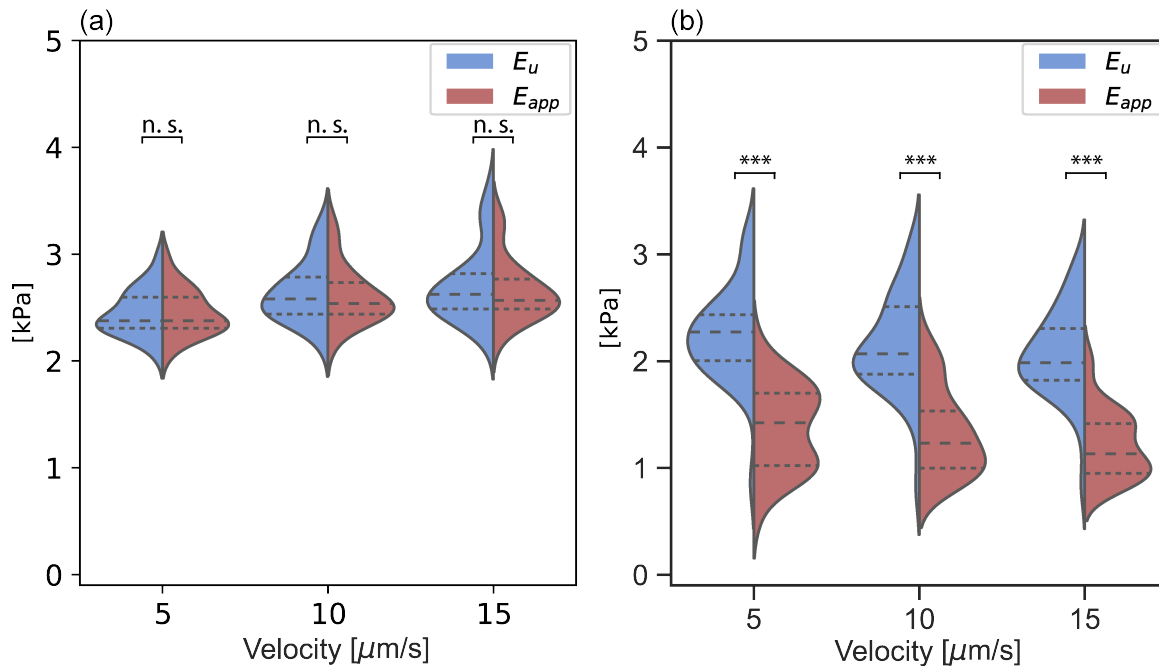


Figure 4.10: Unrelaxed E_u (blue) and apparent E_{app} (red) Young's moduli of PAAm (a) and agarose (b) hydrogels quantified at different indentation velocities (see [9] for resources). Data are presented as violin plots indicating the 25th, 50th and 75th percentiles. Results of a statistical test (Kruskal Wallis) are shown. *** denotes p-values < 0.001 (i.e. significant difference between E_u and E_{app}) and n.s. stands for not significant. Image from [9].

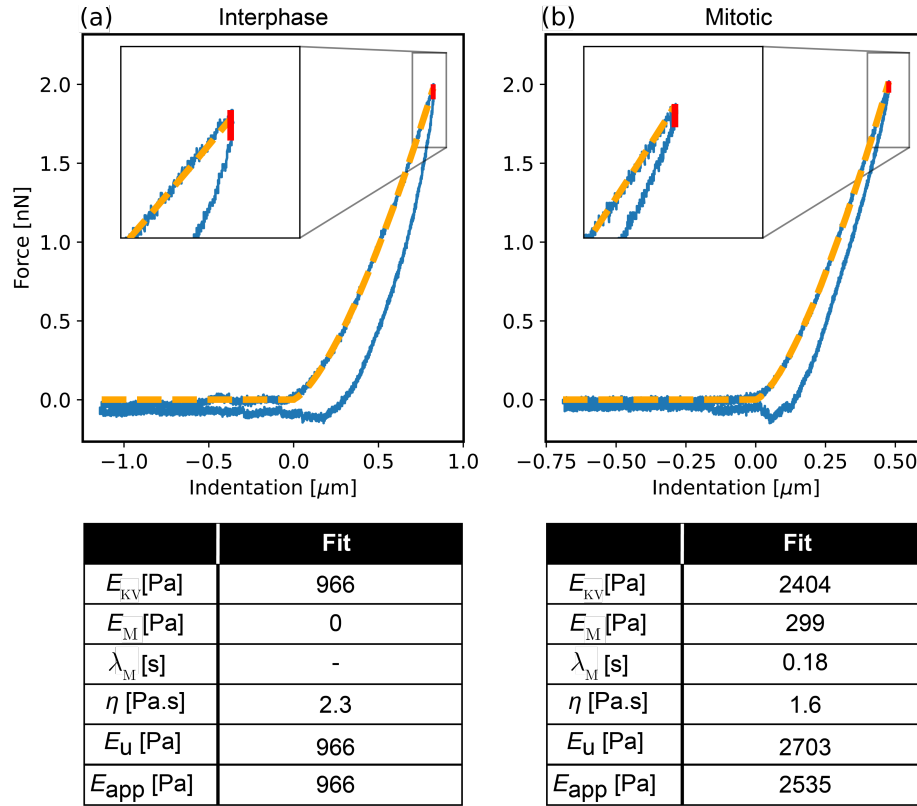


Figure 4.11: Representative force-indentation curves of (a) interphase and (b) mitotic HeLa cells (see [9] for resources). The blue line shows the force-indentation curve acquired by AFM, the dashed orange line shows the approach curve using the fitting model in Eq. (4.3). The fitted parameters are shown in the table below each figure. The vertical red line highlights the jump at the end of the approach and the beginning of the retraction curve, regarding the AFM measurements. For these measurements, the radius of the indenter is $R = 2.5 \mu\text{m}$ and the indentation velocity is $v_I = 2 \mu\text{m/s}$. Adapted from [9].

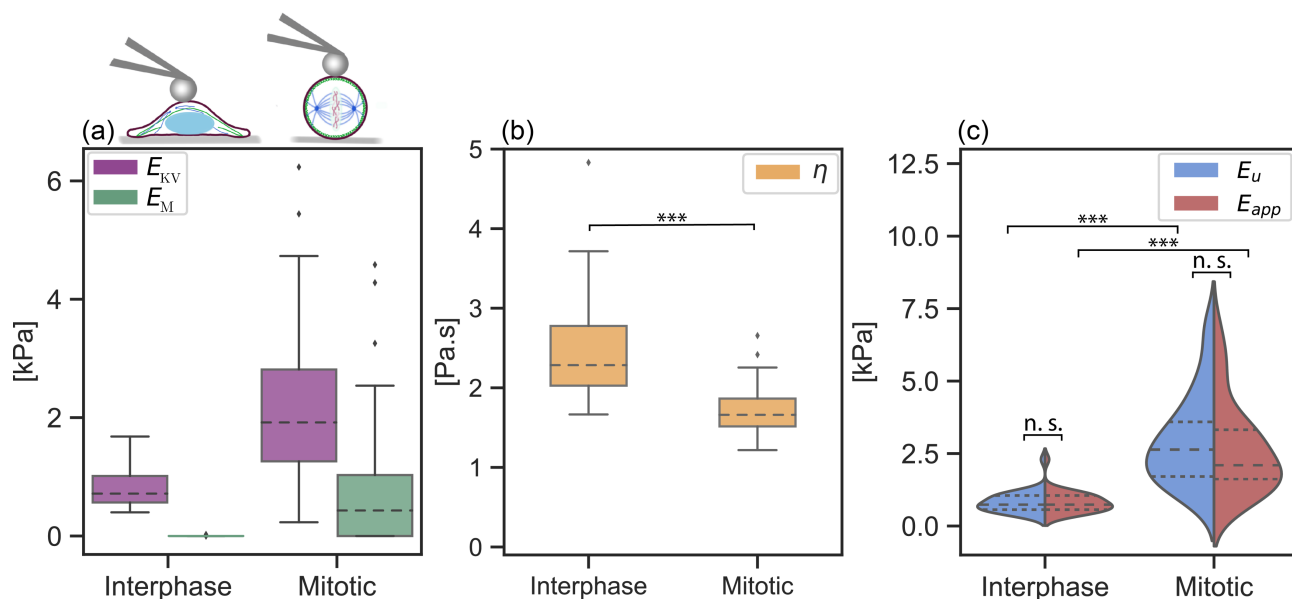


Figure 4.12: Mechanical properties of interphase and mitotic HeLa cells (see [9] for resources). **(a)** The elastic moduli E_{KV} (purple) and E_M (green). **(b)** The apparent viscosity η (yellow). Data in (a) and (b) are presented as box-whisker plots (25th, 50th, 75th percentiles, whiskers indicate 10th and 90th percentiles). **(c)** The unrelaxed E_u (blue) and apparent E_{app} (red) moduli of cells in both cell cycle phases. Data are presented as violin plots indicating the 25th, 50th and 75th percentiles. Results of a statistical test (Kruskal Wallis) are shown. *** denotes p-values < 0.001 , indicating significantly different viscosity values in (b) and elasticity values in (c). In contrast, n.s. denotes non-significant differences between E_u and E_{app} in (c). For every cell cycle phase two independent experiments were performed and a total of 32 cells were measured. Adapted from [9].

4.5 Discussion

In the last few years, AFM became the gold standard method for probing the rheological properties of small-sized soft materials that, otherwise, could not be probed with conventional viscometers and rheometers. To adequately characterize the viscoelastic behavior of the materials with AFM, one should observe the material response in time or frequency domains.

Time-dependent static measurements are usually applied via step-hold experiments, where the force relaxation or the material creep are recorded. An analytical model is then fitted to the recorded force or indentation signals extracting the viscoelastic properties [72, 65, 82]. Alternatively, dynamic measurements can be applied by moving the cantilever in a sinusoidal manner and recording the amplitude and the phase shift of the cantilever deflection. The complex modulus of the material is then evaluated at the different oscillation frequencies of the cantilever [71, 70]. Both methods, step-hold and sinusoidal oscillation, require the user to prepare elaborate acquisition and analysis processes with lengthy measurement times.

Force-indentation measurements, where the cantilever is linearly lowered to indent the sample and then retracted back, are still one of the most used methods for probing soft materials with AFM. A Hertzian model is conventionally used to extract the elastic modulus of the probed sample from the force-indentation curves. The hysteresis present between the approach and retraction curves of the sample confirms that the Hertzian contact mechanics assumption of a purely elastic material is not met. Thus, a few studies have attempted to derive the viscoelastic properties of the materials from the hysteresis between the approach and retraction curves [83, 84, 85]. For example, Rabelo et al. [83] estimated the viscoelastic properties of human kidney epithelial cancer cells from force-indentation curves. The elastic modulus was obtained by fitting the Hertz model, while the apparent viscosity was calculated from the hysteresis between approach and retraction curves of the cantilever. More specifically, the work lost in the approach-retraction cycle was associated with the internal friction forces of the sample. In this work, the calculation of the apparent viscosity required, among other steps, the integration of the approach-retraction curves to calculate the slopes over the indentation range. Nonetheless, this method relies on estimating the slope of noisy data and it assumes an elastic fit for the indentation and retraction curves.

Other recent studies have suggested fitting both the approach and retraction parts of the force curve with a model that accounts for the viscoelastic dissipation [86, 87, 88, 89]. The development of the models relied on the viscoelastic contact mechanics derivation by Lee and Radok [90] and the application of Ting's model [91] for extending the solution to the retraction part of the curve. In each of these studies, a mechanical model, such as a standard linear solid (SLS) or power law rheology, is chosen to describe the material's mechanical nature. Efremov et al. [88] suggested using a SLS model for describing hydrogels and power law rheology for describing cells. The necessity to alternate between models originated from the difference in the behavior of cells and hydrogels in the extreme

cases of $t \rightarrow 0$ and $t \rightarrow \infty$. In these cases, the SLS model describes a purely elastic material with a high elastic modulus E_0 at short times ($t \rightarrow 0$) that relaxes to a lower elastic modulus value E_∞ at longer times ($t \rightarrow \infty$). The power law model, on the other hand, shows a monotonic decrease of the elastic modulus value over time. In such approaches, the user is required to select a model, SLS or power law, even if the mechanical properties of the material have not yet been determined. In addition, the suggested fitting models do not give an explicit relation between the force and indentation signals, and require a rather iterative process of solving integrals numerically.

In this chapter (i.e. in [9]), a new model was developed for fitting AFM force-indentation curves and extracting the viscoelastic behavior of a probed material. It was shown that combining the simplest two viscoelastic mechanical models, Kelvin-Voigt and Maxwell, will account for the hysteresis as well as the regaining of the initial material shape. The underlying numerical method uses fundamental physical laws to predict the force-indentation curve for given viscoelastic parameters. The goal in experimental applications is to directly predict viscoelastic parameters from the measured force-indentation curves. As the numerical model cannot be easily inverted, numerical results were used here for a broad range of parameters to extract the functional dependence by means of a fitting routine. Thus, to extract the viscoelastic properties from AFM force-indentation curves, a fitting model was proposed that describes an explicit relation between the force and the indentation signals in the approach curve. In contrast to common mechanical models typically considered, such as SLS, the Kelvin-Voigt-Maxwell (KVM) model can still describe the viscosity of the materials at very short times. In the force-indentation curves this is translated to the presence of hysteresis between the approach and retraction parts at low and high indentation velocities, a characteristic feature of force-indentation curves of cells [88]. In addition, due to the flexibility of the model to describe simpler mechanical behaviors, such as Kelvin-Voigt or SLL (see Fig. 4.7), it is suitable to be fitted to force-indentation curves of hydrogels that exhibit no hysteresis at low indentation velocities [88]. Ultimately, using the present fitting method, the user is not required to alternate between different models to capture the mechanical nature of different materials and can conveniently compare their fitted parameters.

For validation of the fitting model and demonstration of the method's potential, PAAm and agarose hydrogels were used, each having a different cross-linking mechanism. The PAAm gels exhibited, over the range of different indentation velocities, an elastic behavior accompanied with an apparent viscosity that probably arises from the liquid solvent moving within the elastic polymer network. On the other hand, the agarose gels displayed a viscoelastic behavior that can be explained by the physical crosslinking mechanism of such gels which allows the rearrangement of the polymer network and its contact points during the indentation process.

Finally, HeLa cells were indented in interphase and mitosis cell cycle phases. The interphase cells seemed overall more compliant. However, the mitotic cells exhibited higher values of the Maxwell modulus E_M that lead to higher viscoelastic dissipation during the indentation. Additionally, the apparent viscosity was higher for the interphase cells. These mechanical differences between the cell

cycle phases were also highlighted in a number of other studies [92, 93, 94]. The higher overall stiffness of the mitotic cells was repeatedly attributed to the stiffer actin cortex of these cells which plays an important role in the rounding and the division processes. On the other hand, the lower apparent viscosity of mitotic cells was supposed to be an outcome of the cytoplasmic protein dilution due to water entry and the cell volume increase at this phase [95, 94].

In summary, an analysis method was developed here to extract viscoelastic properties of soft materials from AFM force-indentation curves. The applicability of the method was demonstrated, using the same mechanical model for both hydrogels and cells. This method can be easily incorporated into the conventional analysis of force-indentation curves to broaden the characterization of the rheological properties of soft materials and specifically biological matter.

This chapter vividly demonstrated the potential and the extensibility of the numerical method introduced in Chapter 3.

Chapter 5

Phase field coupled to a deformable solid: Modeling and simulation of soft wetting scenarios

This chapter presents a unified numerical model for wetting of deformable substrates (see Sec. 2.3 for a brief discussion on wetting). A two-phase fluid flow is represented using the phase field model introduced in Sec. 2.2. The setting is now extended to include a soft, (visco-)elastic solid that interacts with the fluid. Note that the method of numerical representation, which will be detailed below, has already been briefly introduced and illustrated in Fig. 2.5. The model developed in this chapter will subsequently be used to study the stick-slip phenomenon in Sec. 5.5. It should be mentioned that the latter is only one example of a wide range of possible scenarios that can be simulated using this method. The content presented here was published by the author in Aland/Mokbel [10] (concerning the numerical model, up to Sec. 5.4) and in Mokbel et al. [11] (concerning stick-slip, Sec. 5.5). Only minor changes in notation and structure are made here.

The following introduction also includes an overview of the structure in this chapter.

5.1 Introduction

Wetting of flexible substrates (also: *soft wetting*, or *elasto-capillarity*) plays a major role in a broad variety of phenomena. Technical applications include the patterning of cells [96] or droplets [97] onto soft surfaces, the optimization of condensation processes [98] or the deposition of droplets in ink-jet printing or additive manufacturing. Also in biology, capillary interactions with flexible materials play a major role in self-organization of cell tissues [99], cell motility [100] and cancer cell migration [101]. Still, our understanding of the dynamics of such soft wetting processes lags far behind of what is known about rigid surfaces [102]. Despite significant progress in computational modeling of (de)wetting

of rigid substrates and the interaction of single fluids with elastic solids separately, the continuum modeling and simulation of wetting of elastic substrates has remained essentially unexplored [28].

One reason for this discrepancy is certainly the challenging nature of the problem, which is inherently multi-scale in space (processes at the micro-scale determine dynamics on the macro-scale) and time (different time scales ranging from microseconds to seconds). Additionally, the strong coupling of hydrodynamics and substrate dynamics near the contact line requires special attention from a numerical point of view. Another reason for the lack of computational results in this field lies in the diversity of the required numerical techniques: the simulation of wetting typically employs interface capturing techniques (like the phase field method [103, 43]), while the interaction of a fluid with an elastic structure (fluid-structure interaction, short: FSI) is typically modeled by interface tracking techniques, in particular the arbitrary Lagrangian-Eulerian (ALE) method [104]. Accordingly, the first simulations of wetting of elastic substrates appeared only very recently [28, 105, 106, 32, 31]. These references comprise basically the whole available literature on numerical simulations of soft wetting at the time of publication of Aland/Mokbel [10]. A work created later is [12], where a ternary phase field approach was used instead of an interface tracking method for FSI. For a brief discussion of general advantages and disadvantages of interface tracking and interface capturing methods, see Sec. 2.4.

The phase field model is probably the most popular continuum model to describe wetting phenomena with moving contact lines. According to Sec. 2.2, the idea is based on an order parameter, the phase field function ϕ , which is used to indicate the fluid phases. The phase field function varies smoothly across the interface leading to a (thin) diffuse interface region. This diffusive nature of the interface regularizes the stress singularity at the contact line, making it a very natural approach for moving contact lines. The rigorous thermodynamic substructure of the model allows for consistent modeling of topological transitions (e.g. [107]), and enables energy stable discrete formulations [43] and robust time discretizations [48]. Consistent boundary conditions for the phase field modeling of wetting have been derived in [29, 108], see also Sec. 2.3.2 in this regard. In [103] an improved phase field model was derived from variational arguments and showed impressive quantitative agreement to molecular dynamics simulations.

Accordingly, the available approaches for simulation of soft wetting [28, 105, 106, 32, 31] all use a combination of different phase field methods for two-phase flow coupled to an ALE discretization of the fluid-solid interaction. For the latter part, advanced standard FSI methods are used in all works. For example, computations on the elastic structure are carried out in a stationary reference domain and mappings are used to transform the corresponding quantities to real space. While this approach is comparatively easy to use for precomputing the stiffness matrix in standard FSI, it requires more complicated strategies in soft wetting, since adaptively changing grids are needed to resolve the region near the contact line. Hence, one could avoid the use of mappings in the ALE discretization by actually moving the grids. Also, the solid incompressibility, which is given for basically any relevant soft material, is not exploited in any of the available numerical methods at the time of publication of

Aland/Mokbel [10].

This chapter aims to exploit these properties to come up with a unified and simpler mathematical model for soft wetting. The model is amenable to a simpler numerical treatment, yet it will be shown that the unified approach makes it numerically more robust with respect to time step restrictions than previous explicit models [28, 105, 106, 32]. In addition, since the solid viscosity can be easily included, soft wetting of a viscoelastic material will be considered for the first time.

The structure of the chapter is as follows. Sec. 5.2 introduces the model equations for the binary fluid and the solid structure together with the corresponding coupling conditions, followed by a reformulation in a unified way. Subsequently, the numerical method including time and space discretization is presented in Sec. 5.3. Benchmark tests and further simulations illustrate the accuracy and efficiency of the method and are carried out in Sec. 5.4. They include the first simulations of the surfing behavior of droplets on a viscoelastic substrate.

In addition, Sec. 5.5 examines a scenario of particular interest to current research, namely the phenomenon of stick-slip contact line motion, to which the present model is applied. Conclusions from this chapter are drawn in Sec. 5.6.

5.2 Mathematical model

5.2.1 Configuration

The domain under consideration is constructed as follows. A two-phase fluid subdomain $\Omega_f \subset \mathbb{R}^d$, consisting of both a fluid and an ambient phase, is connected to a viscoelastic substrate $\Omega_s \subset \mathbb{R}^d$ ($d = 2, 3$). An illustration is given in Fig. 5.1, where the example of a droplet on a substrate is shown. In order to indicate the fluid phases, the phase field function ϕ is introduced, cf. Sec. 2.2. Here, $\phi = 0$ in the ambient phase (liquid or gas) and $\phi = 1$ in the liquid phase. Across the ambient-liquid interface, the phase field varies smoothly, following a tangent hyperbolic profile. This leads to a thin diffuse interface with thickness ϵ , cf. Eqs. (2.16) and (2.17). Furthermore, Γ denotes the sharp fluid-solid interface. The whole domain is denoted by $\Omega = \Omega_f \cup \Omega_s \cup \Gamma$. Three surface tensions are present along the three transition regions. A fluid-fluid tension σ contracts the interface described by the phase field and two solid-fluid tensions, σ_0 and σ_1 , contract the surface of the solid material which is in contact with the ambient and liquid phase, respectively. Note here that the present strategy of numerical representation of free boundaries has already been mentioned in Sec. 2.4.

5.2.2 Governing equations

Binary fluid model

If variable (phase-dependent) densities are involved, different formulations of the phase field model equations have been proposed, e.g. [6, 21, 5]. However, in real scenarios away from the critical

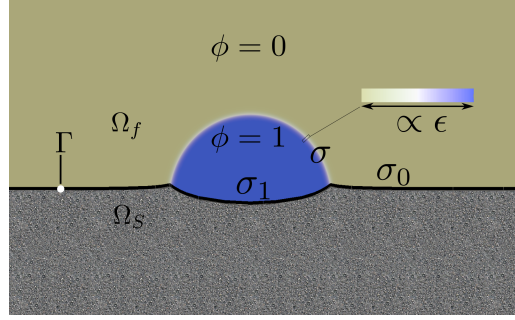


Figure 5.1: Illustration of the soft wetting scenario. A deformable solid domain Ω_s borders on a two-phase fluid domain Ω_f . The two fluids are indicated by the value of the phase field function ϕ . The fluid-fluid interface is diffuse with a thickness ϵ and carries a surface tension σ . The fluid-solid interface Γ has two distinct surface tensions σ_0 and σ_1 depending on the contacting fluid. From Aland/Mokbel [10].

point, the involved interface thickness ϵ is small such that all these models yield comparable results [109]. Therefore, the simplest model from [6] is used here, which considers a volume-averaged velocity formulation with fluid velocity \mathbf{v}_f . The model has also already been derived and presented in Sec. 2.2.5 and Sec. 2.2.6. It reads

$$\left. \begin{aligned} \rho_f(\phi) \partial^\bullet \mathbf{v}_f - \nabla \cdot \mathbb{S}_f &= \mathbf{F} \\ \nabla \cdot \mathbf{v}_f &= 0 \\ \partial^\bullet \phi &= \nabla \cdot (m \nabla q) \\ q &= \tilde{\sigma} \epsilon^{-1} W'(\phi) - \tilde{\sigma} \epsilon \Delta \phi \end{aligned} \right\} \text{in } \Omega_f \quad (5.1)$$

with viscous, pressure and capillary stress

$$\mathbb{S}_f = \eta_f(\phi) (\nabla \mathbf{v}_f + \nabla \mathbf{v}_f^T) - p_f \mathbb{I} - \underbrace{\tilde{\sigma} \epsilon \nabla \phi \otimes \nabla \phi}_{\mathbb{S}_{ca}}. \quad (5.2)$$

Here, the following denotations were used: the material time derivative $\partial^\bullet = d_t + \mathbf{v}_f \cdot \nabla$, the phase-dependent fluid density ρ_f , constant mobility m , the chemical potential q , the double well potential W , the (scaled) fluid-fluid surface tension $\tilde{\sigma}$, the phase-dependent fluid viscosity η_f , and the identity matrix \mathbb{I} . In the present case, the double well potential is chosen as $W(\phi) = \phi^2(1-\phi)^2$, which yields a scaling of a physically motivated surface tension σ according to $\tilde{\sigma} = 3\sqrt{2}\sigma$, see Eq. (2.32).

Compared to previous literature on soft wetting [31], the term

$$\mathbb{I} \left(\frac{\tilde{\sigma} \epsilon}{2} |\nabla \phi|^2 + \frac{\tilde{\sigma}}{\epsilon} W(\phi) - q \phi \right)$$

is omitted here in the definition of the capillary stress \mathbb{S}_{ca} , as it only rescales the interfacial pressure.

That is, the pressure p_f used here, is related to the real physical pressure p_{phys} by

$$p_f = p_{\text{phys}} - \frac{\tilde{\sigma}\epsilon}{2}|\nabla\phi|^2 - \frac{\tilde{\sigma}}{\epsilon}W(\phi) + q\phi.$$

Omitting the left out terms also from the interfacial force balance (Eq. (5.5)₂ below) ensures that this approach is consistent.

Solid elasticity

In the following, the equations of solid elasticity are formulated, which are to be solved in Ω_s . That approach is different from typical approaches in fluid-structure interaction in which the equations are defined on a stationary reference domain and mappings are used to transfer operators to the real physical domain. Furthermore, the present approach exploits the fact that all soft elastic materials (soft wetting occurs typically at Young's moduli in the range of few kPa) are essentially gels, which are incompressible, due to high fluid content. In most work on soft wetting (a notable exception being [31]), this property is approximated by using a Poisson ratio close to 1/2. Instead, the exact incompressibility condition is used here, and the governing equations are accordingly quite similar to the Navier-Stokes equations above. Using a linear elastic model, the equations of momentum and mass conservation are

$$\left. \begin{aligned} \rho_s \partial^\bullet \mathbf{v}_s - \nabla \cdot \mathbb{S}_s &= \mathbf{F} \\ \nabla \cdot \mathbf{v}_s &= 0 \end{aligned} \right\} \text{ in } \Omega_s \quad (5.3)$$

with viscous, pressure and elastic stress

$$\mathbb{S}_s = \eta_s (\nabla \mathbf{v}_s + \nabla \mathbf{v}_s^T) - p_s \mathbb{I} + \underbrace{G (\nabla \mathbf{u} + \nabla \mathbf{u}^T - \nabla \mathbf{u}^T \nabla \mathbf{u})}_{\mathbb{S}_{\text{el}}} . \quad (5.4)$$

Here, $\partial^\bullet = d_t + \mathbf{v}_s \cdot \nabla$ denotes the material time derivative including the solid velocity \mathbf{v}_s . Furthermore, ρ_s , η_s and G denote the solid density, solid viscosity and elastic shear modulus, respectively. Additionally, \mathbf{u} is a displacement field, i.e. the difference between current coordinates and initial coordinates of material points. This displacement field can be tracked either by an additional PDE, $\partial^\bullet \mathbf{u} = \mathbf{v}_s$ in Ω_s , or by moving the grid with the velocity \mathbf{v}_s while memorizing initial coordinates $\hat{\mathbf{x}}$ of each grid point, such that $\mathbf{u} = \mathbf{x} - \hat{\mathbf{x}}$. The latter approach is used in this work.

Note that the elastic stress \mathbb{S}_{el} in Eq. (5.4) includes the nonlinear Euler-Almansi term to make the model geometrically nonlinear. Contrary to previous approaches for numerical simulation of soft wetting, the solid material includes a viscosity, which leads to an effective description as a Kelvin-Voigt viscoelastic material. The viscosity of the solid is relevant for many dynamic phenomena in soft wetting, and its influence is hardly understood [1].

Moreover, note that in general G can be chosen as an arbitrary time- and space-dependent function in Ω_s , e.g. in order to implement an elasticity gradient in the substrate (for example to describe durotaxis [97]). However, throughout this work G is assumed to be constant.

Coupling conditions

The following coupling conditions apply at the solid-fluid interface Γ :

$$\left. \begin{aligned} \mathbf{v}_f &= \mathbf{v}_s \\ \mathbb{S}_f \cdot \mathbf{n} &= \mathbb{S}_s \cdot \mathbf{n} + \nabla_\Gamma \cdot (\sigma_s(\phi) \mathbb{P}) \\ d_t \phi + \mathbf{v}_f \cdot \nabla \phi &= -\nu (\tilde{\sigma} \epsilon \mathbf{n} \cdot \nabla \phi + \sigma'_s(\phi)) \\ \mathbf{n} \cdot \nabla q &= 0 \end{aligned} \right\} \text{ on } \Gamma . \quad (5.5)$$

The first equation is the continuity of velocities across the interface which is equal to the usual no-slip condition. This condition also implies a topological condition which ensures that Ω_f and Ω_s are contiguous at the interface (see Sec. 5.3.1). In typical sharp interface formulations such a no-slip condition results in a pinning of the fluid-fluid contact line to the solid boundary. This effect, also known as contact line singularity, is overcome in the present phase field model. Here, the fluid-fluid interface can move not only by advection, but also by the Cahn-Hilliard diffusion. The corresponding equations are constructed from energetic arguments, such as to minimize the overall surface energy (i.e. to realize the correct contact angles). Hence, the use of a phase field model for the fluid-fluid interface is an elegant and physically motivated way to avoid the contact line singularity.

The second equation is the dynamic condition which describes the balance of forces across the interface (namely traction and capillary stress). Here, \mathbf{n} is the outer normal to Ω_f . The solid surface tension $\sigma_s(\phi)$ represents the tension along Γ between the solid and the fluid indicated by the value of the phase field. It is important to emphasize here that σ_s is defined only in Ω_f , since in Ω_s no phase field is given. According to the derivation in Sec. 2.3.2 and Sec. 2.3.3, it is set to the following differentiable function of the phase field: $\sigma_s(\phi) = (\sigma_1 - \sigma_0) \phi^2 (3 - 2\phi) + \sigma_0$, which implies $\sigma_s(0) = \sigma_0$ and $\sigma_s(1) = \sigma_1$. Further, $\nabla_\Gamma \cdot$ denotes the surface divergence operator and $\mathbb{P} = \mathbb{I} - \mathbf{n} \otimes \mathbf{n}$ is the surface projection operator. Note that the present formulation coincides with the boundary conditions given in [28, 105, 31] as $\nabla_\Gamma \cdot (\sigma_s(\phi) \mathbb{P}) = \sigma_s(\phi) \kappa \mathbf{n} + \nabla_\Gamma \sigma_s(\phi)$ with $\kappa = -\nabla_\Gamma \cdot \mathbf{n}$ being the total curvature. Further note that condition (5.5)₂ also results from the previous derivation in Sec. 2.3.2 and corresponds to Eq. (2.64), here extended by the contribution of the solid stress \mathbb{S}_s .

The third equation, Eq. (5.5)₃ is responsible for the formation of a dynamic contact angle and was also derived in Sec. 2.3.2, where ν denotes a relaxation parameter. Furthermore, this condition has been presented previously in a variational model for moving contact lines in [103]. When ν tends to infinity, the equation reduces to the static contact angle condition $\tilde{\sigma} \epsilon \mathbf{n} \cdot \nabla \phi = -\sigma'_s(\phi)$, which is used for the numerical simulations in this chapter. Moreover, note that both the kinematic and the

topological condition are comparable to those in conventional FSI problems. However, the dynamic condition as well as Eq. (5.5)₃ differ from conventional FSI problems in terms of contribution of the capillary stress \mathbb{S}_{ca} and the fluid-solid surface tension σ_s , leading to a discontinuity of the traction across the interface (see also Sec. 2.3 of [31]).

Finally, Eq. (5.5)₄ ensures mass conservation (no penetration) on Γ . With this, a closed system of equations is now specified (up to outer boundary conditions) for the unknown variables $\mathbf{v}_f, p_f, \mathbf{v}_s, p_s, \phi, q$.

5.2.3 Unified model

This section presents a unification of the previously described equations of binary fluid-structure interaction, cf. [110] for a similar approach. The first step is to exploit the continuity of velocity (5.5)₁ to introduce the common velocity field \mathbf{v} with $\mathbf{v} = \mathbf{v}_s$ in Ω_s and $\mathbf{v} = \mathbf{v}_f$ in Ω_f . Accordingly, the material time derivative is now denoted by $\partial^\bullet = d_t + \mathbf{v} \cdot \nabla$. The fact that the domain Ω_s is not a reference domain, but moves with the material, makes it possible to define a common connected computational domain $\Omega := \Omega_s \cup \Omega_f$. In this domain, let χ_f and χ_s be the characteristic functions to distinguish the domain parts, that is, $\chi_\alpha = 1$ in Ω_α for $\alpha \in \{f, s\}$ and zero anywhere else. The surface Γ is identified with the surface Dirac delta function δ_Γ . This notation allows to add up the variational forms of the equations and to end up with

$$\left. \begin{aligned} \bar{\rho} \partial^\bullet \mathbf{v} - \nabla \cdot (\bar{\eta} (\nabla \mathbf{v} + \nabla \mathbf{v}^T)) + \nabla (\chi_f p_f + \chi_s p_s) = \\ -\nabla \cdot (\chi_f \mathbb{S}_{ca}) + \nabla \cdot (\chi_s \mathbb{S}_{el}) - \delta_\Gamma \nabla_\Gamma \cdot (\sigma_s \mathbb{P}) + \mathbf{F} \\ \nabla \cdot \mathbf{v} = 0 \end{aligned} \right\} \text{in } \Omega. \quad (5.6)$$

Here, $\bar{\rho} = \bar{\rho}(\mathbf{x}, \phi(\mathbf{x}))$ and $\bar{\eta} = \bar{\eta}(\mathbf{x}, \phi(\mathbf{x}))$ are the space-dependent density and viscosity, interpolated in the way that

$$\bar{\rho}(\mathbf{x}, \phi(\mathbf{x})) = \begin{cases} \rho_s & \mathbf{x} \in \Omega_s \\ (\rho_{f,1} - \rho_{f,0}) \phi(\mathbf{x}) + \rho_{f,0} & \mathbf{x} \in \Omega_f, \phi(\mathbf{x}) \in [0, 1] \\ \rho_{f,0} & \mathbf{x} \in \Omega_f, \phi(\mathbf{x}) < 0 \\ \rho_{f,1} & \mathbf{x} \in \Omega_f, \phi(\mathbf{x}) > 1, \end{cases}$$

where $\rho_{f,1}$ and $\rho_{f,0}$ denote the density in the liquid and in the ambient phase, respectively. The last two case distinctions are necessary to limit $\bar{\rho}$ to physically meaningful values. The reason for this is that the phase field does not satisfy a maximum principle, hence its values can slightly exceed the interval $[0, 1]$, which can create unphysical density, especially for large differences between $\rho_{f,0}$ and $\rho_{f,1}$. This type of interpolation also applies in an analogous manner to $\bar{\eta}$.

Equation (5.6) consolidates Eqs. (5.1)₁-(5.1)₂, (5.2), (5.3), (5.4). Additionally also the kinematic and dynamic coupling conditions Eqs. (5.5)₁-(5.5)₂ are included. This yields a single Navier-Stokes equation which incorporates momentum and mass balance of fluid and solid phases together with the

interfacial balance of forces in a monolithic way. Therefore, this formulation is expected to provide superior stability of the numerical method, while greatly simplifying the numerical treatment of the system, as will be shown in Sec. 5.4.1.

For completeness, note here that these equations are still accompanied by the Cahn-Hilliard system in the fluid domain:

$$\left. \begin{aligned} \partial^\bullet \phi &= \nabla \cdot (m \nabla q) \\ q &= \tilde{\sigma} \epsilon^{-1} W'(\phi) - \tilde{\sigma} \epsilon \Delta \phi \end{aligned} \right\} \text{ in } \Omega_f, \quad (5.7)$$

equipped with the boundary conditions (5.5)₃-(5.5)₄.

5.3 Discretization

5.3.1 ALE discretization

The arbitrary Lagrangian-Eulerian (ALE) method is used here to discretize the numerical grids, see Sec. 2.4. The two domains Ω_s and Ω_f are discretized on two separate but connected, moving numerical grids. Within the elastic structure as well as on Γ , grid points move with the material velocity \mathbf{v} , i.e. they are material points. In contrast, the grid points in the fluid structure move with a continuous harmonic extension of this velocity in order to keep a proper shape of the mesh. In this work, the grid velocity \mathbf{v}_{Grid} is calculated in the fluid domain by solving the Bi-Laplace problem

$$\begin{aligned} \Delta^2 \mathbf{v}_{\text{Grid}} &= 0 && \text{in } \Omega_f \\ \mathbf{v}_{\text{Grid}} &= \mathbf{v}, \quad \mathbf{n} \cdot \nabla \Delta \mathbf{v}_{\text{Grid}} = 0 && \text{on } \Gamma \\ \Delta \mathbf{v}_{\text{Grid}} &= \mathbf{v}_{\text{Grid}} = 0 && \text{on } \partial\Omega_f \setminus \Gamma \end{aligned} \quad (5.8)$$

and $\mathbf{v}_{\text{Grid}} = \mathbf{v}$ in Ω_s . Alternatively, other methods can also be used to extend the grid velocity into the fluid domain, for example by penalizing length changes of triangles/tetrahedra, see [111] for more details.

The calculated grid velocity \mathbf{v}_{Grid} is then subtracted in all convective terms of the governing equations. Therefore, the material derivate ∂^\bullet is replaced by

$$d_t + (\mathbf{v} - \mathbf{v}_{\text{Grid}}) \cdot \nabla,$$

where d_t now denotes the time derivative along a quantity on a moving grid point.

5.3.2 Time discretization

The problem is discretized with equidistant time steps of size τ . At each time step, the general workflow of the numerical solution procedure is as follows. First, the coupled system of momentum

balance, mass balance, and phase field evolution, Eqs. (5.6)-(5.7) is solved in one monolithic system. Afterwards the grid velocity \mathbf{v}_{Grid} is computed as explained in the previous subsection. Then in a last step, the grid is updated, i.e. each grid point is moved by the corresponding value of \mathbf{v}_{Grid} .

An IMEX (implicit/explicit) Euler method is used to formulate a time discretization of Eqs. (5.6)-(5.7) which is linear in the solution variables. In the following, quantities on discrete time points are denoted by a superscript, where $()^{n-1}$ refers to the previous time step and $()^n$ refers to the current time step. Explicit discretizations (i.e. step $n-1$) are used for the nonlinear elastic term and most occurrences of the phase field in the momentum balance. The linear elastic term is taken implicitly, $G(\nabla \mathbf{u}^n + (\nabla \mathbf{u}^n)^T)$, by using the identity $\mathbf{u}^n = \mathbf{u}^{n-1} + \tau \mathbf{v}^n$ (see also [110]). This yields an explicit part $G(\nabla \mathbf{u}^{n-1} + (\nabla \mathbf{u}^{n-1})^T)$ and an implicit part $\tau G(\nabla \mathbf{v}^n + (\nabla \mathbf{v}^n)^T)$, which effectively leads to an increment of the solid viscosity by τG .

Additionally, stability is increased by an implicit treatment of the fluid-fluid surface tension force. The capillary stress \mathbb{S}_{ca} is taken semi-implicitly by using $\tilde{\sigma} \epsilon \nabla \phi^n \otimes \nabla \phi^{n-1}$. Note, that the involved tensor product is defined such that $[\nabla \cdot (\nabla \phi^n \otimes \nabla \phi^{n-1})]_i = \sum_j \partial_j (\partial_j \phi^n \partial_i \phi^{n-1})$. It should be emphasized here that the alternative discretization $\tilde{\sigma} \epsilon \nabla \phi^{n-1} \otimes \nabla \phi^n$ does not lead to a stabilizing effect, since only the first occurrence of $\nabla \phi$ effectively contains the interface curvature, see [48] for a more detailed discussion of stabilization of large surface tension in phase field models. This treatment must be accompanied by using the new velocity field \mathbf{v}^n in the advective term of the phase field. Further, the nonlinear derivative of the double well potential $W'(\phi)$ is linearized by a first order Taylor expansion. Finally, this results in the following time discrete formulation of the system:

In each time step n , find $\mathbf{v}^n, p_f^n, p_s^n, \phi^n, q^n$ such that

$$\left. \begin{aligned} \bar{\rho}^{n-1} \left(\frac{\mathbf{v}^n - \mathbf{v}_*^{n-1}}{\tau} + (\mathbf{v}^{n-1} - \mathbf{v}_{\text{Grid}}^{n-1}) \cdot \nabla \mathbf{v}^n \right) = \\ -\nabla (\chi_f^{n-1} p_f^n + \chi_s^{n-1} p_s^n) + \nabla \cdot ((\bar{\eta}^{n-1} + \chi_s^{n-1} \tau G) (\nabla \mathbf{v}^n + (\nabla \mathbf{v}^n)^T)) \\ + \nabla \cdot (\chi_s \mathbb{S}_{\text{el}})^{n-1} - \nabla \cdot (\chi_f^{n-1} \tilde{\sigma} \epsilon \nabla \phi^n \otimes \nabla \phi^{n-1}) - \delta_{\Gamma}^{n-1} \nabla_{\Gamma} \cdot (\sigma_s(\phi) \mathbb{P})^{n-1} + \mathbf{F} \\ \nabla \cdot \mathbf{v}^n = 0 \end{aligned} \right\} \text{in } \Omega^{n-1} \quad (5.9)$$

$$\left. \begin{aligned} \frac{\phi^n - \phi_*^{n-1}}{\tau} + (\mathbf{v}^n - \mathbf{v}_{\text{Grid}}^{n-1}) \cdot \nabla \phi^{n-1} = \nabla \cdot (m \nabla q^n) \\ q^n = \tilde{\sigma} \epsilon^{-1} (W'(\phi^{n-1}) + W''(\phi^{n-1})(\phi^n - \phi^{n-1}) - \tilde{\sigma} \epsilon \Delta \phi^n) \end{aligned} \right\} \text{in } \Omega_f^{n-1}. \quad (5.10)$$

Here \mathbf{v}_*^{n-1} and ϕ_*^{n-1} denote the corresponding quantities from the last time step, but after the applied change of the grid point coordinates due to the mesh update. Further, $\bar{\rho}^{n-1} = \bar{\rho}(\mathbf{x}, \phi^{n-1}(\mathbf{x}))$, $\bar{\eta}^{n-1} = \bar{\eta}(\mathbf{x}, \phi^{n-1}(\mathbf{x}))$.

5.3.3 Space discretization

In the present finite element approach, separate triangulations T_f of Ω_f and T_s of Ω_s are considered, where the membrane Γ connecting the two domains is triangulated by $T_\Gamma = T_f \cap T_s$. In particular, the connection is ensured by the fact that every grid point on the interface of Ω_f has a corresponding grid point on the interface of Ω_s , sharing the same point coordinates. This allows us to enforce continuity of velocity across Γ , as well as to implement the jump conditions of the stress there. For an example illustration of the numerical mesh, see Fig. 5.2.

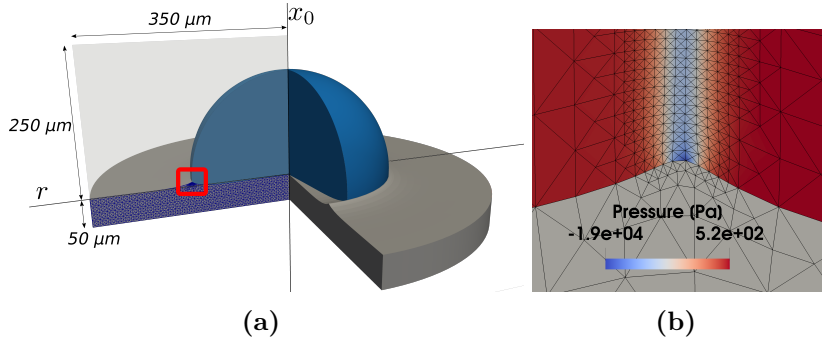


Figure 5.2: Illustration of the setup in the numerical simulations. In (a), the two-dimensional computational domain is indicated by the transparent rectangle. The substrate is represented by a solid gray color, the liquid phase by blue and the ambient is invisible. Additionally, the solid mesh is shown. The mesh at the contact line, marked by the red rectangular, is presented in (b). The solid domain is illustrated in grey, while the coloring in the fluid domain represents the pressure. Adapted from Aland/Mokbel [10].

The combined discrete system of Eqs. (5.1) - (5.5) in the weak form is presented in the following. The finite element spaces read

$$\begin{aligned}
 V_h &:= \left\{ v \in C^0(\bar{\Omega}) \cap H^1(\Omega) \mid v|_k \in P_2(k), k \in T_f \cup T_s \right\} \\
 P_{h,\alpha} &:= \left\{ p \in C(\bar{\Omega}_\alpha) \cap L^2(\Omega_\alpha) \mid p|_k \in P_1(k), k \in T_\alpha \right\}, \alpha = s, f \\
 C_h &:= \left\{ c \in C^0(\bar{\Omega}_f) \cap H^1(\Omega_f) \mid c|_k \in P_2(k), k \in T_f \right\}.
 \end{aligned} \tag{5.11}$$

Here, V_h is the finite element space for the components of the velocity \mathbf{v} . It ensures continuity of the respective variables across T_Γ . Note that in Eq. (5.11)₂, α denotes a placeholder for the distinction between the solid and the fluid domain. The use of two separate spaces, $P_{h,f}$ and $P_{h,s}$, is motivated by the discontinuity of pressure across Γ caused by the solid surface tension. The use of standard finite element spaces for the discretization of the discontinuous pressure leads to poor numerical properties, with an approximation order of only $\mathcal{O}(\sqrt{h})$ with respect to the L^2 norm [112]. Accordingly, the usage of two separate spaces, $P_{h,f}$ and $P_{h,s}$, extends the standard Taylor-Hood finite element space

by additional degrees of freedom of the pressure at the interface, such that the discontinuity can be exactly resolved. The remaining finite element space C_h refers to ϕ and q in Eqs. (5.1)₃ and (5.1)₄.

Navier-Stokes system

The previous arguments now allow to establish a uniform weak formulation of the momentum and mass conservation equation for the combined domain Ω . The weak form reads:

Find $(\mathbf{v}^n, p_f^n, p_s^n) \in V_h^d \times P_{h,f} \times P_{h,s}$, such that $\forall (\mathbf{z}, q_f, q_s) \in V_h^d \times P_{h,f} \times P_{h,s}$:

$$\begin{aligned}
0 &= \int_{\Omega^{n-1}} \bar{\rho}^{n-1} \left(\frac{\mathbf{v}^n - \mathbf{v}_*^{n-1}}{\tau} + (\mathbf{v}^{n-1} - \mathbf{v}_{\text{Grid}}^{n-1}) \cdot \nabla \mathbf{v}^n \right) \cdot \mathbf{z} \\
&\quad + (\bar{\eta}^{n-1} + \chi_s^{n-1} \tau G) (\nabla \mathbf{v}^n + (\nabla \mathbf{v}^n)^T) : \nabla \mathbf{z} - \mathbf{F} \cdot \mathbf{z} \, \text{d}\mathbf{x} \\
&\quad - \int_{\Omega_f^{n-1}} \tilde{\sigma} \epsilon \nabla \phi^n \otimes \nabla \phi^{n-1} : \nabla \mathbf{z} + p_f^n \nabla \cdot \mathbf{z} \, \text{d}\mathbf{x} \\
&\quad + \int_{\Omega_s^{n-1}} G (\nabla \mathbf{u} + (\nabla \mathbf{u})^T - (\nabla \mathbf{u})^T \nabla \mathbf{u})^{n-1} : \nabla \mathbf{z} - p_s^n \nabla \cdot \mathbf{z} \, \text{d}\mathbf{x} \\
&\quad + \int_{\Gamma^{n-1}} (\nabla_{\Gamma} \cdot (\sigma_s(\phi) \mathbb{P}))^{n-1} \cdot \mathbf{z} \, \text{d}\mathbf{x}, \tag{5.12}
\end{aligned}$$

$$0 = \int_{\Omega_f^{n-1}} q_f \nabla \cdot \mathbf{v}^n \, \text{d}\mathbf{x} + \int_{\Omega_s^{n-1}} q_s \nabla \cdot \mathbf{v}^n \, \text{d}\mathbf{x}. \tag{5.13}$$

Cahn-Hilliard system

Since the rest of this chapter considers a static contact angle condition, Eq. (5.5)₃ simplifies to $\tilde{\sigma} \epsilon \mathbf{n} \cdot \nabla \phi = -\sigma'_s(\phi)$. The weak form of Eqs. (5.1)₃ and (5.1)₄ equipped with boundary conditions (5.5)₃- (5.5)₄ then reads:

Find $(\phi^n, q^n) \in C_h \times C_h$ such that $\forall (\psi_1, \psi_2) \in C_h \times C_h$

$$0 = \int_{\Omega_f^{n-1}} \left(\frac{\phi^n - \phi_*^{n-1}}{\tau} + (\mathbf{v}^n - \mathbf{v}_{\text{Grid}}^{n-1}) \cdot \nabla \phi^{n-1} \right) \psi_1 + m \nabla q^n \cdot \nabla \psi_1 \, \text{d}\mathbf{x} \tag{5.14}$$

$$\begin{aligned}
0 &= \int_{\Omega_f^{n-1}} q^m \psi_2 - \tilde{\sigma} \epsilon \nabla \phi^n \cdot \nabla \psi_2 - \frac{\tilde{\sigma}}{\epsilon} (W'(\phi^{n-1}) + W''(\phi^{n-1})(\phi^n - \phi^{n-1})) \psi_2 \, \text{d}\mathbf{x} \\
&\quad - \int_{\Gamma^{n-1}} \sigma'_s(\phi^{n-1}) \psi_2 \, \text{d}\mathbf{x}, \tag{5.15}
\end{aligned}$$

where the nonlinear derivative of the double well potential $W'(\phi)$ is linearized by a Taylor expansion of first order. Note that the Cahn-Hilliard system is still directly coupled to the Navier-Stokes system by the presence of ϕ^n in Eq.(5.12) and the presence of \mathbf{v}^n in Eq. (5.14). This coupling, which removes time step restrictions for small interface length [48], is linear. Hence, the coupled system can be solved by assembling Eqs. (5.12)-(5.15) in a monolithic way, and no subiterations are needed.

5.4 Numerical tests

5.4.1 Validation study

This section starts the verification and validation of the proposed model with a popular wetting test case: the relaxation of an initially half-spherical droplet on a substrate. The author's work Aland/Mokbel [10] presented here aimed to reproduce the numerical reference results in [31] and the experimental data presented in [113] to follow up this benchmark case. The computational setup and parameters are chosen according to [31] and are repeated here for completeness.

As indicated in Fig. 5.2, a cylindrical computational domain with radius 350 μm and height 300 μm is considered. The bottom of the domain consists of a 50 μm thick soft elastic substrate. A liquid droplet is placed in the center of the substrate. The shape of the drop is initially a spherical cap with radius $R_C \approx 177.8 \mu\text{m}$, centered slightly above the substrate surface, such that the fluid-ambient contact line assumes the equilibrium contact angle on the flat substrate. Note that this alignment of the correct initial contact angle is not a necessity of the numerical algorithm but is used to comply with [31]. For an initially undeformed planar substrate the contact angle θ is given by Young's relation

$$\cos \theta = \frac{\sigma_0 - \sigma_1}{\sigma},$$

which applies only to flat rigid substrates, see Sec. 2.3. In particular the time-dependent order parameter $\phi(t, \mathbf{x})$ initially reads (cf. Eqs. (2.16), (2.58))

$$\phi(0, \mathbf{x}) = \frac{1}{2} + \frac{1}{2} \tanh\left(\frac{R_C - |\mathbf{x} - \mathbf{x}_C|}{\epsilon\sqrt{2}}\right),$$

where the center \mathbf{x}_C of the spherical cap is placed such that its distance to the surface of the substrate is $|R_C \cos \theta|$ [31]. Furthermore, the following surface tensions are chosen:

$$\sigma = 46 \frac{\text{mN}}{\text{m}}, \quad \sigma_1 = 36 \frac{\text{mN}}{\text{m}}, \quad \sigma_0 = 31 \frac{\text{mN}}{\text{m}},$$

which leads to an equilibrium contact angle of approximately 96.24° and a distance of \mathbf{x}_C to the substrate of $R_C \left| \frac{\sigma_0 - \sigma_1}{\sigma} \right| \approx 19.3 \mu\text{m}$.

The shear modulus of the soft substrate has been reported to be $G = 1 \text{ kPa}$ [31]. The width of the fluid-fluid interface is set to $\epsilon = 2 \mu\text{m}$, which is sufficiently smaller than the elastocapillary length $\frac{\sigma}{G}$. That is, soft solid behavior and the formation of a three-phase contact angle can be expected, which should roughly follow Neumann's triangle, see Sec. 2.3 and [23]. Further parameters are

$$\begin{aligned} \rho_{f,0} &= 1 \frac{\text{kg}}{\text{m}^3}, & \rho_{f,1} &= 1260 \frac{\text{kg}}{\text{m}^3}, & \rho_s &= 1000 \frac{\text{kg}}{\text{m}^3}, \\ \eta_{f,0} &= 0.1 \text{ Pa} \cdot \text{s}, & \eta_{f,1} &= 1.41 \text{ Pa} \cdot \text{s}, & \eta_s &= 0.005 \text{ Pa} \cdot \text{s}. \end{aligned} \tag{5.16}$$

Since a solid viscosity is not included in [31], η_s is chosen to be negligibly small here. In the associated experiment, the data are measured examining a glycerol droplet in air on a silicone-gel layer. Note that ambient parameters, $\rho_{f,0}, \eta_{f,0}$, in 5.16 are chosen to comply with [31]. There the authors deviated from the physical values of air as used in the experiment [113], to improve numerical stability. The experimental results are only compared in the stationary state, which is independent on ambient viscosity and density.

At the bottom boundary of the solid substrate $\mathbf{v} = 0$ holds, while a free-slip condition is set at all other outer boundaries of the domain.

As in [31], an axisymmetric implementation of the method is chosen to incorporate the rotational symmetry of the experimental setup, which amounts to performing simulations in the two-dimensional $x_0 - r$ plane. According to Fig. 5.2, x_0 and r refer to the coordinates in axial and radial direction, respectively. The same finite-element spaces are used as described in Eq. (5.11), with dimension $d = 2$. Axisymmetry is realized on the level of differential operators by using an axisymmetric divergence and Laplace operator, which replace the corresponding operators in Eqs. (5.9),(5.10). To compute the axisymmetric divergence of the viscous and elastic stress and the projection matrix, additional terms have to be implemented to account for the missing tensor components in 2D. For a more detailed overview of the time-discrete axisymmetric Navier-Stokes and Cahn-Hilliard system, see Sec. 3.5. Further, the solid surface tension force is reformulated as $\nabla_\Gamma \cdot (\sigma_s(\phi) \mathbb{P}) = \sigma_s(\phi) \kappa \mathbf{n} + \nabla_\Gamma \sigma_s(\phi)$, as described in Sec. 5.2.2. Here, $\kappa = -\nabla_\Gamma \cdot \mathbf{n}$ is the total curvature of the solid surface which is computed in the discrete axisymmetric setting as in Sec. 4.2 of [111].

To resolve the dynamics of the wetting ridge formation, the time step size is set to $2 \mu\text{s}$. The distance between the grid nodes is $0.39 \mu\text{m}$ along the interface, which leads to approximately 16 degrees of freedom across the interface region ($\phi \in [0.1, 0.9]$, cf. Eq. (2.17)). The grid size is increased away from the interface region to a maximum node distance of $6.25 \mu\text{m}$. The constant mobility is set to $m = 0.01 \frac{\text{m}^3\text{s}}{\text{kg}}$.

The first benchmark of interest is the equilibrium profile of the substrate, for which the choice of fluid and ambient viscosities and the material densities is not relevant. Fig. 5.3(a) shows the resulting profile at $t = 6 \text{ ms}$ in the (almost) stationary state. Maximum strain is about 30% in a very small region near the tip of the wetting ridge. A comparison with the reference simulation shows a very good agreement in both, the substrate profile under the droplet as well as the wetting ridge. The slightly smaller height of the wetting ridge could be explained by the fact that we model a linear elastic material in contrast to the Neo-Hookean material in the reference. This is also confirmed by comparing to [28] where a linear elastic model lead to a height of slightly less than $7 \mu\text{m}$ for the wetting ridge, which is exactly the same as in our simulations. However the results of [28] are not included in the comparison as they deviate largely in the indentation of the soft substrate below the droplet. Already in the original paper the authors conjectured that this discrepancy is related to compressibility effects due

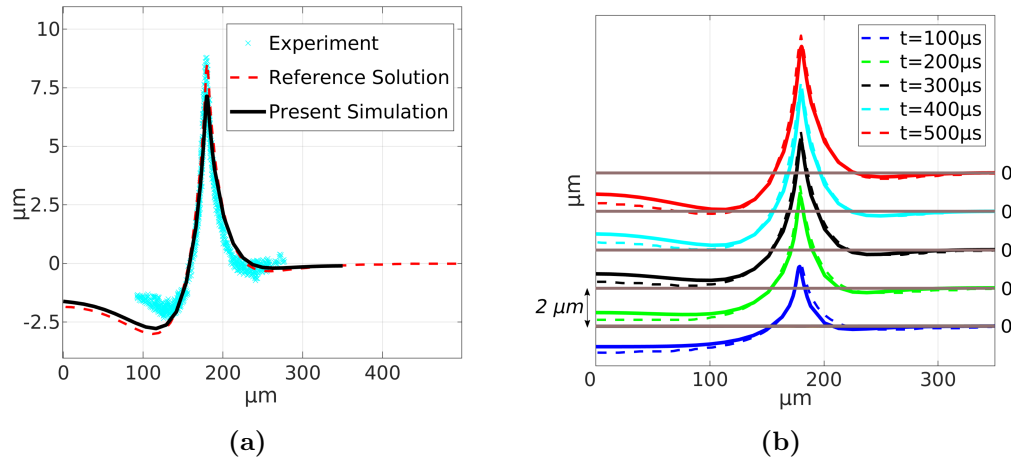


Figure 5.3: Height profile of the deformed elastic substrate. The left vertical axis corresponds to the axis of symmetry. In (a), the equilibrium profile line of the substrate is shown. The black solid line represents the result of the present simulation at time $t = 6 \text{ ms}$, the dashed red line is the reference result in [31], and the cyan crosses show the experimental results in [113]. All data to reproduce the graph were published in [114]. Part (b) indicates the evolution of the wetting ridge at 5 different times (solid lines) in comparison to the reference values from [31] (dashed lines). The coordinate system was repeatedly shifted by $2 \mu\text{m}$ for better visibility with initial position of the substrate indicated by the horizontal lines. From Aland/Mokbel [10].

to their pseudo-incompressible solid model. Moreover, the comparison of the simulation results with the experimental data from [113] also shows a good agreement, especially in the wetting ridge region. Since the stationary wetting ridge profile can be considered as a standard benchmark case for soft wetting, all data to reproduce Figure 5.3(a) were published in [114].

Fig. 5.3(b) shows the evolution of the profile line between $t = 100 \mu\text{s}$ and $t = 500 \mu\text{s}$, in which a large part of the clearly observable dynamic behavior takes place. At this point it is necessary to choose viscosities and densities that match the reference. Using the above mentioned values refers to test case 2 in [31]. A good agreement in the comparison to the reference is also shown here.

5.4.2 Time step stability

The used time step size of $2 \mu\text{s}$ was chosen so that in particular a precise analysis of the evolution of the wetting ridge is possible. The small time step size ensures that kink formation ($\sim \mu\text{s}$) and ridge formation ($\sim \text{ms}$) are reasonably well resolved. Many interesting soft wetting effects happen on larger time scales of seconds or minutes (e.g. droplet motion, cheerios effect, soft nucleation). Obviously, much larger time steps are necessary to resolve these phenomena within reasonable computation time. In this case, one can sacrifice temporal accuracy during the formation of the wetting ridge, as one is more interested to resolve the (slower) motion of an already formed ridge moving over the substrate. However, the necessary larger time steps may pose problems to numerical algorithms as stability

restrictions kick in. Such restrictions were investigated for the above benchmark problem in detail in [28]. It was reported that restrictions emerge due to the explicit coupling of fluid and solid equations. It was also shown that restrictions are independent of the added mass effect. To get a convergent solution in each time step, subiterations with underrelaxation were necessary. The largest stable relaxation factor was found $\sim 10^{-2}$ which means that on the order of 10^2 subiterations were necessary in each time step. This reduces the reported time step size of $10\ \mu\text{s}$ to an “effective” time step size of $0.1\ \mu\text{s}$. Similarly, in [32] time step sizes of $1\ \mu\text{s}$ were chosen to conduct the same benchmark study. Nothing is reported on stability requirements there, but it can be expected that much larger time steps also posed problems, as the computations took already 47h on 128 cores.

The unified approach for the fluid and solid equations presented here seems to stabilize the coupling significantly. The numerical simulations of the benchmark example are found to be stable for time step sizes of up to $16\ \mu\text{s}$ without any subiterations. For higher time step size the explicit coupling of velocity evolution and geometry evolution (grid movement) becomes unstable. While this time step size is already much larger than the sizes reported in previous literature on soft wetting (except for the fully monolithic approach in [31]), the stability can be further increased by considering matched viscosities and densities, which is a valid assumption to obtain the equilibrium state. For example, with the choice $\rho_{f,0} = \rho_{f,1} = 1260\ \text{kg/m}^3$, $\eta_{f,0} = \eta_{f,1} = \eta_s = 1.41\ \text{Pa} \cdot \text{s}$ the time step size may be increased to $128\ \mu\text{s}$. Also, coarsening of the finite element grid leads to weaker time step restrictions. In our case, we found that doubling the mesh size enabled approximately 4 times larger time steps ($512\ \mu\text{s}$). A more detailed study on time step restrictions, stability criteria and time stepping errors is left for future work.

Note that the method still contains an explicit coupling of geometry evolution and flow computation. It can therefore not cope with a completely implicit coupling as recently proposed in [31]. There the authors showed that their fully monolithic solution procedure can provide robust results at time step size of $1000\ \mu\text{s}$, and probably even above. The fully implicit coupling however complicates the solution procedure, including automatic differentiation, Newton iterations and a technique called ϵ -continuation. Despite being not as robust as this fully implicit approach, the method proposed here is more compact and can provide results at low computation time of each time step (35s per time step for the benchmark example on the finest grid with $\approx 280,000$ DOFs on a single core).

5.4.3 Fluid substrates

This subsection illustrates that the present approach is capable to describe even much softer substrates. To this end, the extreme case is assumed where the substrate is a purely viscous fluid without elasticity. This approach is particularly interesting for multi-phase flow with free surfaces, such as gas-water-oil mixtures. Fig. 5.4 shows the scenario of the above benchmark test case, but now with $G = 0\ \text{Pa}$. Fig. 5.4(b) illustrates the significantly different dynamics during the first 1000 microseconds that result from the omission of an elastic influence. While the elastic substrate is already close to the

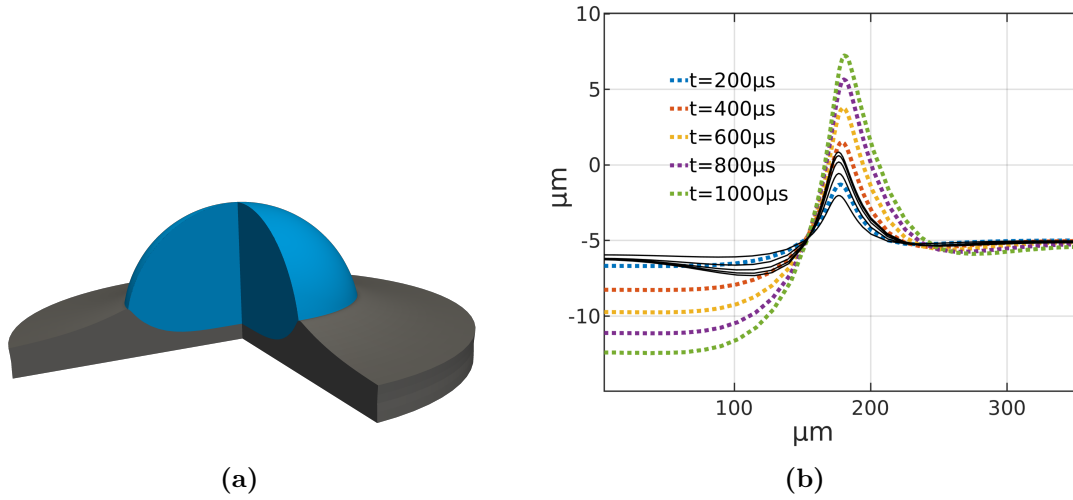


Figure 5.4: Simulations of a droplet on a fluid substrate. (a) The droplet has sunk far into the substrate at $t = 6$ ms. (b) The dynamics of substrate profiles (left axis is the axis of symmetry). The simulation results for $G = 0$ Pa are shown by the dotted, colored lines. The black solid lines represents the corresponding equilibrium profile with $G = 1000$ Pa for comparison (cf. Fig. 5.3). Parameters are as in Sec. 5.4.1, but now with a fluid substrate, $G = 0$ Pa, $\eta_s = 0.1$ Pa \cdot s, $\epsilon = 8$ μ m. From Aland/Mokbel [10].

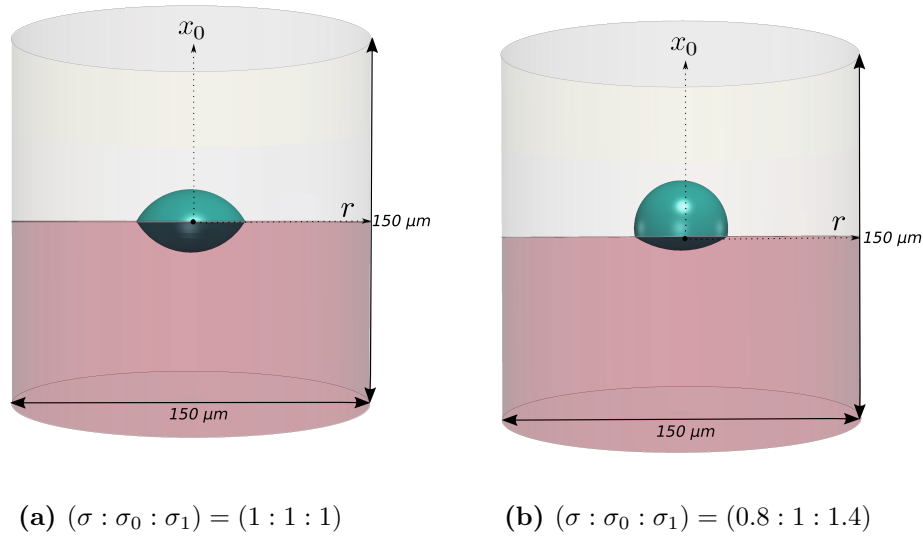


Figure 5.5: Simulated equilibrium configurations of a droplet sinking into a fluid substrate for different ratios of contact angles. In both images, the upper part belongs to the ambient fluid, the lower part to the fluid substrate. Parameters are $\eta_0 = \eta_1 = 1$ Pa \cdot s, $\rho_0 = \rho_1 = 1000$ kg/m³, $\sigma_0 = 30$ $\frac{\text{mN}}{\text{m}}$. Adapted from Aland/Mokbel [10].

equilibrium state at this time, the purely viscous substrate keeps deforming. The Laplace pressure pushes the droplet deeper and deeper into the substrate. As the substrate here is very thin, this dynamics would eventually lead to a breakup of the substrate phase in the center. This breakup

would cause the drop to touch the bottom boundary of the computational domain. Obviously, such a topological change is not correctly described by a grid-based numerical model. Here the simulations crash before the topological change due to degenerate mesh elements.

The observation of a fluid substrate also allows for a comparison of the equilibrium contact angle in the simulations with the Neumann’s triangle, cf. Sec. 2.3.3. Fig. 5.5 shows a reproduction of the results of three-phase flow simulations from [115, Fig.10], using the same relation of the surface tensions. Uniform values for viscosity and density are chosen throughout the whole domain here, namely $1 \text{ Pa} \cdot \text{s}$ and 1000 kg/m^3 . The initial droplet is described as a small spherical cap upon a planar fluid substrate. The obtained equilibrium shapes are displayed in Fig. 5.5.

The intersection between the fluid-fluid meniscus and the substrate shows good agreement of the developed equilibrium contact angle with [115, Fig.10]. In particular, Fig. 5.5(a) indicates that for $\sigma = \sigma_1 = \sigma_0$ the respective angles in all three phases are equal to each other ($\approx 120^\circ$). Also, the case $\sigma_1 : \sigma_0 : \sigma = 1 : 1.4 : 0.8$ shown in Fig. 5.5(b) yields the expected shape when compared with the reference.

5.4.4 Interaction between liquid droplets on viscoelastic substrates

After the validation studies for elastic and fluid substrates in the previous sections, the potential of the method is illustrated in the following. This involves the first numerical simulations of two experimentally observed soft wetting phenomena in Sections 5.4.4 and 5.4.5.

The first of these phenomena considers the substrate-mediated interaction of droplets. When placed sufficiently close, liquid drops on soft solid substrates are found to attract or repel each other, due to a combination of substrate elasticity and capillary forces [116]. This mechanism is also referred to as the inverted Cheerios effect. The present model is able to simulate such scenarios including the topological transition during fusion of drops.

The simulated scenario considers a 2D domain with two drops that are initially close to each other. Fig. 5.6 shows an exemplary series of snapshots to describe the dynamics in more detail. Here, a square domain Ω is set with length $150 \mu\text{m}$, divided in half by Ω_s and Ω_f . The two drops are placed symmetrically and centered so that they have an initial distance of $10.75 \mu\text{m}$. The drops are initially prescribed as half-spherical caps of $20 \mu\text{m}$ radius. Furthermore, $\epsilon = 2 \mu\text{m}$, which is significantly smaller than the distance between the drops, thus preventing the diffuse interfaces to “feel” each other. To strengthen the substrate-mediated interaction, a relatively soft substrate is assumed, namely $G = 200 \text{ Pa}$. The solid surface tensions are higher than the surface tension between drops and ambient, $\sigma_1 = \sigma_0 = 46 \frac{\text{mN}}{\text{m}}$, and $\sigma = 31 \frac{\text{mN}}{\text{m}}$. In the whole domain, viscosity and density are chosen to be constant, namely $1 \text{ Pa} \cdot \text{s}$ and $1000 \frac{\text{kg}}{\text{m}^3}$, respectively.

At the beginning there is a relatively rapid deformation of the substrate in vertical direction due to the capillary forces ($t = 160 \mu\text{s}$). This dynamics decays after $t = 3200 \mu\text{s}$ and the attraction force

between the droplets becomes dominant, moving the two drops in horizontal direction towards each other ($t = 44800 \mu\text{s}$), see also [116, Eq. 3]. After the two drops have merged ($t = 45760 \mu\text{s}$), the resulting single drop develops an almost stationary state, as indicated in the last snapshot.

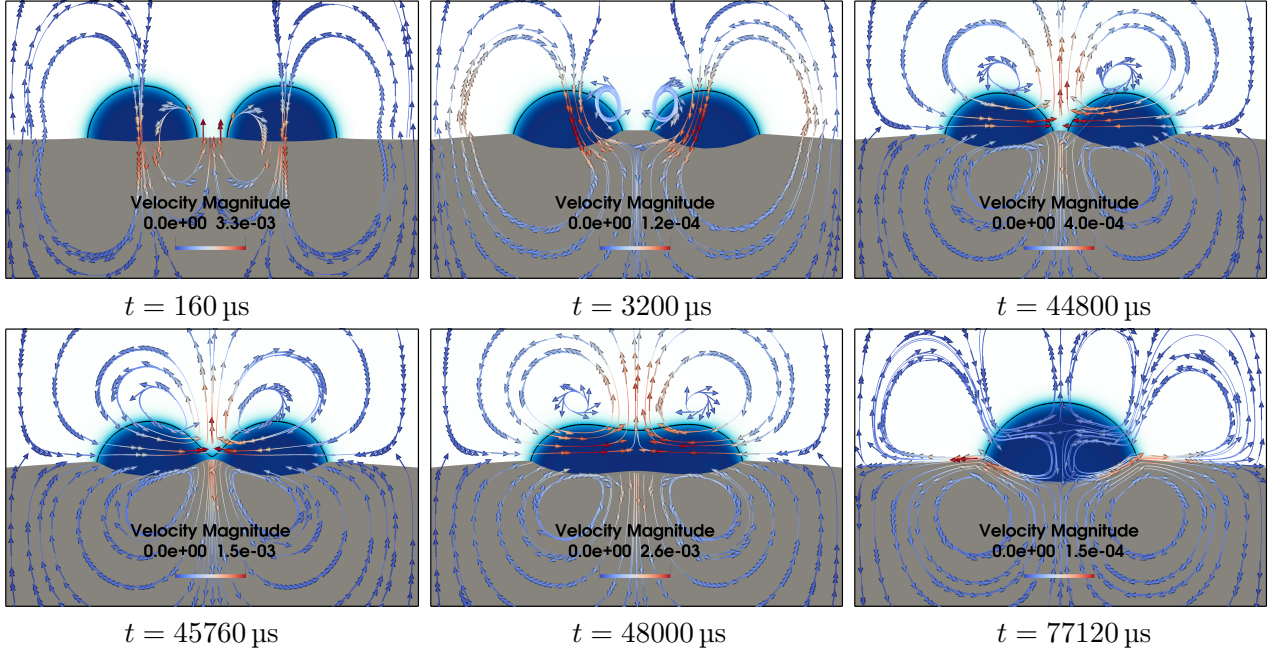


Figure 5.6: Simulation of the inverted Cheerios effect. The six snapshots are chosen such that essential aspects of the dynamic behavior can be recognized. The lower part of the images is Ω_s , the upper part is Ω_f . The coloring in Ω_f indicates the phase field values ($\phi = 1$ in blue, $\phi = 0$ in white). Streamlines are colored by velocity magnitude (in m/s). For better visibility, all snapshots show a section of Ω with $150 \mu\text{m} \times 100 \mu\text{m}$. Adapted from Aland/Mokbel [10].

5.4.5 Surfing on a viscoelastic substrate

Being able to describe viscoelastic substrates, the present model can simulate another interesting soft wetting phenomenon: the observed surfing behavior of liquid droplets. In [1], it was reported that a fluid-fluid interface on a viscoelastic substrate moves in front of the wetting ridge, which suggested the term “surfing on the ridge”. Different rheological models were considered analytically for this purpose [1], and provide a potential reference for results from numerical simulations. Fig. 5.7(a) shows an exemplary experimental setup from [1]. Water is injected into a hollow circular cylinder of viscoelastic material. While water is pushed in, ambient gas drains out and the fluid-fluid interface moves across the substrate, dragging the wetting ridge behind it.

To simulate this scenario, a cylinder is prescribed with 2 mm inner radius, 6 mm length and 2 mm

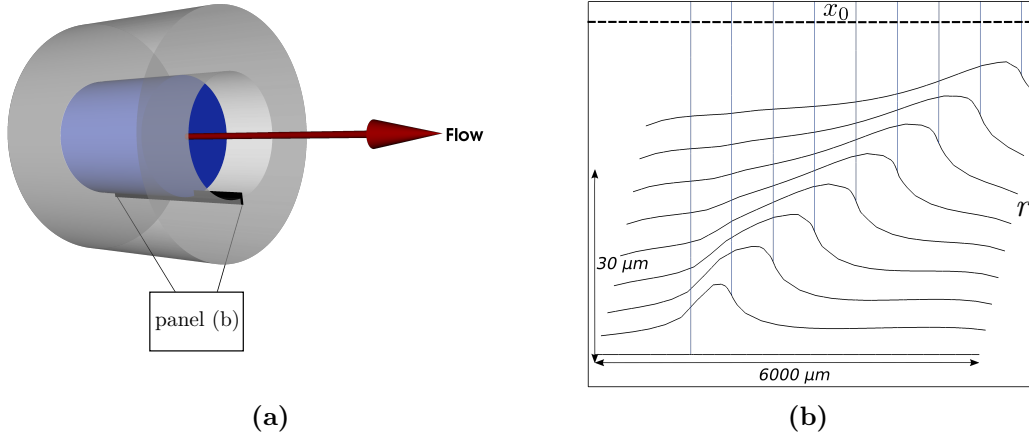


Figure 5.7: Simulation of a fluidic interface moving over a viscoelastic substrate. (a) The simulation setup, where the black rectangle represents the region of interest. (b) The evolution of the surface in the region of interest, indicated by 9 snapshots taken every 13.6 ms. The vertical blue lines represent the liquid-ambient interface and the black lines are the substrate profiles. The flow direction is from left to right, with the liquid on the left side of the liquid-ambient interface. The individual snapshots are each slightly shifted to enhance visibility. A scaling factor of 100 was applied in vertical direction to pronounce the surfing behavior. Adapted from Aland/Mokbel [10].

thickness. The parameters are motivated by the experiments in [1]:

$$\begin{aligned}
 \rho_{f,0} &= 1 \frac{\text{kg}}{\text{m}^3}, & \rho_{f,1} &= 1000 \frac{\text{kg}}{\text{m}^3}, & \rho_s &= 1000 \frac{\text{kg}}{\text{m}^3}, \\
 \eta_{f,0} &= 0.002 \text{ Pa} \cdot \text{s}, & \eta_{f,1} &= 0.002 \text{ Pa} \cdot \text{s}, & \eta_s &= 40 \text{ Pa} \cdot \text{s}, \\
 \sigma &= 72 \frac{\text{mN}}{\text{m}}, & \sigma_1 &= 38 \frac{\text{mN}}{\text{m}}, & \sigma_0 &= 38 \frac{\text{mN}}{\text{m}}, \\
 v_{Flow} &\approx 40 \frac{\text{mm}}{\text{s}}, & G &= 1000 \text{ Pa}, & \epsilon &= 38 \mu\text{m},
 \end{aligned}$$

where v_{Flow} denotes the average inflow velocity, which also determines the velocity of the fluid-ambient interface. Again, a higher viscosity of air is chosen to improve numerical robustness which barely perturbs numerical results. The injection of water is realized using the Dirichlet boundary condition of a parabolic velocity profile, see Sec. 5.5.2 below for details.

The evolution of the substrate profile around the contact line is shown in Fig. 5.7 (b). One can see in the initial stages that the fluid-ambient interface moves faster in the direction of flow than the peak of the wetting ridge. This behavior is caused by the substrate viscosity, which slows down the substrate dynamics significantly. Accordingly, the three-phase contact point is displaced from the peak of the wetting ridge. This gives rise to the “surfing” of the contact line along the front of the ridge.

The dynamics of the solid domain is further illustrated by velocity streamlines shown in Fig. 5.8 at two different times. Note that the horizontal and vertical axes are scaled equally here, which clarifies the actual flatness of the wetting ridge. It can be seen that two vortices appear in the early stage of

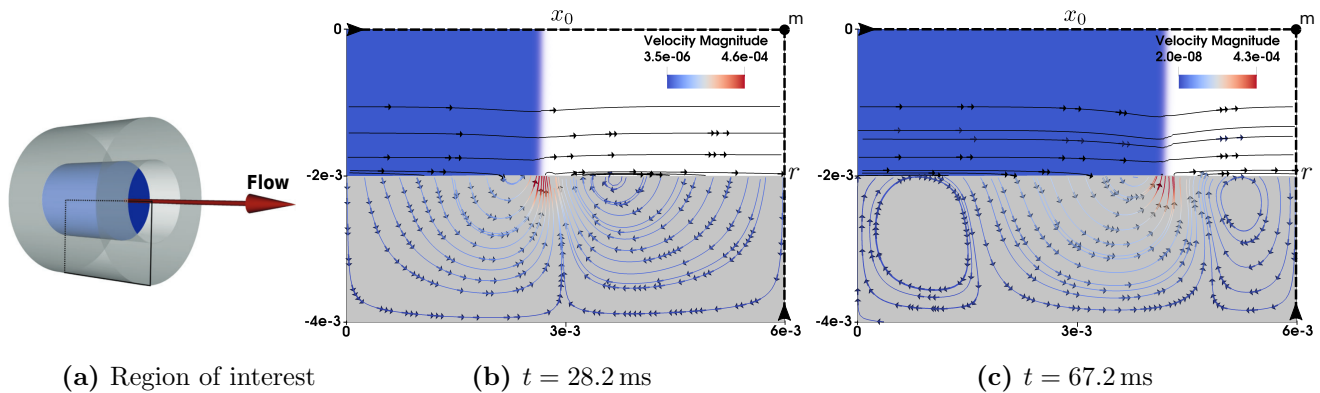


Figure 5.8: Illustration of flow velocity during surfing. (a) The region of interest is marked by a black rectangle. (b, c) Velocity streamlines in the region of interest referring to the simulation presented in Fig. 5.7, exemplary for two different times. The solid substrate Ω_s is in grey, the fluid ($\phi = 1$) in blue, and the ambient phase ($\phi = 0$) in white. Streamlines in Ω_s are colored by velocity magnitude (in m/s), while streamlines in Ω_f are black since the fluid velocity is about two orders of magnitude higher. Adapted from Aland/Mokbel [10].

surfing, complemented by a third vortex in a later stage of the surfing process.

The here developed numerical method is the first one able to simulate the surfing behavior and provides a framework to study visco-elasto-capillary dynamics beyond the limited theoretical study in [1]. Therefore, it can be used to increase the fundamental understanding of the dynamics of soft wetting with many potential applications, such as the patterning of cells[96] or droplets[97] onto soft surfaces, or the optimization of condensation processes[98], which is left for further studies.

With regard to the surfing behavior, however, it is intended to further investigate within this thesis. Of particular interest is the dependence of the behavior on the flow velocity. Simulations using the above numerical method revealed in certain velocity regimes the stick-slip phenomenon often observed experimentally (see e.g. [117]). In contrast, other velocity regimes showed a continuous motion of the contact line. The following section elaborates on this promising finding.

5.5 Stick-slip contact line motion on Kelvin-Voigt model substrates

This section covers the content published by the author in Mokbel et al. [11], where simulation results were compared with an analytical model [1]. The analytical results together with physical insights were kindly provided by Stefan Karpitschka. Background information on the analytical model is not discussed here.

The capillary traction of a liquid contact line causes highly localized deformations in soft solids, tremendously slowing down wetting and dewetting dynamics by viscoelastic braking. Enforcing nonetheless velocities in certain regimes leads to the so-called stick-slip instability, during which the contact line periodically depins from its own wetting ridge. The mechanism of this periodic motion and, especially,

the role of the dynamics in the fluid have remained elusive. This is partly because, to the author's knowledge, a theoretical description of the unsteady soft wetting problem is not available so far. This section presents the first numerical simulations of the full unsteady soft wetting problem, with a full coupling between the liquid and the solid dynamics.

Sec. 5.5.1 gives a brief outline of the state of the art. The model setup for the simulations is then shown in Sec. 5.5.2 and is a specification of the approach presented earlier in this chapter. This is followed by the validation of the numerical model in Sec. 5.5.3, using the analytical model [1]. Afterwards, the findings from the simulations are presented in Sec. 5.5.4. There, three regimes of soft wetting dynamics are observed: steady viscoelastic braking at slow speeds, stick-slip motion at intermediate speeds, and finally another region of viscoelastic braking at high speeds. In the latter region, stick-slip behavior is suppressed by liquid damping, which ultimately gives way to classical wetting dynamics dominated by liquid dissipation. This work is concluded by a brief discussion of the results in Sec. 5.5.5.

5.5.1 State of the art

The capillary interaction of liquids with soft solids is a ubiquitous situation in natural or technological settings [25, 118, 119, 120], see also Sec. 5.1. The capillary tractions, exerted by the liquid onto their soft support, cause strong deformations if the substrate is soft or the considered length scale is sufficiently small [113, 121]. The typical scale below which capillarity deforms solids is given by the elastocapillary length, $\ell = \sigma/G$, the ratio of surface tension σ and (static) shear modulus G , cf. Sec. 2.3.1. At three-phase contact lines, the length scale of the exerted traction lies in the molecular domain, deforming the solid into a sharp-tipped wetting ridge [122]. As a liquid spreads over a soft surface, the traction moves relative to the material points of the substrate. The necessary rearrangement of the solid deformation leads to strong viscoelastic dissipation which counteracts the motion, a phenomenon called viscoelastic braking, see e.g. [123, 1, 124]. At small speeds, the motion remains steady [123], whereas at large speeds, unsteady motion, frequently termed stick-slip, has been observed [117, 125, 1, 126, 127, 128]. In this mode, the contact line velocity and the apparent contact angle undergo strong, periodic oscillations. On paraffin gels, Kajiyama et al. [125] observed stick-slip motion only in an intermediate velocity range, returning to continuous motion if the speed was increased even further.

The origin of this stick-slip motion remains debated in literature. It is clear that the pinning and depinning is not associated with permanent surface features, but rather with the dynamics of the wetting ridge itself: the solid deformation cannot follow the fast contact line motion of the depinned (slip) phase of a stick-slip cycle [127, 128]. Unclear, however, are the conditions upon which a contact line may escape from its ridge, thus eliminating the viscoelastic braking force. The depinning of a contact line from a sharp-tipped feature on a surface is governed by the Gibbs inequality [129, 127]. Van Gorcum et al. [127] postulated a dynamical solid surface tension, which would alter the local force balance and thus allow the contact line to slide down the slope of the ridge. Still, the physico-chemical

origin of such dynamic solid surface tension remains elusive. Roche et al. [130] postulated the existence of a point force due to bulk viscoelasticity, but the shear-thinning nature of typical soft polymeric materials would prevent such a singularity at the strain rates encountered in soft wetting [131, 128]. Unclear as well is the role of the fluid phase during the cyclic motion, mainly because a comprehensive multi-physics model for the unsteady soft wetting problem is not available to date.

This section presents the first fully unsteady numerical simulations of dynamical soft wetting, fully accounting for liquid and solid mechanics, and for the capillarity of the interfaces, by which the life cycle of stick-slip motion is revealed. Phase diagrams of steady and unsteady contact line motion are derived by tuning parameters over large ranges, recovering stick-slip behavior at intermediate speeds. At small and large speeds, steady motion appears that quantitatively agrees with the analytical model.

It should be noted that very recently, after the publication of Mokbel et al. [11], experimental studies [132] of moving contact lines in water mixtures on soft polymer substrates (polydimethylsiloxane, or PDMS for short) underpinned the observations that follow here with quite similar conclusions. However, in contrast to the Stokes flow assumption made here, inertial forces in the liquid were also considered in the experimental studies. It is important to emphasize here that a minimal model is deliberately assumed for the present numerical simulations to keep the physics conceivable, even though it is possible to extend the physics (e.g. to add inertial forces). This assumption reduces the complexity of the stick-slip study to the key influencing factors and is essential for a basic understanding. The present model specifications are described in more detail in the following section.

5.5.2 Setup and contact line motion

Computational domain and material parameters

Figure 5.9(a) shows the geometric setup of the numerical simulations. A hollow cylinder (undeformed inner radius R), made of a soft viscoelastic material (gray, thickness $h_s \ll R$), with a fixed (rigid) outer surface, is partially filled with a liquid (blue) and an ambient fluid phase (transparent). In the following numerical simulations, the values are chosen as $R = 2$ mm and $h_s = 1$ mm. The length of the cylinder is 6 mm. This cylindrical structure allows for the use of rotational symmetry and thus the simulation of a 3D scenario in a 2D computational domain (see Sec. 3.5). Consequently, the computational complexity significantly reduces compared to non-symmetrical 3D setups. The two-phase fluid is implemented by the phase field approach with the finite liquid-ambient interface thickness $\epsilon = 4.75 \mu\text{m} \ll h_s$, and the capillary traction of the meniscus onto the solid is distributed over this characteristic width. The solid is modeled with a sharp interface towards the fluid.

As mentioned above, the physics should be kept conceivable, which is ensured by the following minimal model specifications. The focus is on the evolution of the contact line, which should not depend on a gradient of the fluid viscosity. Therefore, a constant fluid viscosity $\eta_f = 1$ mPa·s is assumed here in both the liquid and ambient phases. Nevertheless, the terms “liquid” and “ambient” are retained

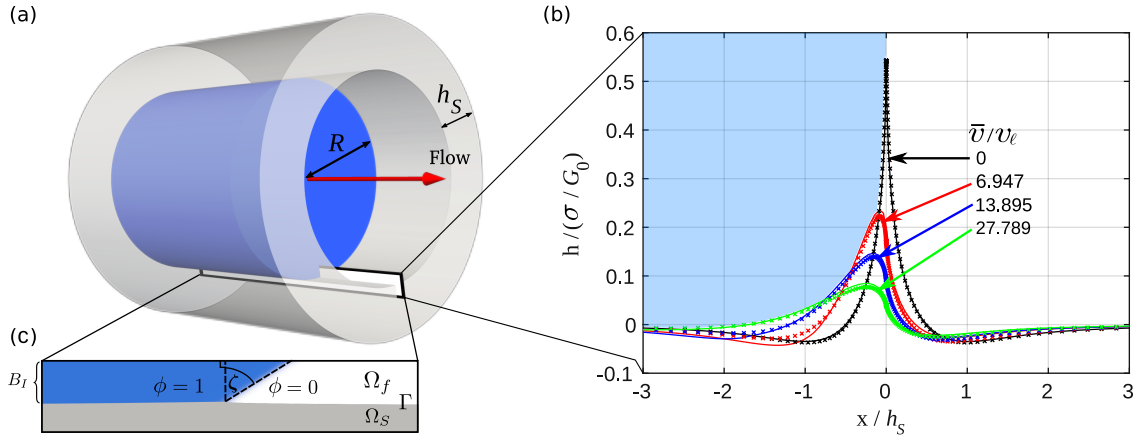


Figure 5.9: (a) Dynamical wetting of a cylindrical cavity (radius R) with a soft viscoelastic wall (grey, thickness h_s) by a two-phase fluid (blue and transparent). The fluid-fluid interface is represented by the transition region of the phase field, with negligible interface width $\epsilon = 0.00475 h_s$. The contact line speed is controlled by the flux boundary condition Eq. (5.17) on the rear end of the cavity. (b) Quasi-stationary wetting ridge on the cavity wall for different (constant) velocities, comparison between FEM simulations (symbols) and the analytical model (lines). The liquid interface is aligned at $x = 0$, while the left blue region indicates the advancing liquid phase. Moving ridges correspond to large velocities beyond the stick-slip regime. Note that for non-zero velocities the maximum height is located well behind the contact line. The rounded shapes are bumps generated by strong solid dissipation, as opposed to the sharp kink imposed at the contact line for $\bar{v} = 0$. (c) Inset containing the definition of the fluid-fluid interface rotation ζ relative to the initial situation in which the interface is perpendicular to the wall surface. Adapted from Mokbel et al. [11].

in the following. Furthermore, inertia is neglected by setting the density $\rho_f = 0 \text{ kg/m}^3$ everywhere, which reduces Eq. (5.1)₁ to the Stokes limit. Constant and equal surface tensions $\sigma = \sigma_s$ apply at all interfaces (liquid-ambient, solid-liquid, and solid-ambient).

According to Sec. 5.2.2, the cylinder casing itself is modeled as an incompressible Kelvin-Voigt material. A viscoelastic Kelvin-Voigt material is generally also characterized by a frequency-dependent complex modulus $G^* = G_0 + i\eta_s\omega$, with static shear modulus G_0 and effective substrate viscosity η_s . Note consequently that from here on the notation G_0 replaces the previous G . Further parameters that will be of interest here are the elastocapillary length $\ell = \sigma/G_0 \ll h_s$, a characteristic time scale $\tau = \eta_s/G_0$, and an elastocapillary velocity $v_\ell = \ell/\tau = \sigma/\eta_s$. The material parameters are listed in Table 5.1. Importantly, since $\epsilon \ll \ell$, the present analytical and numerical results do not significantly depend on the actual value of ϵ (cf. Sec. 2.3).

The inner surface of the soft viscoelastic cylinder wall is deformed into a wetting ridge due to the capillary action of the liquid meniscus. This can be seen in Fig. 5.9(b), in particular at the profile line with zero velocity. The case of non-zero velocities is explained further below.

The present simulation results for the solid deformation are compared to [1], where the authors pre-

symbol	value	meaning
η_f	1 mPa · s	fluid viscosity
σ	38 mN/m	fluid surface tension
σ_s	38 mN/m	solid surface tension
G_0	1 kPa	static shear modulus
η_s	3 Pa · s	substrate viscosity
h_s	1 mm	substrate thickness
R	2 mm	cylindrical cavity radius
ϵ	4.75 μ m	interface thickness
ℓ	38 μ m	elastocapillary length
$\alpha_s = \frac{\sigma_s}{G_0 h_s}$	0.038	elastocapillary number
$v_\ell = \sigma_s / \eta_s$	0.0126 m/s	elastocapillary velocity

Table 5.1: Material parameters. Adapted from Mokbel et al. [11].

sented an analytical plane-strain model. Since $h_s \ll R$ here, the substrate deformation is well approximated by plane-strain conditions.

It should also be noted here that the numerical grid size is about 5% of the elastocapillary length at the liquid-ambient interface, and typically about 20% outside of the interface region.

Contact line motion

As indicated in Fig. 5.9(a) the simulations consider the inflow of the liquid phase into the hollow space of the cylinder. Therefore the liquid-ambient interface is initially placed 1 mm away from the inflow boundary B_I . At the inflow boundary, a parabolic flow profile is used to establish a condition for the velocity $\mathbf{v}_f = (v_0, v_r)$ with components v_0 in the flow (axial) direction and v_r in the radial direction. It reads

$$\mathbf{v}_f = (V(R^2 - r^2), 0)^T \quad \text{on } B_I, \quad (5.17)$$

where r is the position in radial direction ($r = 0$ at the axis of symmetry) and V is a factor which controls the (mean) liquid-ambient interface velocity \bar{v} . The latter can be calculated by

$$\bar{v} = \frac{\int_{\Omega_f} v_0 r \, d\Omega_f}{\int_{\Omega_f} r \, d\Omega_f}. \quad (5.18)$$

The liquid meniscus is forced to move by imposing the boundary condition Eq. (5.17) on the inflow boundary B_I , but can freely change its shape (curvature) in response to the fluid flow. In contrast to the analytical model from [1], the instantaneous contact line velocity (here: v_c) is not imposed, but rather its long-term mean \bar{v} as stated in Eq. (5.18). Although \bar{v} is a time-dependent quantity, the simulations show a nearly constant value with negligible deviations even for unsteady contact line

motion. This constant velocity, approximated in the simulations by \bar{v} , is the analytically expected mean velocity for laminar flow in a pipe, $VR^2/2$ (see e.g. [133]). In this section, \bar{v} refers to this approximative value of the mean velocity.

Furthermore, $\mathbf{v}_s=0$ applies at the outer surface of the cylinder, $\delta\Omega_s\setminus\Gamma$, and $v_r = 0$ applies on $\delta\Omega_f\setminus\Gamma$, i.e. there is no radial flow along the inflow and outflow boundary and on the symmetry axis. Note that $B_I \subset \delta\Omega_f$ and that the inset in Fig. 5.9(c) only shows a section of the rectangular computational domain in the vicinity of the contact line. In particular, the height of the actual domain $\Omega_f \cup \Omega_s$ is $R + h_s$ and the axis of symmetry is part of $\delta\Omega_f$.

All simulations are started at $t = 0$ with a flat substrate, a flat meniscus, and the imposed velocity at the inflow boundary (Eq. (5.17)), and run until a steady state or limit cycle has been reached. Fig. 5.9(b) compares the (sharp) stationary profiles of the simulated solid substrate for several imposed velocities with the analytical model, with excellent agreement. Simulation results are represented there by markers and analytical results by solid lines. The scaled profile height $h/(\sigma/G_0)$ is used, together with the scaled position x/h_s and the scaled velocity \bar{v}/v_ℓ , which nondimensionalizes the occurring physical quantities. Note that this comparison is only possible as steady ridge shapes are observed for the chosen velocities. A static ridge ($\bar{v} = 0$) and very fast ridges ($\bar{v}/v_\ell > 6$) are chosen, where in the latter case the shapes are significantly different from the static case. One important feature of fast ridges is the emergence of a dissipative “bump”, well behind the contact line (see Fig. 5.10(a) for details about the ridge geometry). In an intermediate velocity range, unsteady cyclic shape dynamics emerge (stick-slip) that cannot be grasped by the analytical model.

Moreover, an important comparative quantity is the liquid-ambient interface rotation angle ζ at the contact line, which can be defined in multiple ways. Here ζ is measured as indicated in the inset in Fig. 5.9(c). In the initial state this angle is zero as the liquid-ambient interface is perpendicular to the solid surface. As the interface evolves, it curves accordingly. Automated angle measurement is performed in a thin domain $A \subset \Omega_f$ in the direct vicinity of the contact line. The dimensions of A are chosen to be negligibly small compared to the radius of curvature of the liquid-ambient interface. The rotation angle ζ is then calculated via a phase-dependent averaged normal

$$\mathbf{n}_a = \frac{\int_A \nabla\phi \, dA}{\int_A |\nabla\phi| \, dA}$$

which points towards the liquid phase. Consequently, the rotation angle is calculated by

$$\zeta = \frac{\pi}{2} - \arccos(\mathbf{n}_a \cdot \mathbf{t} / |\mathbf{n}_a|),$$

where $\mathbf{t} = (t_0, t_r)$ denotes the tangent at the initial liquid-ambient interface, which is chosen here as a unit vector in radial direction, i.e. $t_0 = 0$, $t_r = 1$. Note that $-\frac{\pi}{2} \leq \zeta \leq \frac{\pi}{2}$ is assumed here, while for the present simulations only cases with a positive rotation angle are considered.

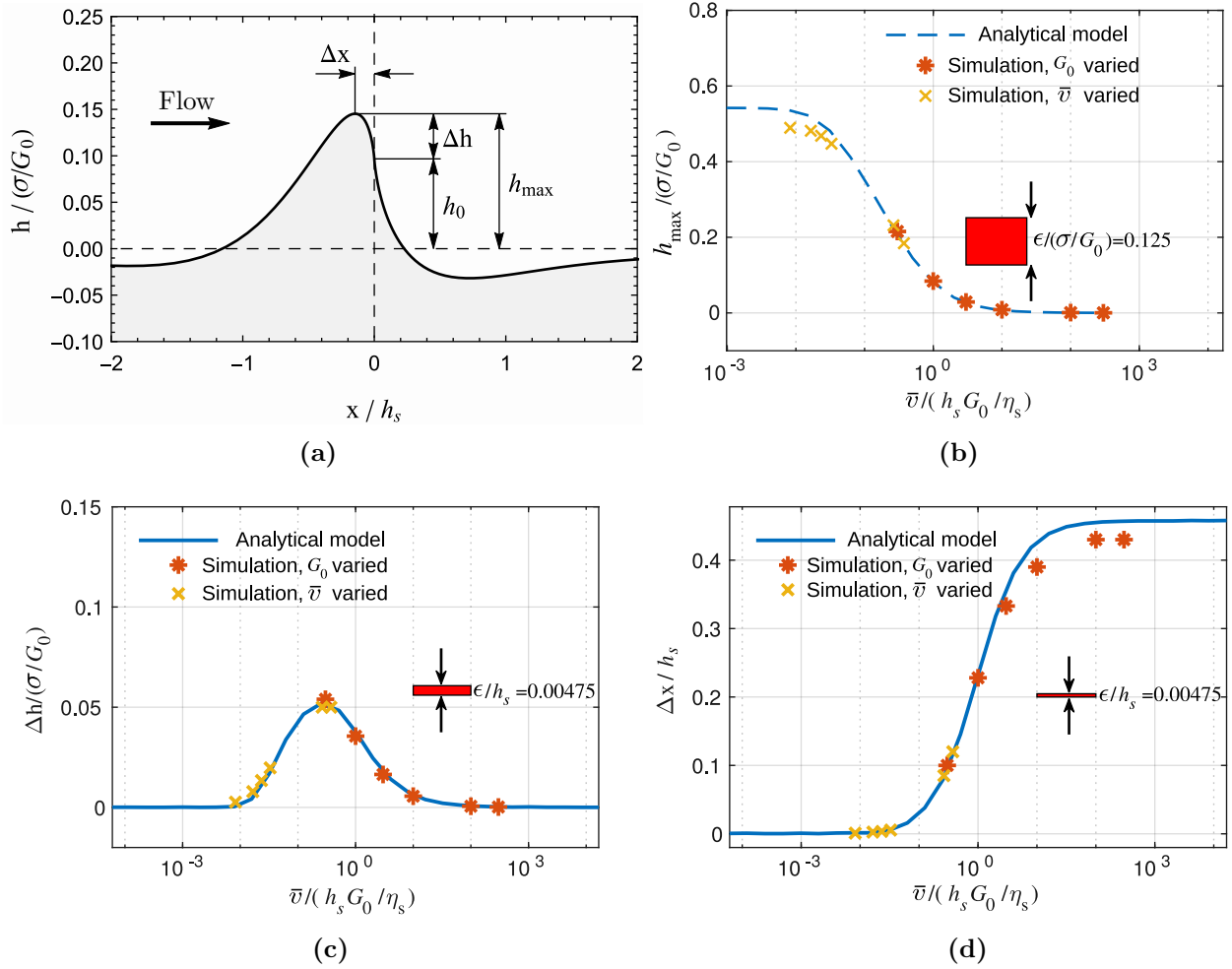


Figure 5.10: Model validation via comparison of simulation results to the analytical model. (a) Characteristic dimensions of a moving wetting ridge. The highest point of the ridge is not located at the contact line, but is located Δx behind and Δh above the contact line, due to strong dissipation in the solid. Both h_0 and h_{max} decrease with velocity, due to dissipation. (b) h_{max} as a function of the imposed (scaled) velocity, comparison between the analytical model (dashed line) and the simulations (markers). The gap at intermediate velocities is the stick-slip region, where a comparison between the unsteady simulation results and the analytical model becomes impossible. (c) and (d) Δh and Δx as functions of the imposed (scaled) velocity, comparing the analytical model (solid line) to simulation results (markers). Note that in the simulations the large magnitudes of the scaled velocity (right subregions in (b)-(d)) are represented by varying G_0 values instead of using large \bar{v} values for stability reasons. Adapted from Figures S2 and S3 in Mokbel et al. [11].

5.5.3 Validation by an analytical model

A further validation of the substrate deformations obtained in the numerical simulations is carried out here by a direct comparison with the analytical model [1]. Note that a first validation step has already

been presented in Fig. 5.9(b), comparing stationary substrate shapes for several velocities. As a next step, Fig. 5.10(a) shows the characteristic, velocity-dependent dimensions of the wetting ridge. The subfigure (b) compares the simulated maximum ridge height, h_{max} , to the analytical model, finding an excellent agreement, both for small and large (nondimensionalized) velocities where the contact line moves at constant velocity. In an intermediate (stick-slip) regime, the ridge shapes change drastically in an oscillating manner, ruling out a direct comparison between the models. This is indicated by the gap in numerical data points at intermediate velocities $\approx 10^{-1}$ and is discussed in more detail in the following section.

Due to the strong dissipation in a Kelvin-Voigt solid, which is regularized by the finite width of the capillary traction (controlled by the interface thickness ϵ of the phase field), the maximum ridge height is not located at the contact line, but behind it. The distance between the contact line and the peak of the ridge, in vertical and in horizontal direction, is plotted in Fig. 5.10(c) and (d). Δh shows a pronounced maximum at the elastocapillary velocity. Δx increases monotonically and saturates at large speeds. Also these ridge properties reveal an excellent agreement between the two models.

5.5.4 Results

Modes of contact line motion

The dynamics of the contact line motion can be characterized by the time-dependent contact line velocity $v_c(t)$ and rotation $\zeta(t)$ of the liquid-ambient interface at the triple line (cf. Fig. 5.9(c)), where the rotation angle is the main focus in the following. The three characteristic regimes revealed by the simulations are now examined, corresponding to a small, intermediate, and large mean velocity \bar{v} . Due to the large differences in \bar{v} , the dynamics are best compared by plotting ζ as a function of contact line position, see Fig. 5.11(a). Subfigures (b) and (c) show further perspectives illustrating the three modes of contact line motion. At small velocity ($\bar{v} \lesssim v_\ell$, blue), after some initial transient the contact line moves steadily with a constant speed and a constant dynamic contact angle. Here, the relation between contact line velocity $v_c(t)$ and rotation ζ is permanently dominated by viscoelastic braking [123, 1]. Once the forcing velocity exceeds a critical value, the motion becomes unsteady, finding a limit cycle after an initial transient (red): the liquid interface rotation ζ shows large oscillations, of peak-to-peak amplitude $\Delta\zeta$ on the order of the mean rotation $\bar{\zeta}$, with a non-trivial waveform, as the contact line advances at an oscillatory velocity $v_c(t)$ (see Fig. 5.11(d)). This behavior is not captured by the simple analytical model. For larger velocities (yellow), v_c and ζ are constant again after an initial transient. Note here that the motion in this regime is very sensitive to discretization artifacts and requires rather fine grid resolutions to give consistent results. Movies illustrating contact line motion and substrate dynamics for the three modes can be found online in the supplementary material of [11].

Fig. 5.11(d) shows a phase portrait of the contact line motion in terms of the physically relevant variables ζ and v_c . For slow forcing velocities (blue), a continuous, steady contact line motion is

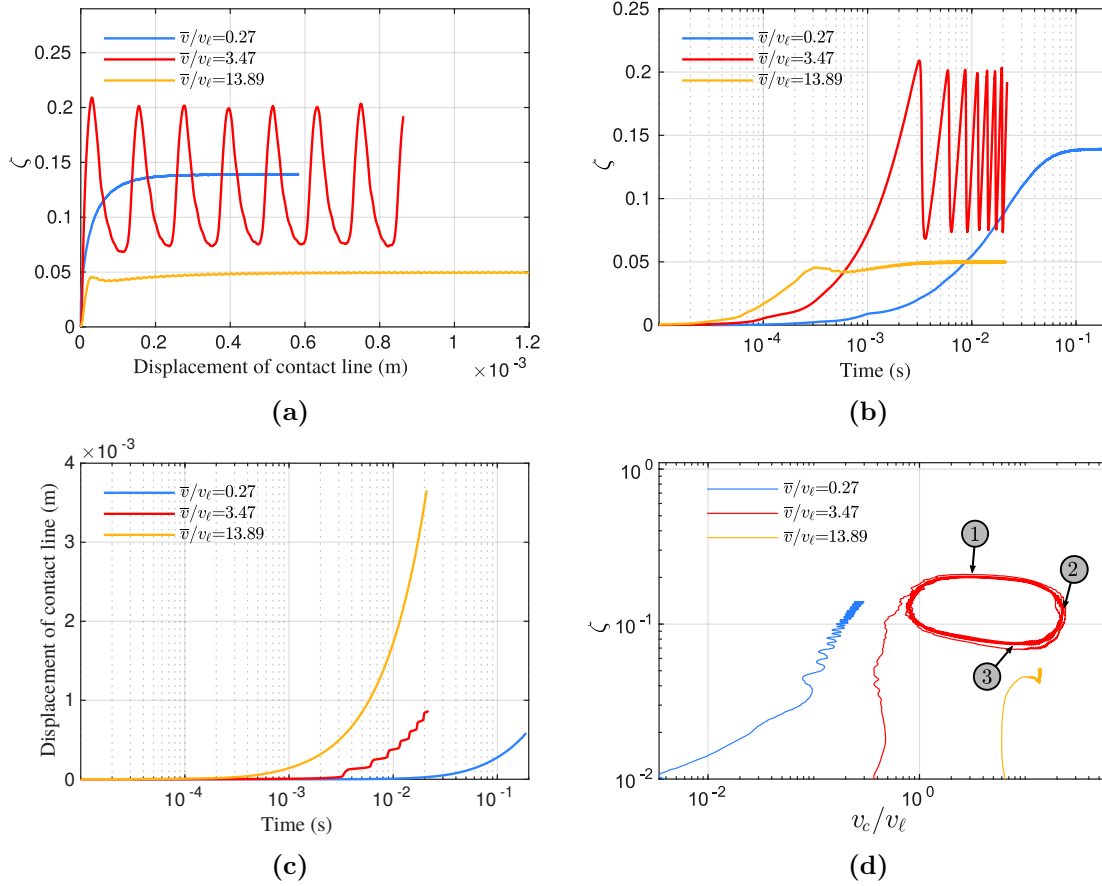


Figure 5.11: Illustration of the three characteristic modes of contact line motion from different perspectives. **(a)** Rotation ζ of the liquid-ambient interface at the contact line, as a function of the contact line position, for different imposed mean velocities. Slow and fast speeds show a continuous motion (blue and yellow, respectively). For intermediate velocities (red) we observe a strong stick-slip behavior, in which the liquid angle oscillates with an amplitude that is comparable to its mean. The residual waviness of the yellow curve is not an actual non-stationary motion but can be traced back to grid artifacts. **(b)** Rotation ζ of the liquid-ambient interface as a function of time. **(c)** Contact line displacement as a function of time. In (b) and (c), the logarithmic scaling of the abscissae was chosen for convenience, to allow a simultaneous display of early and late times for slow and fast contact lines. **(d)** Phase portraits for contact line motion, showing the rotation angle ζ as a function of the (scaled) contact line velocity v_c . Blue: stable, stationary-motion regime. After an initial transient, the contact line finds a stationary constant value in the v_c - ζ -plane. Discretization artifacts are visible for small speeds (mind the logarithmic scale). Red: stick-slip motion, characterized by a large limit cycle in the v_c - ζ -plane. Yellow: at large speeds, stick-slip motion is suppressed, finding a stationary point in the v_c - ζ -plane again. Adapted from Figures 2, 3 and S4 in Mokbel et al. [11].

observed, up to the scale of grid artifacts (mind the logarithmic scales). Intermediate forcing velocities (red) lead to limit-cycles: As the liquid rotation exceeds a well-defined maximum (① in Fig. 5.11(d)), the contact line accelerates. In this phase, it surfs down its own wetting ridge, releasing energy

stored in the meniscus curvature, rate-limited partly by liquid dissipation (② in Fig. 5.11(d)). Then it decelerates and a new wetting ridge starts to grow, opposing the contact line motion further (③ in Fig. 5.11(d)) until the next cycle starts. For larger forcing velocities, the region covered by the limit cycle decreases until it virtually vanishes (yellow), up to grid artifacts. This is caused by the growing importance of liquid dissipation, which effectively limits, and finally prevents, the large-velocity excursions during the slip phases.

Regimes of contact line motion

The contact line motion can be characterized by ζ_{max} (① in Fig. 5.11(d)), ζ_{min} (③ in Fig. 5.11(d)), and $\bar{\zeta}$, the maximum, minimum, and mean values of ζ , respectively, in the stationary/limit cycle regime. Figure 5.12 shows these values as a function of the imposed (long-term mean) \bar{v} . For small velocities, the contact line actually moves with \bar{v} , and the simulated ζ (symbols) coincides with the result of the analytical model (black line), indicating the stability of steady contact line motion.

The onset of stick-slip motion (gray region) aligns with the maximum of ζ observed in the analytical model where the constant contact line velocity v_c is imposed instead of \bar{v} . This was stipulated in [1] since the rotation ζ is a measure for the dissipative (viscoelastic braking) force: A dissipative force that decreases with speed causes acceleration, and thus an unstable motion. The maximum braking force is observed at $\bar{v} \sim v_\ell = \sigma_s / (G_0 \tau) = \sigma_s / \eta_s$, the elastocapillary velocity: The finite width of the traction distribution regularizes the dissipation singularity at the scale $\epsilon \ll \ell \ll h_s$. Thus the largest characteristic frequency $\omega \sim \bar{v} / \epsilon$ dominates the dissipation associated with the contact line motion. One may evaluate the complex modulus at the dominant frequency to define a dynamical elastocapillary length $\ell_{\bar{v}} \sim \sigma_s / |G^*(\bar{v}/\epsilon)|$ [127]. Near the maximum braking force, $G''(\bar{v}/\epsilon) = \eta_s \bar{v} / \epsilon \gg G_0$, and the approximation $|G^*| \approx \eta_s \bar{v} / \epsilon$ yields $\ell_{\bar{v}} = \sigma_s \epsilon / (\eta_s \bar{v})$. Resonance is expected at $\epsilon \sim \ell_{\bar{v}}$ i.e., $\bar{v} \sim \sigma_s / \eta_s = v_\ell$, independent of the choice of ϵ , which is confirmed in the analytical model (see supplementary material in [11]).

ζ_{max} remains approximately constant upon entering the stick-slip regime, indicating a well-defined upper limit of the viscoelastic braking force also in unsteady situations (cf. location ① in Fig. 5.11(d)). However, this force periodically drops to much smaller values, as indicated by the much smaller values of ζ_{min} . In these *surfing* phases (② in Fig. 5.11(d)), liquid dissipation and the finite capillary energy stored in the curved meniscus are the rate-limiting factors.

As the imposed \bar{v} is increased further, the amplitude of the oscillation $\Delta\zeta$ shrinks, reaching virtually zero (indicated by the fading gray region). In this regime, the reduced viscoelastic braking force (ζ_{max}) limits the build-up of capillary energy in the meniscus, while liquid dissipation prevents its fast release. This balance between capillarity and liquid dissipation can be quantified by the capillary number $\text{Ca} = \bar{v} \eta_f / \sigma = (\sigma_s / \sigma) (\eta_f / \eta_s) (\bar{v} / v_\ell)$. If Ca exceeds a certain critical value Ca_c , the oscillatory motion is effectively damped out by liquid dissipation. Ca_c depends on the solid parameters, most

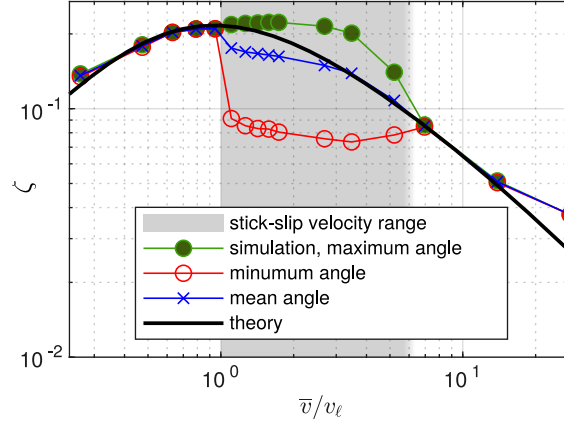


Figure 5.12: Rotation ζ of the liquid-ambient interface, as a function of the imposed mean velocity \bar{v} . In the gray region, the contact line motion is unsteady (stick-slip) in the simulations. The solid black line depicts the analytical calculation of the ridge tip rotation, for an imposed constant contact line velocity. Markers depict the maximum (green solid discs), mean (blue crosses), and minimum (red open discs) angle observed in the simulations. The onset of unsteady motion correlates with the maximum in ridge rotation. At large speeds, the amplitude of the angle oscillations decreases and the motion becomes stationary again until, finally, liquid dissipation becomes relevant. Adapted from Mokbel et al. [11].

notably the ratio σ/σ_s which sets the scale of ζ . Further, decay and growth rates of abandoned and new ridges during the stick-slip cycle matter, and thus some dependence on η_s can also be expected. For $\text{Ca} \gtrsim \text{Ca}_c$, the overall motion is still governed by viscoelastic braking: $\bar{\zeta} \sim \bar{v}^{-1}$ closely follows the result from the analytical model. The increased mean liquid rotation for the largest velocity $\sim 28v_\ell$, relative to the prediction of the analytical model, is another consequence of liquid dissipation. This can be rationalized by a comparison with the Cox-Voinov law for moving contact lines on rigid surfaces which predicts, for $\text{Ca} \sim 10^{-2}$, rotations of this order of magnitude [134, 135, 136]. In this hydrodynamic regime, one returns to the classical wetting physics on rigid surfaces.

Figure 5.13 summarizes the dynamical wetting behavior in terms of these three modes, as a function of the imposed mean velocity and the solid parameters. Steady small-velocity, stick-slip, and steady high-velocity modes are indicated by blue, red, and yellow symbols, respectively. On panel (a), the vertical axis shows varying solid and liquid surface tensions and thus a varying elastocapillary number $\alpha_s = \ell/h_s$, while keeping the Neumann angles of static wetting constant (cf. Fig. 2.4). Since G_0 and h_s merely enter α_s , they are not varied separately but their effect can be extracted from Fig. 5.13 (a). The onset of stick-slip is located near $\bar{v} = v_\ell$, given by the maximum of ζ vs. \bar{v} . This maximum is independent of α_s , up to a small correction that itself vanishes for $\epsilon/\ell \rightarrow 0$, as can be shown by the analytical model (see Fig. 1 of the supplementary material in [11]). Since ϵ is kept constant and ℓ is varied here, the onset of stick-slip motion is expected to depend slightly on ℓ (or $\sigma = \sigma_s$, respectively), as observed in Fig. 5.13(a). In physical units, however, the onset of stick-slip is inversely

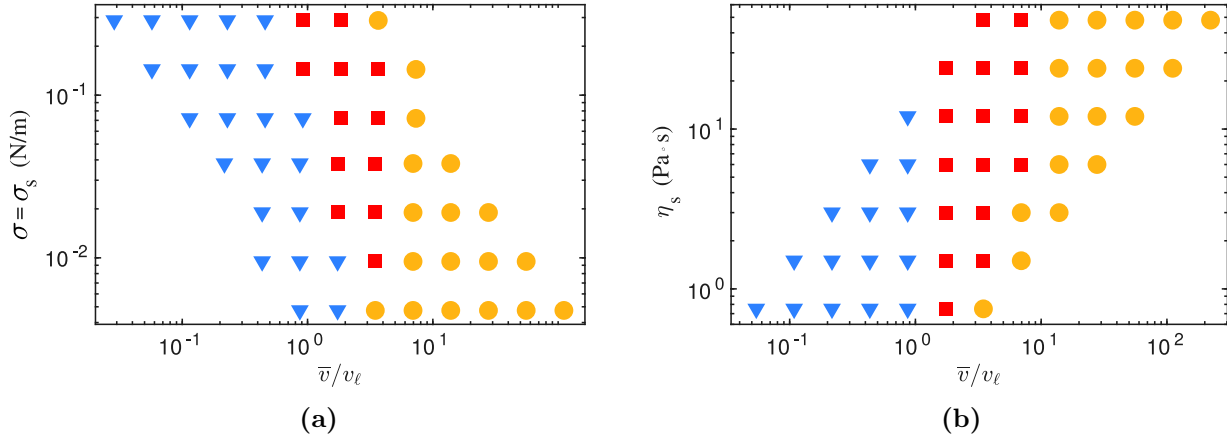


Figure 5.13: Phase diagrams for stick-slip behavior depending on the contact line velocity. Blue triangles: steady contact line motion; red squares: stick-slip; yellow circles: high-speed continuous motion. (a) Tuning the magnitude of capillary forces $\sigma = \sigma_s$ on the vertical axis. (b) Varying the substrate viscosity η_s on the vertical axis. Adapted from Mokbel et al. [11].

proportional to σ_s since $v_\ell \sim \sigma_s$. The transition to the fast continuous mode is, in scaled units, nearly independent of the surface tension. This can be rationalized again by a critical capillary number: Since σ and σ_s are tuned simultaneously, the scale of $\zeta \sim \sigma/\sigma_s$ [1] remains constant, and neither Ca_c , nor $\text{Ca} \sim (\sigma_s/\sigma)(\bar{v}/v_\ell)$ changes along the vertical axis. The stick-slip mode disappears at very low $\sigma = \sigma_s$, where $\ell \sim \epsilon$.

Similarly, the solid viscosity η_s (panel (b)) has no measurable impact on the critical \bar{v}/v_ℓ for the transition to stick-slip since the maximum ζ , which governs this transition, is independent of η_s . Still, the physical critical velocity is proportional to η_s since $v_\ell \sim \eta_s^{-1}$. The transition to the fast continuous mode behaves differently. $\text{Ca} \sim (\eta/\eta_s)(\bar{v}/v_\ell)$ increases with decreasing η_s , and the damping effect of liquid dissipation becomes noticeable already at smaller \bar{v}/v_ℓ . Thus the transition back to steady motion occurs earlier, such that the stick-slip region ultimately disappears at very low η_s . In any case, at very large velocities, liquid dissipation will take over, leading to wetting dynamics equivalent to those on rigid surfaces.

5.5.5 Discussion

This stick-slip study provides a comprehensive numerical analysis of dynamical soft wetting, including the physics of all relevant elements, the liquid, the solid, and the interfaces. The minimum required level of complexity is assumed in each element to keep physics intact and conceivable: the Stokes limit for the fluid along with a uniform fluid viscosity, a Kelvin-Voigt constitutive relation for the soft solid, regularized at a constant scale $\epsilon \ll \ell$, and constant and equal surface tensions on all three interfaces. This simple model already requires a complex, strongly coupled multi-physics modeling approach, and

exhibits rich behaviors.

The numerical experiments performed cover a wide range of system parameters and reveal three regimes in which the dominant physical mechanisms differ: (i) a slow regime, in which the contact line motion is entirely dominated by the dissipation in the solid. This regime is observed as long as the viscoelastic braking force increases with velocity. (ii) an intermediate regime, in which the dominant rate-limiting mechanism periodically switches from solid to liquid dissipation. This regime starts where the viscoelastic braking force exhibits a maximum with respect to the imposed (mean) velocity. This maximum is caused by a resonance effect, due to the regularization of a singular dissipation at some finite (constant) length scale. Other mechanisms, like dynamic solid surface tensions (surface constitutive relations [137, 138, 127, 139, 140, 141]) or a constitutive relation that exhibits resonance (e.g., standard linear solid [1]) would lead to the same phenomenology. (iii) a large- \bar{v} -regime with continuous motion, yet governed by viscoelastic braking, in which liquid dissipation prevents strong oscillations of the meniscus. This regime, and especially the transition into it, is based on a strong coupling between solid and fluid physics. To the best knowledge of the authors of Mokbel et. al. [11], this regime had been reported in only a single experimental work [125]. Another experimental work carried out later provides complementary insights into different velocity regimes in unsteady soft wetting [132]. Since the viscoelastic braking force, in contrast to liquid dissipation, does not increase with velocity, liquid dissipation ultimately dominates the contact line motion in the large- \bar{v} -regime, and one recovers the wetting physics of rigid surfaces.

This first comprehensive overview of soft wetting physics scenarios provides a strong basis for interpreting different phenomenology observed in experiments, ranging from paraffins [125] over microelectronic sealants [127, 113] to biology [142, 143, 144] and motivate experiments on the so-far little explored transition to continuous motion beyond stick-slip.

5.6 Conclusions

Soft wetting is an emerging young field of research with many potential applications (e.g. [96, 97, 98]) and a richness of not fully understood physical phenomena (e.g., durotaxis[97], Shuttleworth effect[145]) which demand for numerical simulation tools. The work presented in this chapter and in [10] has contributed a novel method which differs from previous methods in exploiting some characteristic properties of soft wetting. The result is a certain simplicity of the model (a unified approach for fluid and solid equations) and of the numerical discretization (no mappings, no subiterations, no non-linear solvers needed). It has been shown that the method is highly accurate and more robust than previous methods based on explicit coupling of the involved subproblems. At least up to [10] it was only surpassed by the fully monolithic method presented in [31].

As special features, the method includes exact incompressibility and a linear monolithic assembly of the Navier-Stokes and Cahn-Hilliard equations which stabilizes dominant surface tension at small interface

lengths [48]. Solid viscosity is included and it has been illustrated that solid material properties can be continuously tuned from purely viscous (i.e. three-phase fluid flow) to purely elastic. The surfing behavior of droplets on viscoelastic substrates has been reproduced for the first time. Moreover, a more advanced numerical study of stick-slip contact line motion on a viscoelastic substrate was performed using this method, which also explains the transitions to continuous motion, and which takes into account the physics of all components involved (liquid, ambient, solid). The robustness and flexibility of the method will permit detailed investigations of many further soft wetting phenomena in the future.

Chapter 6

Conclusions and outlook

In this thesis, two different approaches have been developed for modeling and simulation of ternary fluid-structure interaction (FSI) problems with incompressible viscoelastic structures. All these approaches are based on a phase field model for two-phase flows. The corresponding models are solved numerically using an adaptive finite element method.

The first approach considers the interaction between two structures and a fluid. One structure is modeled as a deformable viscoelastic solid, the other as a rigid body. The fluid, together with the viscoelastic solid, is represented by a phase field using a novel extended version of the basic phase field model capable of simulating two-phase FSI. The equations for mass and momentum are solved monolithically for velocity in both the fluid and the structure domain. This two-phase system interacts with a freely moving part of the domain boundary, here realized by (but not limited to) the setting of a spherical hole within the domain. This free boundary part may be moved with the flow or with a self-defined velocity. An ALE method is used for the grid movement. To account for the viscoelasticity of the structure, additional Oldroyd-B-like equations can be solved to describe the evolution of elastic strain. Specific selections of these equations allow a combination of different viscoelastic models, such as Kelvin-Voigt, Maxwell, or a parallel connection of these two. Since a neo-Hookean hyperelastic model is used, results are expected to be accurate even at large strains up to 100%. The system is shown to be thermodynamically consistent and stably discretizable, and validity is demonstrated using a challenging benchmark scenario. Practical applicability is demonstrated by an elaborate study aimed at probing viscoelastic properties of biological and synthetic materials. For this purpose, simulations of atomic force microscopy (AFM) experiments are performed. The forces acting on the spherical indenter in experiments can be easily computed for comparison in the simulations. Promising results of this study confirm the usefulness of the method for further research on viscoelastic properties of a wide range of materials. Moreover, the method is easily modifiable in several respects:

- Instead of FSI, the interaction between three structures can also be simulated.

- The shape and motion of the rigid structure can be defined in different ways.
- A variety of viscoelastic models can be implemented.
- Contact dynamics can be simulated, including adhesion of the structure to a wall.

This opens a wide range of future applications of the method in biology, physics or material sciences.

In the second approach, a two-phase fluid interacting with a viscoelastic solid structure is considered. The modeling is motivated by soft wetting scenarios, whose typical example is a liquid drop in air sitting on a soft viscoelastic substrate. Fluid and solid are represented by two separate domains, but aligned at the interface between them. The two-phase fluid is represented by the basic phase field model. The solid structure is modeled as Kelvin-Voigt material with linear elastic contribution. This method takes advantage of the fact that solid materials considered in soft wetting are usually incompressible. Thus, a single Navier-Stokes system which incorporates conservation of momentum and mass can be solved monolithically in both subdomains. Fluid and solid stresses are restricted to their respective domains by characteristic functions. The monolithic system further encompasses the balance of forces across the fluid-solid interface. The latter is sharply represented by grid points and is moved with flow velocity. An ALE method is implemented for the overall grid motion. The coupling conditions at the fluid-solid interface, in addition to force balance, are continuity of velocity, no penetration, and a contact angle condition. The latter is of interest for cases where the fluid-fluid interface meets the fluid-solid interface, resulting in a three-phase contact line (speaking in 3D). Contact line singularities are regularized by the phase field representation of the fluid-fluid interface. The latter can thus move freely in the fluid, controlled only by the evolution of the phase field, and can also undergo topological changes. In particular, droplet merging or contact lines that slip over the substrate are easy to simulate. Hence the method is capable of simulating a variety of both static and dynamic soft wetting phenomena, with the unified approach leading to increased stability compared to previous methods. Specific applications in this thesis include, as a benchmark scenario, the steady state of a droplet on an elastic substrate, followed by simulations with fluid substrates, the (inverted) Cheerios effect including droplet merging, surfing of the contact line over a substrate, and the stick-slip phenomenon. The latter is the subject of a more in-depth study, where simulations provide physical insight into soft wetting dynamics that have been quite unexplored.

In summary, the methods presented here provide powerful tools for exploring poorly understood complex relationships in nature. On the one hand, these methods are already capable of contributing to research in biology, physics, and materials science, and on the other hand, they can be flexibly extended to further broaden the scope of application in the future.

Bibliography

- [1] S. Karpitschka et al. “Droplets move over viscoelastic substrates by surfing a ridge”. In: *Nature Communications* 6.1 (Aug. 2015), p. 7891. ISSN: 2041-1723. DOI: 10.1038/ncomms8891. URL: <https://doi.org/10.1038/ncomms8891>.
- [2] Nele Moelans, Bart Blanpain, and Patrick Wollants. “An introduction to phase-field modeling of microstructure evolution”. In: *Calphad* 32.2 (2008), pp. 268–294. ISSN: 0364-5916. DOI: <https://doi.org/10.1016/j.calphad.2007.11.003>. URL: <https://www.sciencedirect.com/science/article/pii/S0364591607000880>.
- [3] Yulan Li et al. “A review: Applications of the phase field method in predicting microstructure and property evolution of irradiated nuclear materials”. In: *npj Computational Materials* 3 (Dec. 2017). DOI: 10.1038/s41524-017-0018-y.
- [4] Thomas J.R. Hughes, Wing Kam Liu, and Thomas K. Zimmermann. “Lagrangian-Eulerian finite element formulation for incompressible viscous flows”. In: *Computer Methods in Applied Mechanics and Engineering* 29.3 (1981), pp. 329–349. ISSN: 0045-7825. DOI: [https://doi.org/10.1016/0045-7825\(81\)90049-9](https://doi.org/10.1016/0045-7825(81)90049-9). URL: <https://www.sciencedirect.com/science/article/pii/0045782581900499>.
- [5] Helmut Abels, Harald Garcke, and Günther Grün. “Thermodynamically consistent, frame indifferent diffuse interface models for incompressible two-phase flows with different densities”. In: *Mathematical Models and Methods in Applied Sciences* 22.03 (2012), p. 1150013. DOI: 10.1142/S0218202511500138. eprint: <https://doi.org/10.1142/S0218202511500138>. URL: <https://doi.org/10.1142/S0218202511500138>.
- [6] Hang Ding, Peter D.M. Spelt, and Chang Shu. “Diffuse interface model for incompressible two-phase flows with large density ratios”. In: *Journal of Computational Physics* 226.2 (2007), pp. 2078–2095. ISSN: 0021-9991. DOI: <https://doi.org/10.1016/j.jcp.2007.06.028>. URL: <https://www.sciencedirect.com/science/article/pii/S0021999107002793>.
- [7] Dominic Mokbel, Helmut Abels, and Sebastian Aland. “A phase-field model for fluid–structure interaction”. In: *Journal of Computational Physics* 372 (2018), pp. 823–840. ISSN: 0021-9991. DOI: <https://doi.org/10.1016/j.jcp.2018.06.063>. URL: <https://www.sciencedirect.com/science/article/pii/S0021999118304418>.

- [8] Beomkeun Kim et al. “A comparison among Neo-Hookean model, Mooney-Rivlin model, and Ogden model for chloroprene rubber”. In: *International Journal of Precision Engineering and Manufacturing* 13 (2012), pp. 759–764.
- [9] Shada Abuhattum, Dominic Mokbel, et al. “An explicit model to extract viscoelastic properties of cells from AFM force-indentation curves”. In: *iScience* 25.4 (2022), p. 104016. ISSN: 2589-0042. DOI: <https://doi.org/10.1016/j.isci.2022.104016>. URL: <https://www.sciencedirect.com/science/article/pii/S2589004222002863>.
- [10] Sebastian Aland and Dominic Mokbel. “A unified numerical model for wetting of soft substrates”. In: *International Journal for Numerical Methods in Engineering* 122.4 (2021), pp. 903–918. DOI: <https://doi.org/10.1002/nme.6567>. eprint: <https://onlinelibrary.wiley.com/doi/pdf/10.1002/nme.6567>. URL: <https://onlinelibrary.wiley.com/doi/abs/10.1002/nme.6567>.
- [11] Dominic Mokbel, Sebastian Aland, and Stefan Karpitschka. “Stick-slip contact line motion on Kelvin-Voigt model substrates”. In: *Europhysics Letters* 139.3 (Aug. 2022), p. 33002. DOI: 10.1209/0295-5075/ac6ca6. URL: <https://dx.doi.org/10.1209/0295-5075/ac6ca6>.
- [12] Sebastian Aland and Paul Auerbach. “A ternary phase-field model for wetting of soft elastic structures”. In: *International Journal for Numerical Methods in Engineering* 122 (Apr. 2021). DOI: 10.1002/nme.6694.
- [13] Marco F. P. ten Eikelder and I. Akkerman. “An energy-dissipative level-set method for the incompressible two-phase Navier-Stokes equations with surface tension using functional entropy variables”. In: *ArXiv abs/2005.08371* (2020).
- [14] Tinh Quoc Bui and Xiaofei Hu. “A review of phase-field models, fundamentals and their applications to composite laminates”. In: *Engineering Fracture Mechanics* 248 (2021), p. 107705. ISSN: 0013-7944. DOI: <https://doi.org/10.1016/j.engfracmech.2021.107705>. URL: <https://www.sciencedirect.com/science/article/pii/S0013794421001582>.
- [15] Dongsun Lee et al. “Physical, mathematical, and numerical derivations of the Cahn–Hilliard equation”. In: *Computational Materials Science* 81 (2014), pp. 216–225. ISSN: 0927-0256. DOI: <https://doi.org/10.1016/j.commatsci.2013.08.027>. URL: <https://www.sciencedirect.com/science/article/pii/S0927025613004801>.
- [16] Sebastian Aland. “Modelling of two-phase flow with surface active particles”. PhD dissertation. Technische Universität Dresden, 2012.
- [17] S Aland, J Lowengrub, and A Voigt. “Two-phase flow in complex geometries: A diffuse domain approach”. In: *Computer modeling in engineering and sciences : CMES* 57.1 (2010), pp. 77–106. ISSN: 1526-1492. URL: <https://europepmc.org/articles/PMC3171464>.
- [18] Christof Eck, Harald Garcke, and Peter Knabner. *Mathematische Modellierung*. Springer, 2008.
- [19] Hyun Geun Lee and Junseok Kim. “Regularized Dirac delta functions for phase field models”. In: *International Journal for Numerical Methods in Engineering* 91.3 (2012), pp. 269–288. DOI: <https://doi.org/10.1002/nme.4262>. eprint: <https://onlinelibrary.wiley.com/doi/>

- pdf/10.1002/nme.4262. URL: <https://onlinelibrary.wiley.com/doi/abs/10.1002/nme.4262>.
- [20] Luciano Modica and Stefano Mortola. “Un esempio di Gamma-convergenza”. In: *Bollettino della Unione Matematica Italiana B* 5 (14 1977), pp. 285–299.
- [21] Franck Boyer. “A theoretical and numerical model for the study of incompressible mixture flows”. In: *Computers & Fluids* 31.1 (2002), pp. 41–68. ISSN: 0045-7930. DOI: [https://doi.org/10.1016/S0045-7930\(00\)00031-1](https://doi.org/10.1016/S0045-7930(00)00031-1). URL: <https://www.sciencedirect.com/science/article/pii/S0045793000000311>.
- [22] P. G. de Gennes. “Wetting: statics and dynamics”. In: *Reviews of Modern Physics* 57.3 (July 1985), pp. 827–863. DOI: 10.1103/RevModPhys.57.827.
- [23] Antonin Marchand et al. “Contact Angles on a Soft Solid: From Young’s Law to Neumann’s Law”. In: *Phys. Rev. Lett.* 109 (23 Dec. 2012), p. 236101. DOI: 10.1103/PhysRevLett.109.236101. URL: <https://link.aps.org/doi/10.1103/PhysRevLett.109.236101>.
- [24] Minehide Yamamoto et al. “Theoretical Explanation of the Lotus Effect: Superhydrophobic Property Changes by Removal of Nanostructures from the Surface of a Lotus Leaf”. In: *Langmuir* 31.26 (2015). PMID: 26075949, pp. 7355–7363. DOI: 10.1021/acs.langmuir.5b00670. eprint: <https://doi.org/10.1021/acs.langmuir.5b00670>. URL: <https://doi.org/10.1021/acs.langmuir.5b00670>.
- [25] Bruno Andreotti and Jacco H. Snoeijer. “Statics and Dynamics of Soft Wetting”. In: *Annual Review of Fluid Mechanics* 52.1 (2020), pp. 285–308. DOI: 10.1146/annurev-fluid-010719-060147. eprint: <https://doi.org/10.1146/annurev-fluid-010719-060147>. URL: <https://doi.org/10.1146/annurev-fluid-010719-060147>.
- [26] Klaus Deckelnick, Gerhard Dziuk, and Charles M. Elliott. “Computation of geometric partial differential equations and mean curvature flow”. In: *Acta Numerica* 14 (Jan. 2005), pp. 139–232. DOI: 10.1017/S0962492904000224.
- [27] Xianmin Xu and Xiaoping Wang. “Analysis of wetting and contact angle hysteresis on chemically patterned surfaces”. In: *SIAM Journal on Applied Mathematics* 71.5 (2011), pp. 1753–1779. ISSN: 00361399. URL: <http://www.jstor.org/stable/23073406> (visited on 09/13/2022).
- [28] E. Harald van Brummelen et al. “Binary-fluid–solid interaction based on the Navier–Stokes–Cahn–Hilliard Equations”. In: *Fluid-Structure Interaction*. Ed. by Stefan Frei et al. Berlin, Boston: De Gruyter, 2018, pp. 283–328. ISBN: 9783110494259. DOI: 10.1515/9783110494259-008. URL: <https://doi.org/10.1515/9783110494259-008>.
- [29] David Jacqmin. “Calculation of two-phase Navier-Stokes flows using phase-field modeling”. In: *J. Comput. Phys* 155 (1999), pp. 96–127.
- [30] Minh Do-Quang and Gustav Amberg. “The splash of a solid sphere impacting on a liquid surface: Numerical simulation of the influence of wetting”. In: *Physics of Fluids* 21 (2 2009), pp. 0-13. DOI: 10.1063/1.3073968.

- [31] E. Harald van Brummelen, Tristan H.B. Demont, and Gertjan J. van Zwieten. “An adaptive isogeometric analysis approach to elasto-capillary fluid-solid interaction”. In: *International Journal for Numerical Methods in Engineering* 122 (19 2021), pp. 5331–5352. DOI: 10.1002/nme.6388.
- [32] Jesus Bueno et al. “Three-dimensional dynamic simulation of elastocapillarity”. In: *Meccanica* 53 (6 2018), pp. 1221–1237.
- [33] Anupam Pandey et al. “Singular Nature of the Elastocapillary Ridge”. In: *Physical Review X* 10 (3 2020), p. 31067. DOI: 10.1103/PhysRevX.10.031067.
- [34] J.A. Sethian. *Level Set Methods and Fast Marching Methods Evolving Interfaces in Computational Geometry, Fluid Mechanics, Computer Vision, and Materials Science*. Cambridge University Press, 1999.
- [35] Kazuyasu Sugiyama et al. “A full Eulerian finite difference approach for solving fluid-structure coupling problems”. In: *Journal of Computational Physics* 230.3 (2011), pp. 596–627.
- [36] Rajat Mittal and Gianluca Iaccarino. “Immersed Boundary Methods”. In: *Annual Review of Fluid Mechanics* 37.1 (2005), pp. 239–261. DOI: 10.1146/annurev.fluid.37.061903.175743. eprint: <https://doi.org/10.1146/annurev.fluid.37.061903.175743>. URL: <https://doi.org/10.1146/annurev.fluid.37.061903.175743>.
- [37] Gene Hou, Jin Wang, and Anita Layton. “Numerical Methods for Fluid-Structure Interaction - A Review”. In: *Communications in Computational Physics* 12.2 (2012), pp. 337–377. DOI: 10.4208/cicp.291210.290411s.
- [38] Stefan Frei, Thomas Richter, and Thomas Wick. “Eulerian Techniques for Fluid-Structure Interactions: Part I – Modeling and Simulation”. In: *Numerical Mathematics and Advanced Applications-ENUMATH 2013*. Springer, 2015, pp. 745–753.
- [39] C.W Hirt and B.D Nichols. “Volume of fluid method for the dynamics of free boundaries”. In: *Journal of Computational Physics* 39.1 (1981), pp. 201–225. ISSN: 0021-9991. DOI: [https://doi.org/10.1016/0021-9991\(81\)90145-5](https://doi.org/10.1016/0021-9991(81)90145-5). URL: <http://www.sciencedirect.com/science/article/pii/0021999181901455>.
- [40] G. Cottet, E. Maitre, and T. Milcent. “Eulerian formulation and level set models for incompressible fluid-structure interaction”. In: *ESAIM: M2AN* 42.3 (2008), pp. 471–492. DOI: 10.1051/m2an:2008013. URL: <https://doi.org/10.1051/m2an:2008013>.
- [41] A. Legay, J. Chessa, and T. Belytschko. “An Eulerian-Lagrangian method for fluid-structure interaction based on level sets”. In: *Computer Methods in Applied Mechanics and Engineering* 195.17 (2006), pp. 2070–2087. ISSN: 0045-7825. DOI: <https://doi.org/10.1016/j.cma.2005.02.025>. URL: <http://www.sciencedirect.com/science/article/pii/S0045782505001982>.
- [42] Ping He and Rui Qiao. “A full-Eulerian solid level set method for simulation of fluid-structure interactions”. In: *Microfluidics and Nanofluidics* 11.5 (2011), p. 557. ISSN: 1613-4990. DOI: 10.1007/s10404-011-0821-6. URL: <https://doi.org/10.1007/s10404-011-0821-6>.

- [43] Sebastian Aland and Feng Chen. “An efficient and energy stable scheme for a phase-field model for the moving contact line problem”. In: *International Journal for Numerical Methods in Fluids* 81.11 (2016), pp. 657–671. DOI: <https://doi.org/10.1002/flid.4200>. eprint: <https://onlinelibrary.wiley.com/doi/pdf/10.1002/flid.4200>. URL: <https://onlinelibrary.wiley.com/doi/abs/10.1002/flid.4200>.
- [44] G. Grün and F. Klingbeil. “Two-phase flow with mass density contrast: Stable schemes for a thermodynamic consistent and frame-indifferent diffuse-interface model”. In: *Journal of Computational Physics* 257 (2014), pp. 708–725. ISSN: 0021-9991. DOI: <https://doi.org/10.1016/j.jcp.2013.10.028>. URL: <http://www.sciencedirect.com/science/article/pii/S0021999113007043>.
- [45] J. Lowengrub, J. Allard, and S. Aland. “Numerical simulation of endocytosis: Viscous flow driven by membranes with non-uniformly distributed curvature-inducing molecules”. In: *Journal of Computational Physics* 309 (2016), pp. 112–128.
- [46] S. Aland, J. Lowengrub, and A. Voigt. “A continuum model of colloid-stabilized interfaces”. In: *Physics of Fluids* 23.6 (2011), p. 062103.
- [47] Harald Garcke, KF Lam, and B Stinner. “Diffuse interface modelling of soluble surfactants in two-phase flow”. In: *Communications in Mathematical Sciences* 12.8 (2014), pp. 1475–1522. URL: <http://www.intlpress.com/site/pub/pages/journals/items/cms/content/vols/0012/0008/a006/>.
- [48] Sebastian Aland. “Time integration for diffuse interface models for two-phase flow”. In: *Journal of Computational Physics* 262 (2014), pp. 58–71. ISSN: 0021-9991. DOI: <https://doi.org/10.1016/j.jcp.2013.12.055>. URL: <http://www.sciencedirect.com/science/article/pii/S0021999114000102>.
- [49] Pengtao Sun, Jinchao Xu, and Lixiang Zhang. “Full Eulerian finite element method of a phase field model for fluid-structure interaction problem”. In: *Computers & Fluids* 90 (2014), pp. 1–8. ISSN: 00457930. DOI: 10.1016/j.compfluid.2013.11.010. URL: <http://linkinghub.elsevier.com/retrieve/pii/S0045793013004489>.
- [50] Yadong Liu and Dennis Trautwein. *On a diffuse interface model for incompressible viscoelastic two-phase flows*. 2022. DOI: 10.48550/ARXIV.2212.13507. URL: <https://arxiv.org/abs/2212.13507>.
- [51] Javier Bonet and Richard D Wood. *Nonlinear continuum mechanics for finite element analysis*. Cambridge university press, 1997.
- [52] X Li et al. “Solving PDEs in complex geometries: a diffuse domain approach”. In: *Communications in mathematical sciences* 7.1 (2009), p. 81.
- [53] Sébastien Boyaval, Tony Lelièvre, and Claude Mangoubi. “Free-energy-dissipative schemes for the Oldroyd-B model”. In: *ESAIM: M2AN* 43.3 (2009), pp. 523–561. DOI: 10.1051/m2an/2009008. URL: <https://doi.org/10.1051/m2an/2009008>.

- [54] Martien A. Hulsen. “A sufficient condition for a positive definite configuration tensor in differential models”. In: *Journal of Non-Newtonian Fluid Mechanics* 38.1 (1990), pp. 93–100. ISSN: 0377-0257. DOI: [https://doi.org/10.1016/0377-0257\(90\)85034-V](https://doi.org/10.1016/0377-0257(90)85034-V). URL: <https://www.sciencedirect.com/science/article/pii/037702579085034V>.
- [55] Stefan Turek and Jaroslav Hron. “Proposal for Numerical Benchmarking of Fluid-Structure Interaction between an Elastic Object and Laminar Incompressible Flow”. In: *Fluid-Structure Interaction*. Ed. by Hans-Joachim Bungartz and Michael Schäfer. Berlin, Heidelberg: Springer Berlin Heidelberg, 2006, pp. 371–385. ISBN: 978-3-540-34596-1.
- [56] S. Turek et al. “Numerical Benchmarking of Fluid-Structure Interaction: A Comparison of Different Discretization and Solution Approaches”. In: *Fluid Structure Interaction II*. Ed. by Hans-Joachim Bungartz, Miriam Mehl, and Michael Schäfer. Berlin, Heidelberg: Springer Berlin Heidelberg, 2010, pp. 413–424. ISBN: 978-3-642-14206-2.
- [57] Sebastian Aland et al. “Diffuse interface models of locally inextensible vesicles in a viscous fluid”. In: *Journal of Computational Physics* 277 (2014), pp. 32–47. ISSN: 0021-9991. DOI: <https://doi.org/10.1016/j.jcp.2014.08.016>. URL: <https://www.sciencedirect.com/science/article/pii/S0021999114005622>.
- [58] M. Mokbel et al. “Numerical Simulation of Real-Time Deformability Cytometry To Extract Cell Mechanical Properties”. In: *ACS Biomaterials Science & Engineering* 3.11 (2017). PMID: 33418716, pp. 2962–2973. DOI: 10.1021/acsbiomaterials.6b00558. eprint: <https://doi.org/10.1021/acsbiomaterials.6b00558>. URL: <https://doi.org/10.1021/acsbiomaterials.6b00558>.
- [59] Simon Vey and Axel Voigt. “AMDiS: Adaptive multidimensional simulations”. In: *Computing and Visualization in Science* 10.1 (2007), pp. 57–67. ISSN: 1433-0369. DOI: 10.1007/s00791-006-0048-3. URL: <https://doi.org/10.1007/s00791-006-0048-3>.
- [60] T. Witkowski et al. “Software concepts and numerical algorithms for a scalable adaptive parallel finite element method”. In: *Advances in Computational Mathematics* 41.6 (2015), pp. 1145–1177. ISSN: 1572-9044. DOI: 10.1007/s10444-015-9405-4. URL: <https://doi.org/10.1007/s10444-015-9405-4>.
- [61] O. Otto et al. “Real-Time Deformability Cytometry: On-the-fly Cell Mechanical Phenotyping.” In: *Nature Methods* 12.3 (2015), p. 199. DOI: <https://doi.org/10.1038/nmeth.3281>.
- [62] Tatyana G. Kuznetsova et al. “Atomic force microscopy probing of cell elasticity”. In: *Micron* 38.8 (2007). Microscopy in Nanobiotechnology, pp. 824–833. ISSN: 0968-4328. DOI: <https://doi.org/10.1016/j.micron.2007.06.011>. URL: <https://www.sciencedirect.com/science/article/pii/S0968432807001047>.
- [63] Franziska Lautenschläger et al. “The regulatory role of cell mechanics for migration of differentiating myeloid cells”. In: *Proceedings of the National Academy of Sciences* 106.37 (2009), pp. 15696–15701. DOI: 10.1073/pnas.0811261106. eprint: <https://www.pnas.org/doi/>

- pdf/10.1073/pnas.0811261106. URL: <https://www.pnas.org/doi/abs/10.1073/pnas.0811261106>.
- [64] Alba Diz-Muñoz, Daniel A. Fletcher, and Orion D. Weiner. “Use the force: membrane tension as an organizer of cell shape and motility”. In: *Trends in Cell Biology* 23.2 (2013), pp. 47–53. ISSN: 0962-8924. DOI: <https://doi.org/10.1016/j.tcb.2012.09.006>. URL: <https://www.sciencedirect.com/science/article/pii/S0962892412001778>.
- [65] Eric M. Darling et al. “Viscoelastic properties of human mesenchymally-derived stem cells and primary osteoblasts, chondrocytes, and adipocytes”. In: *Journal of Biomechanics* 41.2 (2008), pp. 454–464. ISSN: 0021-9290. DOI: <https://doi.org/10.1016/j.jbiomech.2007.06.019>. URL: <https://www.sciencedirect.com/science/article/pii/S0021929007003028>.
- [66] Robert M Hochmuth. “Micropipette aspiration of living cells”. In: *Journal of Biomechanics* 33.1 (2000), pp. 15–22. ISSN: 0021-9290. DOI: [https://doi.org/10.1016/S0021-9290\(99\)00175-X](https://doi.org/10.1016/S0021-9290(99)00175-X). URL: <https://www.sciencedirect.com/science/article/pii/S002192909900175X>.
- [67] J. Guck et al. “Optical Deformability of Soft Biological Dielectrics”. In: *Phys. Rev. Lett.* 84 (23 June 2000), pp. 5451–5454. DOI: [10.1103/PhysRevLett.84.5451](https://doi.org/10.1103/PhysRevLett.84.5451). URL: <https://link.aps.org/doi/10.1103/PhysRevLett.84.5451>.
- [68] Heinrich Hertz. “Ueber die Berührung fester elastischer Körper”. In: *Band 92*. Ed. by A. L. Crelle, C. W. Borchardt, and Schellbach. Berlin, Boston: De Gruyter, 1882, pp. 156–171. ISBN: 9783112342404. DOI: [doi:10.1515/9783112342404-004](https://doi.org/10.1515/9783112342404-004). URL: <https://doi.org/10.1515/9783112342404-004>.
- [69] Ben Fabry et al. “Scaling the Microrheology of Living Cells”. In: *Phys. Rev. Lett.* 87 (14 Sept. 2001), p. 148102. DOI: [10.1103/PhysRevLett.87.148102](https://doi.org/10.1103/PhysRevLett.87.148102). URL: <https://link.aps.org/doi/10.1103/PhysRevLett.87.148102>.
- [70] Jan Rother et al. “Atomic force microscopy-based microrheology reveals significant differences in the viscoelastic response between malignant and benign cell lines”. In: *Open Biology* 4.5 (2014), p. 140046. DOI: [10.1098/rsob.140046](https://doi.org/10.1098/rsob.140046). eprint: <https://royalsocietypublishing.org/doi/pdf/10.1098/rsob.140046>. URL: <https://royalsocietypublishing.org/doi/abs/10.1098/rsob.140046>.
- [71] Jordi Alcaraz et al. “Microrheology of Human Lung Epithelial Cells Measured by Atomic Force Microscopy”. In: *Biophysical Journal* 84.3 (2003), pp. 2071–2079. ISSN: 0006-3495. DOI: [https://doi.org/10.1016/S0006-3495\(03\)75014-0](https://doi.org/10.1016/S0006-3495(03)75014-0). URL: <https://www.sciencedirect.com/science/article/pii/S0006349503750140>.
- [72] Eric M. Darling et al. “A Thin-Layer Model for Viscoelastic, Stress-Relaxation Testing of Cells Using Atomic Force Microscopy: Do Cell Properties Reflect Metastatic Potential?” In: *Biophysical Journal* 92.5 (2007), pp. 1784–1791. ISSN: 0006-3495. DOI: <https://doi.org/10.1529/biophysj.106.083097>. URL: <https://www.sciencedirect.com/science/article/pii/S0006349507709864>.

- [73] Marcel Mokbel et al. “The Poisson Ratio of the Cellular Actin Cortex Is Frequency Dependent”. In: *Biophysical Journal* 118.8 (Apr. 2020), pp. 1968–1976. ISSN: 0006-3495. DOI: 10.1016/j.bpj.2020.03.002. URL: <https://doi.org/10.1016/j.bpj.2020.03.002>.
- [74] R. E. Mahaffy et al. “Scanning Probe-Based Frequency-Dependent Microrheology of Polymer Gels and Biological Cells”. In: *Phys. Rev. Lett.* 85 (4 July 2000), pp. 880–883. DOI: 10.1103/PhysRevLett.85.880. URL: <https://link.aps.org/doi/10.1103/PhysRevLett.85.880>.
- [75] Shada Abuhattum et al. “Intracellular Mass Density Increase Is Accompanying but Not Sufficient for Stiffening and Growth Arrest of Yeast Cells”. In: *Frontiers in Physics* 6 (2018). ISSN: 2296-424X. DOI: 10.3389/fphy.2018.00131. URL: <https://www.frontiersin.org/articles/10.3389/fphy.2018.00131>.
- [76] Joan-Carles Escolano et al. “Compliant Substrates Enhance Macrophage Cytokine Release and NLRP3 Inflammasome Formation During Their Pro-Inflammatory Response”. In: *Frontiers in Cell and Developmental Biology* 9 (2021). ISSN: 2296-634X. DOI: 10.3389/fcell.2021.639815. URL: <https://www.frontiersin.org/articles/10.3389/fcell.2021.639815>.
- [77] Stephanie Möllmert et al. “Zebrafish Spinal Cord Repair Is Accompanied by Transient Tissue Stiffening”. In: *Biophysical Journal* 118.2 (2020), pp. 448–463. ISSN: 0006-3495. DOI: <https://doi.org/10.1016/j.bpj.2019.10.044>. URL: <https://www.sciencedirect.com/science/article/pii/S0006349519343528>.
- [78] S. V. Kontomaris, A. Stylianou, and A. Malamou. “Is It Possible to Directly Determine the Radius of a Spherical Indenter Using Force Indentation Data on Soft Samples?” In: *Scanning* 2022 (Feb. 2022), p. 6463063. ISSN: 0161-0457. DOI: 10.1155/2022/6463063. URL: <https://doi.org/10.1155/2022/6463063>.
- [79] Yue Ding, Guang-Kui Xu, and Gang-Feng Wang. “On the determination of elastic moduli of cells by AFM based indentation”. In: *Scientific Reports* 7.1 (Apr. 2017), p. 45575. ISSN: 2045-2322. DOI: 10.1038/srep45575. URL: <https://doi.org/10.1038/srep45575>.
- [80] Enrique A. López-Guerra and Santiago D. Solares. “Modeling viscoelasticity through spring-dashpot models in intermittent-contact atomic force microscopy”. In: *Beilstein Journal of Nanotechnology* 5 (2014), pp. 2149–2163. ISSN: 2190-4286. DOI: 10.3762/bjnano.5.224.
- [81] Z. Ilke Kalcioglu et al. “From macro- to microscale poroelastic characterization of polymeric hydrogels via indentation”. In: *Soft Matter* 8 (12 2012), pp. 3393–3398. DOI: 10.1039/C2SM06825G. URL: <http://dx.doi.org/10.1039/C2SM06825G>.
- [82] Susana Moreno-Flores et al. “Stress relaxation and creep on living cells with the atomic force microscope: a means to calculate elastic moduli and viscosities of cell components”. In: *Nanotechnology* 21.44 (Oct. 2010), p. 445101. DOI: 10.1088/0957-4484/21/44/445101. URL: <https://dx.doi.org/10.1088/0957-4484/21/44/445101>.
- [83] L M Rebelo et al. “Comparison of the viscoelastic properties of cells from different kidney cancer phenotypes measured with atomic force microscopy”. In: *Nanotechnology* 24.5 (Jan.

- 2013), p. 055102. DOI: 10.1088/0957-4484/24/5/055102. URL: <https://dx.doi.org/10.1088/0957-4484/24/5/055102>.
- [84] Schanila Nawaz et al. “Cell Visco-Elasticity Measured with AFM and Optical Trapping at Sub-Micrometer Deformations”. In: (2012). DOI: 10.1371/journal.pone.0045297.
- [85] Anshu B. Mathur et al. “Endothelial, cardiac muscle and skeletal muscle exhibit different viscoelastic and elastic properties as determined by atomic force microscopy”. In: *Journal of Biomechanics* 34.12 (2001), pp. 1545–1553. ISSN: 0021-9290. DOI: [https://doi.org/10.1016/S0021-9290\(01\)00149-X](https://doi.org/10.1016/S0021-9290(01)00149-X). URL: <https://www.sciencedirect.com/science/article/pii/S002192900100149X>.
- [86] Bastian Rouven Brückner, Helen Nöding, and Andreas Janshoff. “Viscoelastic Properties of Confluent MDCK II Cells Obtained from Force Cycle Experiments”. In: *Biophysical Journal* 112.4 (2017), pp. 724–735. ISSN: 0006-3495. DOI: <https://doi.org/10.1016/j.bpj.2016.12.032>. URL: <https://www.sciencedirect.com/science/article/pii/S0006349516343387>.
- [87] J. S. de Sousa et al. “Analytical model of atomic-force-microscopy force curves in viscoelastic materials exhibiting power law relaxation”. In: *Journal of Applied Physics* 121.3 (2017), p. 034901. DOI: 10.1063/1.4974043. eprint: <https://doi.org/10.1063/1.4974043>. URL: <https://doi.org/10.1063/1.4974043>.
- [88] Yuri M. Efremov et al. “Measuring nanoscale viscoelastic parameters of cells directly from AFM force-displacement curves”. In: *Scientific Reports* 7.1 (May 2017), p. 1541. ISSN: 2045-2322. DOI: 10.1038/s41598-017-01784-3. URL: <https://doi.org/10.1038/s41598-017-01784-3>.
- [89] Pablo D. Garcia, Carlos R. Guerrero, and Ricardo Garcia. “Nanorheology of living cells measured by AFM-based force–distance curves”. In: *Nanoscale* 12 (16 2020), pp. 9133–9143. DOI: 10.1039/C9NR10316C. URL: <http://dx.doi.org/10.1039/C9NR10316C>.
- [90] E. H. Lee and J. R. M. Radok. “The Contact Problem for Viscoelastic Bodies”. In: *Journal of Applied Mechanics* 27.3 (Sept. 1960), pp. 438–444. ISSN: 0021-8936. DOI: 10.1115/1.3644020. eprint: https://asmedigitalcollection.asme.org/appliedmechanics/article-pdf/27/3/438/5443475/438_1.pdf. URL: <https://doi.org/10.1115/1.3644020>.
- [91] T. C. T. Ting. “The Contact Stresses Between a Rigid Indenter and a Viscoelastic Half-Space”. In: *Journal of Applied Mechanics* 33.4 (Dec. 1966), pp. 845–854. ISSN: 0021-8936. DOI: 10.1115/1.3625192. eprint: https://asmedigitalcollection.asme.org/appliedmechanics/article-pdf/33/4/845/5447986/845_1.pdf. URL: <https://doi.org/10.1115/1.3625192>.
- [92] Elisabeth Fischer-Friedrich et al. “Quantification of surface tension and internal pressure generated by single mitotic cells”. In: *Scientific Reports* 4.1 (Aug. 2014), p. 6213. ISSN: 2045-2322. DOI: 10.1038/srep06213. URL: <https://doi.org/10.1038/srep06213>.
- [93] Elisabeth Fischer-Friedrich et al. “Rheology of the Active Cell Cortex in Mitosis”. In: *Biophysical Journal* 111.3 (2016), pp. 589–600. ISSN: 0006-3495. DOI: <https://doi.org/10.1016/j.bpj.2016.06.008>. URL: <https://www.sciencedirect.com/science/article/pii/S0006349516304416>.

- [94] Anna V. Taubenberger, Buzz Baum, and Helen K. Matthews. “The Mechanics of Mitotic Cell Rounding”. In: *Frontiers in Cell and Developmental Biology* 8 (2020). ISSN: 2296-634X. DOI: 10.3389/fcell.2020.00687. URL: <https://www.frontiersin.org/articles/10.3389/fcell.2020.00687>.
- [95] Nunu Mchedlishvili et al. “Two-step interphase microtubule disassembly aids spindle morphogenesis”. In: *BMC Biology* 16.1 (Jan. 2018), p. 14. ISSN: 1741-7007. DOI: 10.1186/s12915-017-0478-z. URL: <https://doi.org/10.1186/s12915-017-0478-z>.
- [96] Dennis E. Discher, Paul Janmey, and Yu-li Wang. “Tissue Cells Feel and Respond to the Stiffness of Their Substrate”. In: *Science* 310.5751 (2005), pp. 1139–1143. DOI: 10.1126/science.1116995. eprint: <https://www.science.org/doi/pdf/10.1126/science.1116995>. URL: <https://www.science.org/doi/abs/10.1126/science.1116995>.
- [97] Robert W. Style et al. “Patterning droplets with durotaxis”. In: *Proceedings of the National Academy of Sciences* 110.31 (2013), pp. 12541–12544. DOI: 10.1073/pnas.1307122110. eprint: <https://www.pnas.org/doi/pdf/10.1073/pnas.1307122110>. URL: <https://www.pnas.org/doi/abs/10.1073/pnas.1307122110>.
- [98] Mordechai Sokuler et al. “The Softer the Better: Fast Condensation on Soft Surfaces”. In: *Langmuir* 26.3 (2010). PMID: 19928793, pp. 1544–1547. DOI: 10.1021/la903996j. eprint: <https://doi.org/10.1021/la903996j>. URL: <https://doi.org/10.1021/la903996j>.
- [99] M. Lisa Manning et al. “Coaction of intercellular adhesion and cortical tension specifies tissue surface tension”. In: *Proceedings of the National Academy of Sciences* 107.28 (2010), pp. 12517–12522. DOI: 10.1073/pnas.1003743107. eprint: <https://www.pnas.org/doi/pdf/10.1073/pnas.1003743107>. URL: <https://www.pnas.org/doi/abs/10.1073/pnas.1003743107>.
- [100] Chun-Min Lo et al. “Cell Movement Is Guided by the Rigidity of the Substrate”. In: *Biophysical Journal* 79.1 (2000), pp. 144–152. ISSN: 0006-3495. DOI: [https://doi.org/10.1016/S0006-3495\(00\)76279-5](https://doi.org/10.1016/S0006-3495(00)76279-5). URL: <https://www.sciencedirect.com/science/article/pii/S0006349500762795>.
- [101] Stéphane Douezan, Julien Dumond, and Françoise Brochard-Wyart. “Wetting transitions of cellular aggregates induced by substrate rigidity”. In: *Soft Matter* 8 (17 2012), pp. 4578–4583. DOI: 10.1039/C2SM07418D. URL: <http://dx.doi.org/10.1039/C2SM07418D>.
- [102] Daniel Bonn et al. “Wetting and spreading”. In: *Rev. Mod. Phys.* 81 (2 May 2009), pp. 739–805. DOI: 10.1103/RevModPhys.81.739. URL: <https://link.aps.org/doi/10.1103/RevModPhys.81.739>.
- [103] Tiezheng Qian, Xiao-Ping Wang, and Ping Sheng. “A variational approach to moving contact line hydrodynamics”. In: *Journal of Fluid Mechanics* 564 (2006), pp. 333–360. DOI: 10.1017/S0022112006001935.
- [104] M. Souli, A. Ouahsine, and L. Lewin. “ALE formulation for fluid–structure interaction problems”. In: *Computer Methods in Applied Mechanics and Engineering* 190.5 (2000), pp. 659–

675. ISSN: 0045-7825. DOI: [https://doi.org/10.1016/S0045-7825\(99\)00432-6](https://doi.org/10.1016/S0045-7825(99)00432-6). URL: <https://www.sciencedirect.com/science/article/pii/S0045782599004326>.
- [105] E. H. van Brummelen, M. Shokrpour-Roudbari, and G. J. van Zwieten. “Elasto-Capillarity Simulations Based on the Navier–Stokes–Cahn–Hilliard Equations”. In: *Advances in Computational Fluid-Structure Interaction and Flow Simulation: New Methods and Challenging Computations*. Ed. by Yuri Bazilevs and Kenji Takizawa. Cham: Springer International Publishing, 2016, pp. 451–462. ISBN: 978-3-319-40827-9. DOI: 10.1007/978-3-319-40827-9_35. URL: https://doi.org/10.1007/978-3-319-40827-9_35.
- [106] Jesus Bueno et al. “Wettability control of droplet durotaxis”. In: *Soft Matter* 14 (8 2018), pp. 1417–1426. DOI: 10.1039/C7SM01917C. URL: <http://dx.doi.org/10.1039/C7SM01917C>.
- [107] Junseok Kim. “Phase-Field Models for Multi-Component Fluid Flows”. In: *Communications in Computational Physics* 12.3 (2012), pp. 613–661. DOI: 10.4208/cicp.301110.040811a.
- [108] Weiqing Ren and Weinan E. “Boundary conditions for the moving contact line problem”. In: *Physics of Fluids* 19.2 (2007), p. 022101. DOI: 10.1063/1.2646754. eprint: <https://doi.org/10.1063/1.2646754>. URL: <https://doi.org/10.1063/1.2646754>.
- [109] Sebastian Aland and Axel Voigt. “Benchmark computations of diffuse interface models for two-dimensional bubble dynamics”. In: *International Journal for Numerical Methods in Fluids* 69 (May 2012), pp. 747–761. DOI: 10.1002/flid.2611.
- [110] S. Bordère and J.-P. Caltagirone. “A unifying model for fluid flow and elastic solid deformation: A novel approach for fluid–structure interaction”. In: *Journal of Fluids and Structures* 51 (2014), pp. 344–353. ISSN: 0889-9746. DOI: <https://doi.org/10.1016/j.jfluidstructs.2014.09.010>. URL: <https://www.sciencedirect.com/science/article/pii/S0889974614002138>.
- [111] Marcel Mokbel and Sebastian Aland. “An ALE method for simulations of axisymmetric elastic surfaces in flow”. In: *International Journal for Numerical Methods in Fluids* 92 (Mar. 2020). DOI: 10.1002/flid.4841.
- [112] Sven Groß and Arnold Reusken. “An extended pressure finite element space for two-phase incompressible flows with surface tension”. In: *Journal of Computational Physics* 224.1 (2007). Special Issue Dedicated to Professor Piet Wesseling on the occasion of his retirement from Delft University of Technology, pp. 40–58. ISSN: 0021-9991. DOI: <https://doi.org/10.1016/j.jcp.2006.12.021>. URL: <https://www.sciencedirect.com/science/article/pii/S0021999106006097>.
- [113] Robert W. Style et al. “Universal Deformation of Soft Substrates Near a Contact Line and the Direct Measurement of Solid Surface Stresses”. In: *Phys. Rev. Lett.* 110 (6 Feb. 2013), p. 066103. DOI: 10.1103/PhysRevLett.110.066103. URL: <https://link.aps.org/doi/10.1103/PhysRevLett.110.066103>.

- [114] Dominic Aland Sebastian; Mokbel. *Data Supplement for "A unified numerical model for wetting of soft substrates"*. Zenodo, Oct. 2020. DOI: 10.5281/zenodo.4066988. URL: <https://doi.org/10.5281/zenodo.4066988>.
- [115] F. Boyer et al. "Cahn–Hilliard/Navier–Stokes Model for the Simulation of Three-Phase Flows". In: *Transport in Porous Media* 82.3 (Apr. 2010), pp. 463–483. ISSN: 1573-1634. DOI: 10.1007/s11242-009-9408-z. URL: <https://doi.org/10.1007/s11242-009-9408-z>.
- [116] Stefan Karpitschka et al. "Liquid drops attract or repel by the inverted Cheerios effect". In: *Proceedings of the National Academy of Sciences* 113.27 (2016), pp. 7403–7407. DOI: 10.1073/pnas.1601411113. eprint: <https://www.pnas.org/doi/pdf/10.1073/pnas.1601411113>. URL: <https://www.pnas.org/doi/abs/10.1073/pnas.1601411113>.
- [117] Gang Pu and Steven J. Severtson. "Characterization of Dynamic Stick-and-Break Wetting Behavior for Various Liquids on the Surface of a Highly Viscoelastic Polymer". In: *Langmuir* 24.9 (May 2008), pp. 4685–4692. ISSN: 0743-7463. DOI: 10.1021/la703790f. URL: <https://doi.org/10.1021/la703790f>.
- [118] Hadrien Bense, Benoit Roman, and José Bico. "Surface Effects on Elastic Structures". In: *Mechanics and Physics of Solids at Micro- and Nano-Scales*. John Wiley & Sons, Ltd, 2019. Chap. 7, pp. 185–213. ISBN: 9781119687566. DOI: <https://doi.org/10.1002/9781119687566.ch7>. eprint: <https://onlinelibrary.wiley.com/doi/pdf/10.1002/9781119687566.ch7>. URL: <https://onlinelibrary.wiley.com/doi/abs/10.1002/9781119687566.ch7>.
- [119] Longquan Chen et al. "Static and dynamic wetting of soft substrates". In: *Current Opinion in Colloid & Interface Science* 36 (2018). Wetting and Spreading, pp. 46–57. ISSN: 1359-0294. DOI: <https://doi.org/10.1016/j.cocis.2017.12.001>. URL: <https://www.sciencedirect.com/science/article/pii/S1359029417301371>.
- [120] Robert W. Style et al. "Elastocapillarity: Surface Tension and the Mechanics of Soft Solids". In: *Annual Review of Condensed Matter Physics* 8.1 (2017), pp. 99–118. DOI: 10.1146/annurev-conmatphys-031016-025326. eprint: <https://doi.org/10.1146/annurev-conmatphys-031016-025326>. URL: <https://doi.org/10.1146/annurev-conmatphys-031016-025326>.
- [121] Binyu Zhao et al. "Elasticity-to-Capillarity Transition in Soft Substrate Deformation". In: *Nano Letters* 21.24 (Dec. 2021), pp. 10361–10367. ISSN: 1530-6984. DOI: 10.1021/acs.nanolett.1c03643. URL: <https://doi.org/10.1021/acs.nanolett.1c03643>.
- [122] Su Ji Park et al. "Visualization of asymmetric wetting ridges on soft solids with X-ray microscopy". In: *Nature Communications* 5.1 (July 2014), p. 4369. ISSN: 2041-1723. DOI: 10.1038/ncomms5369. URL: <https://doi.org/10.1038/ncomms5369>.
- [123] Alain Carré, Jean-Claude Gastel, and Martin E. R. Shanahan. "Viscoelastic effects in the spreading of liquids". In: *Nature* 379.6564 (Feb. 1996), pp. 432–434. ISSN: 1476-4687. DOI: 10.1038/379432a0. URL: <https://doi.org/10.1038/379432a0>.

- [124] Katrina Smith-Mannschott et al. “Droplets Sit and Slide Anisotropically on Soft, Stretched Substrates”. In: *Phys. Rev. Lett.* 126 (15 Apr. 2021), p. 158004. DOI: 10.1103/PhysRevLett.126.158004. URL: <https://link.aps.org/doi/10.1103/PhysRevLett.126.158004>.
- [125] Tadashi Kajiyama et al. “Advancing liquid contact line on visco-elastic gel substrates: stick-slip vs. continuous motions”. In: *Soft Matter* 9 (2 2013), pp. 454–461. DOI: 10.1039/C2SM26714D. URL: <http://dx.doi.org/10.1039/C2SM26714D>.
- [126] S. J. Park et al. “Self-spreading of the wetting ridge during stick-slip on a viscoelastic surface”. In: *Soft Matter* 13 (44 2017), pp. 8331–8336. DOI: 10.1039/C7SM01408B. URL: <http://dx.doi.org/10.1039/C7SM01408B>.
- [127] M. van Gorcum et al. “Dynamic Solid Surface Tension Causes Droplet Pinning and Depinning”. In: *Phys. Rev. Lett.* 121 (20 Nov. 2018), p. 208003. DOI: 10.1103/PhysRevLett.121.208003. URL: <https://link.aps.org/doi/10.1103/PhysRevLett.121.208003>.
- [128] M. van Gorcum et al. “Spreading on viscoelastic solids: are contact angles selected by Neumann’s law?” In: *Soft Matter* 16 (5 2020), pp. 1306–1322. DOI: 10.1039/C9SM01453E. URL: <http://dx.doi.org/10.1039/C9SM01453E>.
- [129] D. C. Dyson. “Contact line stability at edges: Comments on Gibbs’s inequalities”. In: *The Physics of Fluids* 31.2 (1988), pp. 229–232. DOI: 10.1063/1.866851. eprint: <https://aip.scitation.org/doi/pdf/10.1063/1.866851>. URL: <https://aip.scitation.org/doi/abs/10.1063/1.866851>.
- [130] Julien Dervaux, Matthieu Roché, and Laurent Limat. “Nonlinear theory of wetting on deformable substrates”. In: *Soft Matter* 16 (22 2020), pp. 5157–5176. DOI: 10.1039/D0SM00395F. URL: <http://dx.doi.org/10.1039/D0SM00395F>.
- [131] Stefan Karpitschka et al. “Soft wetting: Models based on energy dissipation or on force balance are equivalent”. In: *Proceedings of the National Academy of Sciences* 115.31 (2018), E7233–E7233. DOI: 10.1073/pnas.1808870115. eprint: <https://www.pnas.org/doi/pdf/10.1073/pnas.1808870115>. URL: <https://www.pnas.org/doi/abs/10.1073/pnas.1808870115>.
- [132] Surjyasish Mitra et al. *Unsteady wetting of soft solids*. 2022. DOI: 10.48550/ARXIV.2211.07043. URL: <https://arxiv.org/abs/2211.07043>.
- [133] Jaroslav Štigler. “Analytical velocity profile in tube for laminar and turbulent flow”. In: *Engineering Mechanics* 21.6 (2014), pp. 371–379.
- [134] R. G. Cox. “The dynamics of the spreading of liquids on a solid surface. Part 1. Viscous flow”. In: *Journal of Fluid Mechanics* 168 (1986), pp. 169–194. DOI: 10.1017/S0022112086000332.
- [135] O. V. Voinov. “Hydrodynamics of wetting”. In: *Fluid Dynamics* 11.5 (Sept. 1976), pp. 714–721. ISSN: 1573-8507. DOI: 10.1007/BF01012963. URL: <https://doi.org/10.1007/BF01012963>.
- [136] Jacco H. Snoeijer and Bruno Andreotti. “Moving Contact Lines: Scales, Regimes, and Dynamical Transitions”. In: *Annual Review of Fluid Mechanics* 45.1 (2013), pp. 269–292. DOI: 10.1146/annurev-fluid-011212-140734. eprint: <https://doi.org/10.1146/annurev-fluid-011212-140734>. URL: <https://doi.org/10.1146/annurev-fluid-011212-140734>.

-
- [137] Qin Xu, Robert W Style, and Eric R Dufresne. “Surface elastic constants of a soft solid”. In: *Soft Matter* 14.6 (2018), pp. 916–920.
- [138] Qin Xu et al. “Direct measurement of strain-dependent solid surface stress”. In: *Nature communications* 8.1 (2017), p. 555.
- [139] Zezhou Liu, Anand Jagota, and Chung-Yuen Hui. “Modeling of surface mechanical behaviors of soft elastic solids: theory and examples”. In: *Soft Matter* 16.29 (2020), pp. 6875–6889.
- [140] Stefanie Heyden et al. “Contact lines on stretched soft solids: modelling anisotropic surface stresses”. In: *Proceedings of the Royal Society A* 477.2245 (2021), p. 20200673.
- [141] Weiwei Zhao et al. “The role of crosslinking density in surface stress and surface energy of soft solids”. In: *Soft Matter* 18.3 (2022), pp. 507–513.
- [142] Frank J Holly and Michael A Lemp. “Wettability and wetting of corneal epithelium”. In: *Experimental eye research* 11.2 (1971), pp. 239–250.
- [143] Manu Prakash, David Quéré, and John WM Bush. “Surface tension transport of prey by feeding shorebirds: the capillary ratchet”. In: *science* 320.5878 (2008), pp. 931–934.
- [144] Carlos Pérez-González et al. “Active wetting of epithelial tissues”. In: *Nature physics* 15.1 (2019), pp. 79–88.
- [145] Bruno Andreotti and Jacco H. Snoeijer. “Soft wetting and the Shuttleworth effect, at the crossroads between thermodynamics and mechanics”. In: *Europhysics Letters* 113.6 (Apr. 2016), p. 66001. DOI: 10.1209/0295-5075/113/66001. URL: <https://dx.doi.org/10.1209/0295-5075/113/66001>.

Acknowledgments

I would like to express my deep gratitude to my supervisor Prof. Dr. Sebastian Aland, who gave me excellent support and motivation at all stages of this work from the very beginning. He was always ready to answer my questions and always provided a pleasant atmosphere. Through his provision of funding opportunities and exciting projects, the last years have been a time for me to enjoy my work.

In addition, a number of other people deserve my sincere thanks:

- The entire Aland lab group, in particular Marcel Mokbel, Lucas Wittwer, Eloy de Kinkelder, Luise Zieger, Claudia Wohlgemuth, Maximilian Kloppe, and Paul Auerbach, for an environment where we support each other and always have a great time together.
- Shada Abuhattum for the cooperation regarding the AFM experiments and simulations.
- Stefan Karpitschka for the cooperation regarding the analysis of the stick-slip simulations.
- Helmut Abels for the cooperation regarding the phase field model for fluid-structure interaction.

I am also especially grateful to my wife for supporting me at any time and providing a refreshing and motivating atmosphere. Finally, I would like to thank my parents who have supported me not only materially, but also through the loving and humorous family environment in which I feel comfortable at all times.

Copyright Information

Die am heutigen Tag eingereichte Dissertation zum Thema

Phase field modeling of ternary fluid-structure interaction problems

wurde am Institut für Numerische Mathematik und Optimierung der TU Freiberg unter Betreuung durch Prof. Dr. rer. nat. Sebastian Aland angefertigt. Hiermit versichere ich, dass ich die vorliegende Dissertation ohne unzulässige Hilfe Dritter und ohne Benutzung anderer als der angegebenen Hilfsmittel angefertigt habe. Die aus fremden Quellen direkt oder indirekt übernommenen Gedanken sind als solche kenntlich gemacht. Die Arbeit wurde bisher weder im Inland noch im Ausland in gleicher oder ähnlicher Form einer anderen Prüfungsbehörde vorgelegt.

Freiberg, den 1. Februar 2024

M.Sc. Dominic Mokbel Ala Al Dawla

Versicherung

Hiermit versichere ich, dass ich die vorliegende Arbeit ohne unzulässige Hilfe Dritter und ohne Benutzung anderer als der angegebenen Hilfsmittel angefertigt habe; die aus fremden Quellen direkt oder indirekt übernommenen Gedanken sind als solche kenntlich gemacht. Bei der Auswahl und Auswertung des Materials sowie bei der Herstellung des Manuskripts habe ich Unterstützungsleistungen von folgenden Personen erhalten:

Weitere Personen waren an der Abfassung der vorliegenden Arbeit nicht beteiligt. Die Hilfe eines Promotionsberaters habe ich nicht in Anspruch genommen. Weitere Personen haben von mir keine geldwerten Leistungen für Arbeiten erhalten, die nicht als solche kenntlich gemacht worden sind. Die Arbeit wurde bisher weder im Inland noch im Ausland in gleicher oder ähnlicher Form einer anderen Prüfungsbehörde vorgelegt.

Freiberg, den 1. Februar 2024

M.Sc. Dominic Mokbel Ala Al Dawla